Adaptive Control of Waveguide Modes in Two-Mode Fibers

Peng Lu

Dissertation submitted to the faculty of the Virginia Polytechnic Institute and State University in partial fulfillment of the requirements for the degree of

Doctor of Philosophy
In
Electrical Engineering

Yong Xu, Chair
Anbo Wang
Hans Robinson
Shay Soker
William Baumann

Feb. 18, 2016
Blacksburg, VA

Keywords: Adaptive optics, fiber optics, multimode fiber, mode control, mode division multiplexing, time division multiplexing, fiber Bragg gratings

Adaptive Control of Waveguide Modes in Two-Mode Fibers

Peng Lu

ABSTRACT

Few mode fibers and multimode fibers (MMFs) are traditionally regarded as unsuitable for important applications such as communications and sensing. A major challenge in using MMFs for aforementioned applications is how to precisely control the waveguide modes propagating within MMFs. In this thesis, we experimentally demonstrate a generic method for controlling the linearly polarized (LP) modes within a two-mode fiber (TMF). Our method is based on adaptive optics (AO), where one utilizes proper feedback signals to shape the wavefront of the input beam in order to achieve the desired LP mode composition.

In the first part of this thesis, we demonstrate the feasibility of AO-based mode control by using the correlation between the experimentally measured field distribution and the desired mode profiles as feedback for wavefront optimization. Selectively excitation of pure LP modes or their combinations at the distal end of a TMF are shown. Furthermore, we demonstrate that selective mode excitation in the TMF can be achieved by using only 5×5 independent phase blocks.

Afterwards, we extend our AO-based mode control method to more practical scenarios, where feedback signals are provided by all-fiber devices such as a directional fiber coupler or fiber Bragg gratings (FBGs). Using the coupling ratio of a directional coupler as feedback, we demonstrate adaptive control of LP modes at the two output ports of the directional coupler. With feedback determined by the relative magnitude of optical power reflected by a FBG and the transmitted power, selective excitations of the LP_{01} and the LP_{11} modes are experimentally shown.

As the final component of this thesis, we experimentally combine the AO-based mode control with time-division-multiplexing. By choosing reflected pulses with appropriate arrival time for mode control, we can selectively excite the LP_{11} mode at different FBG locations within the TMF, based on the ratio of optical signals reflected by FBGs in the TMF and the transmitted signal. Using two lasers set at the two FBG peak reflection wavelengths associated with the LP_{01} and the LP_{11} modes, we can accomplish AO-based mode control within a TMF by using only the reflection signals from the FBG. By using the ratio of the reflected signals of two lasers as feedback, we demonstrate selective excitation of almost pure LP_{01} or LP_{11} mode at the FBG location within the TMF.

The method developed in this thesis is generic and can be extended to many other applications using appropriately chosen feedback signals. It is possible to generalize the AO-based mode control method to MMF as well. This method may find important applications in MMF-based communication, sensing and imaging *et. al.* in the future.

Acknowledgement

First and foremost, I would like to thank my advisor Dr. Yong Xu. It is my honor to be his PhD student. I appreciate all his contribution of time, ideas, and funding to make my Ph.D. experience enjoyable and productive. The joy and enthusiasm he has for his research is contagious and motivational for me. I have benefitted so much from his innovative thinking and broad knowledge during my Ph.D. research. I am also thankful for the excellent example he has provided as a successful researcher and professor.

I wish to express my sincere thanks to Dr. Anbo Wang for providing full access to his lab facilities and helpful discussion.

I wish to thank the members of my dissertation committee: Drs. Yong Xu, Anbo Wang, Hans Robinson, William Baumann, and Shay Soker for generously offering their time, support, and guidance throughout the preparation and review of this document.

Further gratitude is for all of my colleagues and friends for their continual help and unforgettable friendships: Xiangyu Wei, Islam Ashry, Baigang Zhang, Matthias Hoffmann, Bryce White, Chalongrat Daengngam, Ishac Kandas, Bo Dong, Xu Yuan, Aram Lee, Zhipeng Tian, Chennan Hu, Lingmei Ma, Bo Liu, Di Hu, Li Yu, Nan Wu, Jing Wang, Chaofan Wang, Shuo Yang, Jiaji He, Michael Fraser, and Etai Sapoznik.

I owe my loving thanks to my wife Mengna Liu. Without her love, understanding, and support, it would have been impossible for me to finish this work. I appreciate so much for her accompaniment in this wonderful journey and in our future life. I hope you always know how much I love you.

Last but not least, my deep gratitude is given to my mother, farther, mother-in-law, and father-in-law, for their unconditional love, support, and endless encouragement from the other side of the globe. With their unceasing love, my journey to the Ph.D. has never been lonely.

Contents

1. Introduction **1**

1.1 Motivation…… 2

1.2 Research Objectives…… 3

1.3 Thesis Organization…… 3

2. Background **6**

2.1 LP Modes in Step-Index Fibers...…… 6

2.2 Directional Fiber Couplers..…… 11

2.3 Fiber Bragg Gratings...…… 12

2.4 Recent Applications of MMF…… 14

2.5 Mode Control Methods in MDM…… 17

2.6 Recent Development of AO……... 20

2.7 Principle of AO based Mode Control in TMF…… 23

3. Adaptive Mode Control Based on Mode Correlation Functions **26**

3.1 Experiment Setup and AO algorithm…… 26

3.2 Experiment Results…… 29

3.3 Discussion and Conclusions…….. 35

4. Adaptive Mode Control Using a Directional Coupler **37**

4.1 Experiment Setup and AO algorithm…… 37

4.2 Experiment Results……... 40

4.3 Discussion and Conclusions…… 48

5. Adaptive Mode Control Based on Fiber Bragg Gratings **50**

5.1 Experiment Setup and AO algorithm…… 50

5.2 Experiment Results…….. 53

5.3 Discussion and Conclusions…… 61

6. Adaptive Mode Control in Time Domain **63**

6.1 Mode Control Based on Transmission and Reflection Signals…… 64

6.1.1 Experiment Setup and AO algorithm…… 64

6.1.2 Experiment Results…… 67
6.2 Mode Control Based on Reflection Signals……. …….. 74
6.2.1 Experiment Setup and AO algorithm……. 74
6.2.2 Experiment Results…… 76
6.3 Discussion and Conclusions…… 82
7. Summary of Future Work **84**
References **86**

List of abbreviations

AO	Adaptive optics
BFS	Brillouin frequency shift
CGH	Computer-generated-holography
DM	Deformable mirror
DSP	Digital signal processor
EDFA	Erbium-doped fiber amplifier
EM	Electromagnetic
FBG	Fiber Bragg grating
FMF	Few-mode fiber
LP	Linearly polarized
LPG	Long period grating
MCR	Mode contrast ratio
MDM	Mode-division-multiplexing
MMF	Multimode fiber
MIMO	Multiple-input-multiple-output
MSC	Mode selective coupler
OPC	Optical-phase-conjugation
SBS	Stimulated Brillouin scattering
SDM	Space-division multiplexing
SLM	Spatial light modulator
SMF	Single mode fiber
SMS	SMF-MMF-SMF
SNR	Signal-to-noise ratio
TDM	Time-division-multiplexing
TM	Transmission matrix
TMF	Two-mode fiber
WDM	Wavelength-division-multiplexing

Chapter 1

Introduction

Fiber optics, on which internet is based, has become one of the most important technological platforms. Traditionally, single mode fibers (SMFs) are highly preferred for a large number of applications, such as optical communications and sensing. The main reason is that there are more than one propagation modes in multimode fibers (MMFs), and individual modes are strongly coupled with each other in MMFs. The intermodal coupling in MMF can depend on a large number of environmental factors, including geometrical deformation (such as fiber bending) and strain. For many applications, it is very difficult to precisely control these environmental parameters. As a result, the coupling between different fiber modes is typically unknown and cannot be precisely controlled. In turn, the inability for precise mode control in MMFs makes them unattractive for a large number of important applications.

Recently, MMF has attracted many interests in fiber optical researches. A well-known example is the mode-division-multiplexing (MDM) in fiber optical communications [1-3]. In MDM, individual waveguide modes in MMFs are utilized as communication channels for signal multiplexing. With the help of sophisticated multiple-input-multiple-output (MIMO) digital signal processing techniques, the information capacity of the optical communication network can be significantly improved [4-6]. In addition, MMFs have been recently used in imaging systems [7, 8] and particle manipulation [9]. MMF-based nonlinear optics such as stimulated Brillouin scattering (SBS) [10, 11], and optical sensing have also been investigated [12].

For all these applications, a major challenge is how to accurately control the form of optical waves in the MMF, *i.e.* selectively excite desired modes in the MMF. In MDM, this task can be accomplished by using multiple techniques, such as long period gratings

(LPGs) in MMF [6], spot-based coupler or spatial beam sampler [13, 14], photonic lanterns [15-17], phase masks [4, 18] or spatial light modulators (SLMs) [5, 19, 20]. In MMF-based imaging, a number of researchers directly measure the transmission matrix (TM) of a MMF and use the measured TM to quantify intermodal coupling and achieve high resolution imaging [7, 9].

1.1 Motivation

Though various techniques have been proposed to control the guided waves in MMF, all methods in existing literature have the same drawback: mode control in MMFs is mainly accomplished at either the input or the output ports of the MMF network, and mode control *within* the MMF network is not investigated. For example in MDM, one mainly focuses on the relationship of optical fields between the input and the output ports, and typically describes the impact of intermodal coupling of the entire MMF network as an impulse response matrix. Thus, existing MDM techniques cannot be used to control the guided modes *within* a MMF network. The TM-based approach requires direct imaging of optical fields on the output plane of the MMF. Therefore, it is difficult to extend these techniques to applications that require model control *within* the MMF network, especially if one cannot directly image optical fields at desired locations.

If we extend the concept of MDM to optical sensing, where sensors are constructed using MMFs and are connected to each other via MMF networks, one often needs to be able to control the form of optical fields at each sensor location. The reason is that, the response of a MMF-based sensor can be highly mode dependent. For example, for a two-mode fiber (TMF) that supports one fundamental linearly polarized (LP) mode (i.e., LP_{01}) and two degenerate LP_{11} modes, a regular fiber Bragg grating (FBG) can produce multiple reflection peaks in the spectral domain [21, 22]. Therefore, relating the response of an FBG sensor with the yet-to-be-measured external parameters can become challenging, if one does not know the composition of optical modes at the sensor location. Thus, there is an urgent need to develop a generic method for mode control *within* the MMF network. The same capability may also be relevant for developing MMF-based imaging systems and nonlinear fiber optics.

In this thesis, we describe a generic adaptive optics (AO) based platform for mode control *within* a few mode fiber (FMF). AO has attracted great attention recently in scattering medium focusing [23-28], turbid medium imaging [29,30], and particle manipulation [7-9]. In addition, AO has been used previously in fiber optics for mode control [19, 20, 31], reduction of intermodal dispersion [32], and MDM related applications [5, 33]. Inspired by MDM and scattering medium focusing, we aim to develop an AO-based method for mode control *within* FMF-based sensing networks. It is equivalent to optical "focusing" in modal domain. Since our main purpose is to demonstrate the feasibility of this AO-based platform for mode control, we mainly use step-index TMFs in this thesis and all experiments are conducted using TMFs.

1.2 Research Objectives

The goal of this research is to develop a novel and generic method for modes control *within* a TMF using the AO approach. More specifically, we aim to accomplish the following three research objectives.

1. Experimentally demonstrate the feasibility of mode control *within* a TMF by using the AO method.
2. Experimentally achieve AO-based mode control *within* a TMF by using all-fiber devices to provide feedback signals, such as directional fiber couplers and FBGs.
3. Experimentally demonstrate the feasibility of AO-based mode control at different locations *within* a TMF.

1.3 Thesis Organization

This dissertation is organized as follows:

Chapter 2: Background

In this Chapter, we briefly introduce the background knowledge and key topics related to the research in this thesis. We first summarize the theoretical analysis of LP modes in weakly guiding step-index SMFs and FMFs. Then we briefly introduce all-fiber devices such as the directional fiber coupler and FBGs used in the following experiments. Afterwards, we review the relevant research on MMFs, current techniques for mode control in MDM, and the recent development of AO, including recent applications of AO

in scattering media imaging system and fiber optics. Finally, we introduce the generic AO algorithm used in this research, and compare it with existing methods in literature.

Chapter 3: Adaptive Mode Control Based on Mode Correlation Functions

In this Chapter, we investigate the feasibility of using the AO algorithm mentioned in Section 2.7 and an appropriate feedback function to control the form of the optical field at a given location in a TMF. As a proof-of-concept experiment, we demonstrate AO-base mode control at the distal end of the TMF, and the feedback function is the correlation between the desired optical field profile and the optical intensity profile captured by a CCD camera. Experiment results of AO-based mode control using different numbers of phase blocks are also studied in this chapter.

Chapter 4: Adaptive Mode Control Using a Directional Coupler

In this Chapter, we extend the work in Chapter 3 to a more practical case, where the feedback function is based on the optical power within the two output ports of a TMF directional coupler. Specifically, we demonstrate that by maximizing or minimizing feedback functions such as the coupling ratio of the directional coupler, we can ensure optical wave at the desired coupler port to be a specific LP mode. Experiment results of feedback base on the absolute power of specific output port are also shown in this chapter.

Chapter 5: Adaptive Mode Control Based on Fiber Bragg Gratings

In this Chapter, we demonstrate adaptive mode control *within* a TMF by using optical signals produced by FBGs. The feedback signal is determined by the ratio of optical power transmitted through and reflected by an FBG written in the TMF. For many applications, the FBG-based mode control approach is superior to the coupler-based approach in Chapter 4.

Chapter 6: Adaptive Mode Control in Time Domain

In this Chapter, we show experiment results of AO-based mode control at different locations *within* a TMF. Specifically, we combine FBG-based mode control developed in Chapter 5 and the time-division-multiplexing (TDM) technique. The method requires multiple inline FBGs in a TMF and uses pulsed optical signals for mode control. The reflected signal from specific FBG can be determined by the arrival time of reflected pulse. By using feedback signal similar to Chapter 5, we can accomplish adaptive mode control at different locations *within* the TMF. Additionally, we demonstrate adaptive

mode control based on only the reflection signals from the FBG. Experimentally, it is achieved by using two lasers set at the two FBG peak reflection wavelengths associated with the LP_{01} and LP_{11} modes, and the feedback is the ratio of reflection signals of two lasers from the FBG location. It should be possible to extend the reflection signals based AO method to mode control at multiple locations within a TMF sensor network in the future.

Chapter 7: Summary of Future Work

In this chapter, we discuss potential improvement of the AO-based mode control method developed in this thesis, and we briefly outline possible future development.

Chapter 2

Background

In this Chapter, we first describe the basic procedure for calculating fiber modes in step-index SMFs and FMFs. Then we discuss the degenerate LP modes in weakly guiding fibers. In Sections 2.2 and 2.3, we briefly introduce two important all-fiber devices used in experiments of later chapters, the directional fiber coupler and FBGs. Afterwards, in Sections 2.4-2.6, we review recent development of MMF-based applications, different techniques for selective mode excitation in MDM, and relevant literature on AO. In section 2.7, we outline the generic principle of the AO-based mode control method, which forms the foundation for experiments described in later chapters.

2.1 LP Modes in Step-Index Fibers

Figure 2.1.1 shows the geometric structure of a step-index fiber and its refractive index profile, which is generally expressed as,

$$n(r) = \begin{cases} n_1 & 0 \le r \le a \\ n_2 & a < r \le b \end{cases} \tag{2.1.1}$$

where n_1 and n_2 are refractive indices of the fiber core and cladding respectively, with $n_1 > n_2$; a is the core radius, and b is the cladding radius. For standard step-index SMFs and FMFs, the core radius is typically smaller than 5 μm, and the cladding radius is ~ 62.5 μm.

To analyze the mode field distribution in step-index SMFs and FMFs, one needs to solve Maxwell's equations subject to appropriate boundary conditions. For simplicity, we can

assume the fiber cladding extends to infinity, because the optical field of propagation modes almost vanishes at the edge of the fiber cladding.

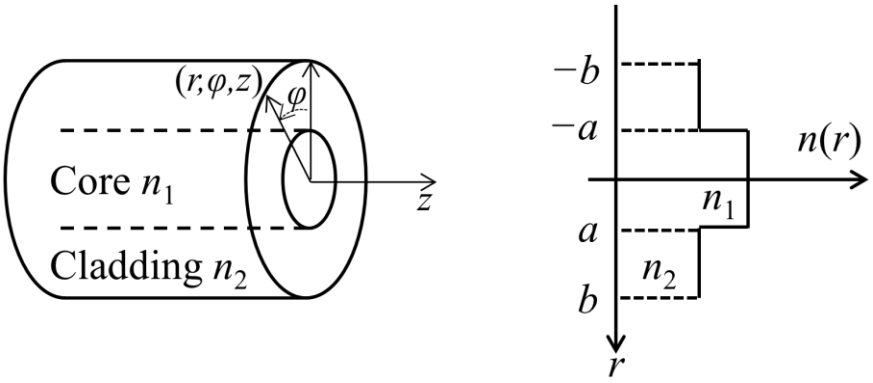

Fig. 2.1.1 Geometric structure of a step-index fiber and its refractive index profile

Based on Maxwell's equations in dielectric material with no currents and free charges, the following wave equations can be derived,

$$\nabla^2\mathbf{E} = \varepsilon\mu\frac{\partial^2\mathbf{E}}{\partial t^2} \tag{2.1.2}$$

$$\nabla^2\mathbf{H} = \varepsilon\mu\frac{\partial^2\mathbf{H}}{\partial t^2} \tag{2.1.3}$$

where ε is the dielectric constant, and μ is the permeability of the medium.

Considering electromagnetic (EM) waves propagating along the step-index fiber under cylindrical coordinates shown in Fig. 2.1.1, we can express the EM field in the following time-harmonic form,

$$\mathbf{E}(r,\varphi,z) = \mathbf{E}_0(r,\varphi)e^{j(\omega t-\beta z)} \tag{2.1.4}$$

$$\mathbf{H}(r,\varphi,z) = \mathbf{H}_0(r,\varphi)e^{j(\omega t-\beta z)} \tag{2.1.5}$$

$$\mathbf{E}_0(r,\varphi) = E_r(\mathrm{r},\varphi)\hat{a}_r + E_\varphi(\mathrm{r},\varphi)\hat{a}_\varphi + E_z(\mathrm{r},\varphi)\hat{a}_z \tag{2.1.6}$$

$$\mathbf{H}_0(r,\varphi) = H_r(\mathrm{r},\varphi)\hat{a}_r + H_\varphi(\mathrm{r},\varphi)\hat{a}_\varphi + H_z(\mathrm{r},\varphi)\hat{a}_z \tag{2.1.7}$$

where β is the mode propagation constant along the z-axis, and it satisfies $n_2k_0 < \beta < n_1k_0$. k_0 is the free space wavenumber. $\hat{a}_r$, $\hat{a}_\varphi$ and $\hat{a}_z$ are unit vectors in cylindrical coordinates shown in Fig. 2.2.1.

Substitute Eq. (2.1.4) into Eq. (2.1.2) we can derive,

$$\nabla^2\mathbf{E} = (\nabla_t^2 + \frac{\partial^2}{\partial z^2})\mathbf{E} = \nabla_t^2\mathbf{E} - \beta^2\mathbf{E} = e^{j(\omega t-\beta z)}(\nabla_t^2\mathbf{E}_0 - \beta^2\mathbf{E}_0) \tag{2.1.8}$$

$$\varepsilon\mu\frac{\partial^2\mathbf{E}}{\partial t^2} = -\omega^2\varepsilon\mu\mathbf{E} = -e^{j(\omega t-\beta z)}\omega^2\varepsilon\mu\mathbf{E}_0 \tag{2.1.9}$$

Thus Eq. (2.1.2) becomes,

$$\nabla_t^2\mathbf{E}_0 + (\omega^2\varepsilon\mu - \beta^2)\mathbf{E}_0 = 0 \tag{2.1.10}$$

Similarly, Eq. (2.1.3) becomes,

$$\nabla_t^2\mathbf{H}_0 + (\omega^2\varepsilon\mu - \beta^2)\mathbf{H}_0 = 0 \tag{2.1.11}$$

Equations (2.1.10) and (2.1.11) can be simplified as,

$$\nabla_t^2\phi + q^2\phi = 0 \quad \text{with } q^2 = \omega^2\varepsilon\mu - \beta^2 \tag{2.1.12}$$

Substitute Eqs. (2.1.6) and (2.1.7) into following Maxwell's equations,

$$\nabla\times\mathbf{E} = -\frac{\partial\mathbf{B}}{\partial t} \tag{2.1.13}$$

$$\nabla\times\mathbf{B} = \frac{\partial\mathbf{D}}{\partial t} \tag{2.1.14}$$

We can derive,

$$E_r = -\frac{j}{q^2}(\beta\frac{\partial E_z}{\partial r} + \frac{\mu\omega}{r}\frac{\partial H_z}{\partial\varphi}) \tag{2.1.15}$$

$$E_\varphi = -\frac{j}{q^2}(\frac{\beta}{r}\frac{\partial E_z}{\partial\varphi} - \mu\omega\frac{\partial H_z}{\partial r}) \tag{2.1.16}$$

$$H_r = -\frac{j}{q^2}(\beta\frac{\partial H_z}{\partial r} - \frac{\varepsilon\omega}{r}\frac{\partial E_z}{\partial\varphi}) \tag{2.1.17}$$

$$H_\varphi = -\frac{j}{q^2}(\frac{\beta}{r}\frac{\partial H_z}{\partial\varphi} + \varepsilon\omega\frac{\partial E_z}{\partial r}) \tag{2.1.18}$$

It is clear that with E_z and H_z determined, other EM field components can be expressed in terms of E_z and H_z.

From Eq. (2.1.12), we can derived that E_z and H_z satisfy following equations,

$$\frac{\partial^2 E_z}{\partial r^2}+\frac{1}{r}\frac{\partial E_z}{\partial r}+\frac{1}{r^2}\frac{\partial^2 E_z}{\partial \varphi^2}+q^2 E_z=0 \tag{2.1.19}$$

$$\frac{\partial^2 H_z}{\partial r^2}+\frac{1}{r}\frac{\partial H_z}{\partial r}+\frac{1}{r^2}\frac{\partial^2 H_z}{\partial \varphi^2}+q^2 H_z=0 \tag{2.1.20}$$

Equations above can be solved by the separation-of-variables method, and the solution is expressed as [34],

$$E_z=\begin{cases} AJ_v(ur)e^{jv\varphi}e^{j(\omega t-\beta z)} & r<a \\ BK_v(wr)e^{jv\varphi}e^{j(\omega t-\beta z)} & r\geq a \end{cases} \tag{2.1.21}$$

$$H_z=\begin{cases} CJ_v(ur)e^{jv\varphi}e^{j(\omega t-\beta z)} & r<a \\ DK_v(wr)e^{jv\varphi}e^{j(\omega t-\beta z)} & r\geq a \end{cases} \tag{2.1.22}$$

where v = 0, 1, 2, ⋯⋯; $u^2=k_1^2-\beta^2$, $w^2=\beta^2-k_2^2$, $k_1=n_1k_0$ and $k_2=n_2k_0$. J_v is the Bessel function of the first kind of order v, and K_v is the Bessel function of the second kind. Depend on the transvers E and H fields, modes in the fiber are designated as TE, TM, EH, and HE fields.

According to boundary conditions, tangential components of EM fields, *i.e.* E_z, E_φ, H_z, and H_φ must be continuous at the core-cladding interface. Based on these conditions, the characterization equation of fiber modes can be derived as,

$$(\eta_1+\eta_2)(n_1^2\eta_1+n_2^2\eta_2)=\left(\frac{\beta v}{k_0}\right)^2\left(\frac{1}{U^2}+\frac{1}{W^2}\right)^2 \tag{2.1.23}$$

where $U=ua$, $W=wa$, and

$$\eta_1=\frac{J_v'(U)}{uJ_v(U)} \text{ and } \eta_2=\frac{K_v'(W)}{wK_v(W)} \tag{2.1.24}$$

For *weakly guiding* fiber with $\Delta=(n_1-n_2)/n_1\ll 1$, we have $k_1^2\simeq k_2^2\simeq\beta^2$. Under this approximation, Eq. (2.1.23) can be further simplified as,

$$\frac{UJ_{l-1}(U)}{J_l(U)}+\frac{WK_{l-1}(W)}{K_l(W)}=0 \tag{2.1.25}$$

where

$$l = \begin{cases} 1 & \text{for TE and TM modes} \\ \nu + 1 & \text{for EH modes} \\ \nu - 1 & \text{for HE modes} \end{cases} \tag{2.1.26}$$

Thus fiber modes degenerate and constitute LP modes in the fiber, which are designated as LP_{lm} modes, and we have:

1. Each LP_{0m} mode is derived from a HE_{1m} mode.
2. Each LP_{1m} mode is formed by TE_{0m}, TM_{0m}, and HE_{2m} modes.
3. Each LP_{lm} comes from an $HE_{l+1,m}$ and an $EH_{l-1,m}$ mode.

For each LP mode, there are two polarizations. For modes with $m \neq 0$, there are two independent azimuthal dependence with either $\cos(l\varphi)$ or $\sin(l\varphi)$. Thus, the LP mode field can be expressed in the scalar form as

$$\psi_{l,m}(r,\varphi) = \begin{cases} J_l(ur)\begin{Bmatrix}\cos(m\varphi)\\ \sin(m\varphi)\end{Bmatrix} & r < a \\ K_l(wr)J_l(ua)/K_l(wa)\begin{Bmatrix}\cos(m\varphi)\\ \sin(m\varphi)\end{Bmatrix} & r \geq a \end{cases} \tag{2.1.27}$$

Figure 2.1.2 illustrates the LP_{01} and LP_{11} mode intensity profiles in the 980-HP SMF for red laser at 632.8 nm, which is a TMF at this wavelength and used in experiments of Chapter 3 and Chapter 4.

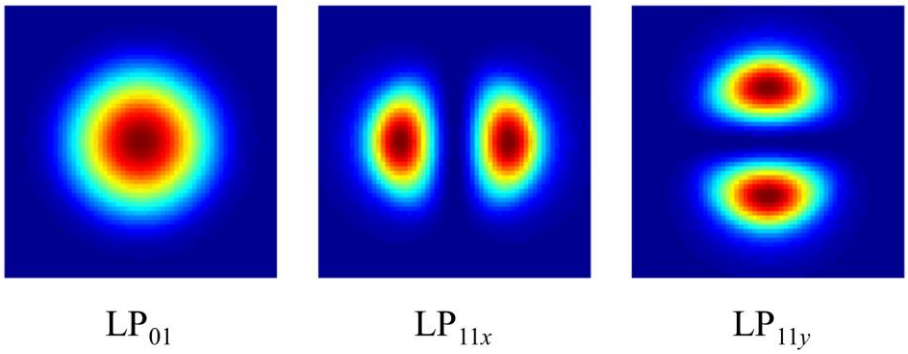

Fig. 2.1.2 Illustration of intensity profiles of the LP_{01} and LP_{11} modes in a TMF

2.2 Directional Fiber Couplers

The directional fiber coupler is an $M \times N$ fiber optical device typically used for power combining and splitting. Figure 2.2.1 shows the common construction of a 2×2 fused-fiber coupler. It is fabricated by twisting two fibers together, melting, and pulling them so they can be fused together over a uniform section, which is the mode coupling region. This coupling region typically has a length of several millimeters. As the transverse dimension gradually decreases to the coupling region, the reflection power back to the input port is neglectable, thus this device is called directional coupler.

To analyze optical power coupled from the input ports to the output ports of the directional coupler, one needs to solve the EM field distribution based on the coupled wave theory, and it is well established in a lot of books [34]. Here we simply take the results. Under the assumption that the couple is lossless and symmetric, the power coupling from Port 1 to Port 3 and Port 4 can be expressed as,

$$P_3 = P_1 \cos^2(\kappa z) \tag{2.2.1}$$

$$P_4 = P_1 \sin^2(\kappa z) \tag{2.2.2}$$

where κ is the coupling coefficient describing the power coupling between the two fibers. It is determined by the refractive indices and the fusing of the two fibers. By choosing proper length of the coupling region, the coupling power from the input port to the two output ports can be controlled accurately.

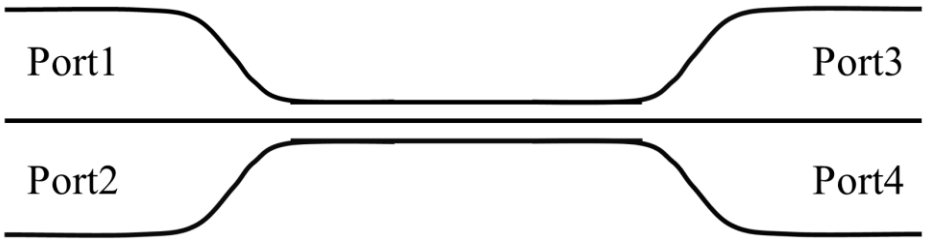

Fig. 2.2.1 Schematic illustration of a 2×2 fused-fiber coupler

Directional fiber coupler is easy to fabricate and has a lot of important applications in fiber optical communications. In addition of power combining and splitting, by combining fiber couplers with the Mach-Zehnder interferometers and FBGs, one can

build wavelength multiplexers and demultiplexers for wavelength-division multiplexing (WDM) networks. In the recently developed MDM, fiber coupler with special design can be used as mode filters [35-37]. In later experiments, we will use a directional coupler to provide feedback signals for AO-based mode control in a TMF, and details can be found in Chapter 4.

2.3 Fiber Bragg Gratings

Fiber Bragg grating is another all-fiber device with important applications in communications and sensing [34]. Based on experimental observations, ultraviolet light can induce refractive index change in germanium-doped silica fiber [38]. Thus, one can write phase gratings in fiber by creating periodic refractive index change within the fiber core. The grating can be fabricated by exposing the hydrogen-loaded fiber under the interference pattern of two ultraviolet beams. Figure 2.3.1 shows a schematic illustration of an FBG with a period of Λ and grating length of L.

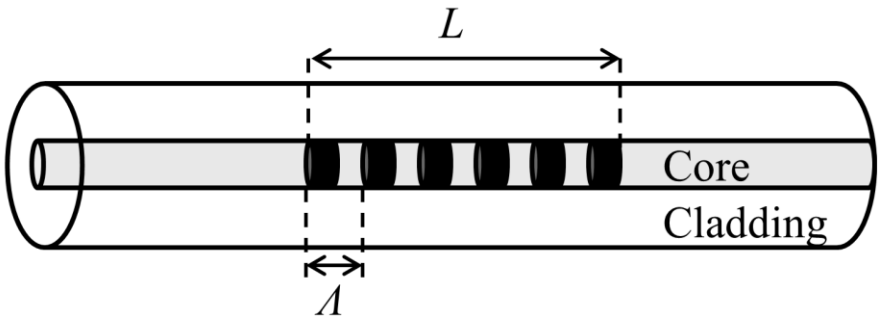

Fig. 2.3.1 Schematic illustration of an FBG

To understand the optical characteristics of an FBG, one typically employs the coupled-wave theory in periodic media to analyze the optical field in the grating [39]. For a uniform FBG in a SMF, the refractive index perturbation can be expressed as

$$\delta n_{\text{eff}}(z) = \overline{\delta n_{\text{eff}}}\left[1+\cos\left(\frac{2\pi}{\Lambda}z\right)\right] \tag{2.3.1}$$

where $\overline{\delta n_{\text{eff}}}$ is the refractive index perturbation averaged over a grating period Λ. The reflection of the FBG is solved as,

$$R = \frac{\sinh^2(sL)}{\cosh^2(sL) - \frac{\hat{\sigma}^2}{\kappa^2}} \tag{2.3.2}$$

where $\hat{\sigma}$ and κ are coupling coefficients. More specifically,

$$\kappa = \frac{\pi \overline{\delta n_{\text{eff}}}}{\lambda} \tag{2.3.3}$$

$$\hat{\sigma} = \delta + \sigma \tag{2.3.4}$$

$$\delta = \beta - \pi / \Lambda \tag{2.3.5}$$

$$\sigma = \frac{2\pi \overline{\delta n_{\text{eff}}}}{\lambda} \tag{2.3.6}$$

$$s^2 = \kappa^2 - \hat{\sigma}^2 \tag{2.3.7}$$

$\hat{\sigma}$ is the general self-coupling coefficient; δ is the detuning, representing the difference of the propagating constant between the wavelength λ, and the design wavelength (equal to $2n_{\text{eff}}\Lambda$, where n_{eff} is the effective index of the fiber mode).

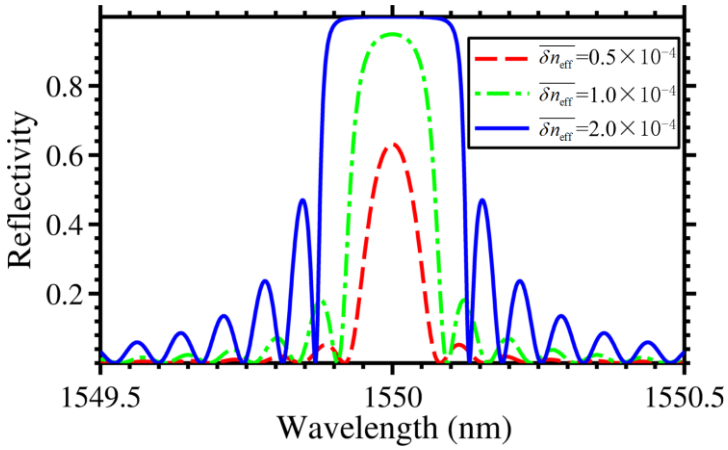

Fig. 2.3.2 Simulation results of FBG reflection spectrums with parameters Λ = 0.534 μm, L = 1.07 cm and different $\overline{\delta n_{\text{eff}}}$.

The peak reflection wavelength of the FBG can be derived from Eq. (2.3.2),

$$\lambda_B = \left(1 + \frac{\overline{\delta n_{\text{eff}}}}{n_{\text{eff}}}\right) 2n_{eff}\Lambda \simeq 2n_{eff}\Lambda \tag{2.3.8}$$

Examples of theoretical FBG reflection spectra with parameters Λ = 0.534 μm, L = 1.07 cm, and peak wavelength at 1550 nm are shown in Fig. 2.3.2.

Fiber Bragg gratings have many important applications in fiber optical communications. For example, FBGs can work as adding and dropping multiplexers in WDM [40]. It can also be used for wavelength filtering [41] and dispersion compensation [42]. In fiber optical sensing, FBGs can be used to compose quasi-distributed temperature sensor networks [43]. Other physical parameters, such as refractive index [44], can be measured by using FBGs as well. Additionally, as FBG is an all-fiber device, it has other advantages such as low cost, low loss, easy of coupling with fibers, and polarization insensitive.

2.4 Recent Applications of MMF

In this section, we briefly review recent applications of MMF in the following three aspects:

- MMF-based optical communications:

  Traditionally, MMFs have been used in fiber optical communications over short distances. In commercial systems, the data rate can reach 10 Gbit/s over length up to several hundred meters. The data rate for such system is mainly limited by the modal dispersion, *i.e.* signal of different mode groups travels at different speed within the MMF, thus causes pulse boarding and impairs the data rate. Therefore, single mode fiber is used in almost all long-haul commercial optical communication systems nowadays.

  The transmission capacity in SMF has been improved rapidly. Recent experiments have reported over 100 Tbit/s capacity in SMFs [45,46], while the input power required for maintaining the optical signal-to-noise ratio (SNR) is approaching the damage threshold [47] and nonlinearity limit [48]. In order to overcome the fast approaching capacity limit of the SMF [48, 49], “space” is explored as a new multiplexing parameter in space-division-multiplexing (SDM) to improve the transmission capacity [1-3].

One approach for implementing SDM is MDM, which utilizes individual waveguide modes within FMFs or even MMFs as communication channels for signal multiplexing and demultiplexing. The schematic of a typical MDM transmission system is shown in Figure 2.4.1. Signals for individual mode channels are multiplexed by a mode multiplexer (MUX) and sent into the MMF. A multimode fiber amplifier is used to amplify signals of individual mode channels. At the receiver side, a mode demultiplexer (DMUX) is used to separate signals into individual mode channels, and the signals are detected by coherent receivers (Co-Rx). As cross-talk exists between individual mode channels within the MMF, a MIMO digital signal processors (DSP) is usually required for recovering signals of individual channels. In most of recent MDM demonstrations, the optical fiber is actual a TMF supporting only the LP_{01} and LP_{11} modes.

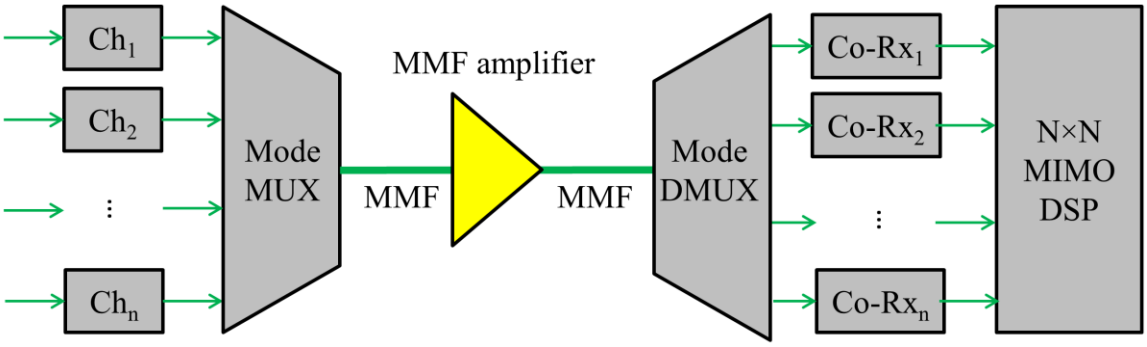

Fig. 2.4.1 Schematic of a typical MDM transmission system

The concept of MDM was first proposed by Berdague et. al. in 1982 [50]. MDM is demonstrated by using two high-order fiber modes in a 10 meter graded-index MMF with a core of 25 μm. In 2000, Stuart realized the MIMO technique developed in wireless communications can be used in optical communications, and experiment results applying 2×2 MIMO for two MDM channels were shown [51]. Since then, more proof-of-concept experiments by applying MIMO in MDM have been demonstrated [52-54]. With the help of the recent development of FMFs, MDM improves rapidly. In early 2011, MDM experiments with over 100Gb/s per channel rate up to 40 km have been demonstrated by using the LP_{01} and LP_{11} modes in FMF [5, 6]. Experiments also show that one can apply full degrees of freedom of the LP_{01} and LP_{11} modes in MDM [4, 55]. By combining MDM with other multiplexing

techniques such as WDM and polarization-division-multiplexing, the data rate of the optical communication system can be further improved [56]. Few-mode Erbium-doped fiber amplifiers (EDFAs) are also developed for amplifying signals in MDM transmission systems [57,18].

- MMF-based sensing:

  Comparing with SMF-based sensors, MMF-based optical sensors have advantages such as low-cost, high sensitivity, and discrimination capability for more than one sensing parameters [58]. In 1980s, MMFs have been initially applied in different types of optical sensors [59, 60]. In [59], An MMF displacement sensor is demonstrated based on micro-bending induced mode coupling between core and cladding modes. This technique has been widely used in subsequent displacement sensors. For example, one recent sensors based on micro-bend MMF has been applied in medical devices for measuring breathing and heart rates [61]. In [60], sensors based on the classic SMF-MMF-SMF (SMS) structure and interference between modes in the MMF are proposed. Various sensors based on the SMS structure have been developed for measuring strain [62], temperature [63, 64], refractive index [65], and curvature [66] *et. al.* MMF-based sensors using other mechanism have also been investigated recently, such as multimode FBGs [67-73] and SBS [12, 74-76]. Base on multimode FBGs, sensors for simultaneous measurement of strain and temperature [70], refractive index and temperature [71, 72], and strain and bending have been reported [73]. In addition, multimode FBG based sensors can be used to compose quasi-distributed sensing networks for measuring multiple environment parameters at multiple locations. Distributed sensor network based on SBS has also been studied for simultaneous temperature and strain measurement [76]. The principle is that, for different LP modes (the LP_{01} and LP_{11} modes), the Brillouin frequency shifts (BFSs) caused by temperature and strain are different. Thus, one can measure the temperature and strain simultaneously by measuring the BFSs of two different spatial modes. This technique can also be adapted to measure the intermodal coupling in FMFs [77].

- MMF-based imaging:

  Due to modal scrambling in MMF, image transferring through a MMF is severely distorted, and the output at the receiver end of the MMF is a random speckle pattern.

Though experiments have shown that the modal scrambling in MMF can be compensated in as early as 1967 [78], MMF-based imaging has not attracted great interests in the last few decades. The renewed interests in MMF-based imaging are aroused from the recent progress of AO [23-30], which will be discussed in details in Section 2.6. Briefly, recent researches show that it is possible to focusing through turbid media by optimizing the wavefront [23], and turbid media with strong scattering can be characterized by TMs [25]. Realizing the analogy of turbid media and MMFs, several groups have demonstrated that, by calibrating the TM of a MMF-based imaging system in advance, original images can be retrieved from the distorted ones [7, 8, 79].

Different techniques have been applied to characterize the TM in a MMF, including computer-generated-holography (CGH) [7, 9, 80], optical-phase-conjugation (OPC) [8], and spatial-spectral encoding [81, 82]. Based on these techniques, various imaging modalities such as confocal microscope [83, 84], fluorescence microscope [7, 85], two photon microscope [86], light sheet microscope [87] via MMF have been demonstrated subsequently. These techniques can also be used to improve the resolution of fiber-bundle based endoscope [88], manipulate particles [9] and cells [89]. By taking advantages of scattering media in MMF-based imaging, the numerical aperture of the MMF-based imaging system can be enhanced, which is important for improving both the resolution and field-of-view of the MMF-based imaging systems [90, 91]. Several other aspects of MMF-based imaging systems are actively under research, such as imaging through MMFs without accessing the fiber distal end [92], and dynamic compensation of the fiber bending [93, 94]. Algorithms for reducing noise in MMF-based imaging have been studied recently as well [95]. Comparing to current fiber-bundle based systems, the MMF-based imaging setup is scanless, miniature, and potentially has high-resolution.

2.5 Mode Control Methods in MDM

A key component of MDM is the excitation of specific waveguide mode in a MMF. As mentioned in Chapter 1, this task can be accomplished using multiple techniques, such as LPGs, spot-based couplers, phase masks, photonic lanterns, or SLMs et. al.

In the first paper MDM proposed in 1982, selective mode excitation is accomplished by using a spatial filter matching the field patterns of two high-order modes in a MMF [50]. In later demonstration of MDM experiments, phase plates are widely used [4, 18, 57]. The principle is similar to the spatial filter method, but this time it works in phase domain [57]. By using a phase plate to match the phase of the optical field of desired fiber mode, the target mode is exited in the MMF. Phase plates can be batch-fabricated with high resolution by photolithograph, thus they are widely used in MDM experiments. The drawback of phase plates is the high insertion loss and cross-talk. Though the phase of light can be well-matched with the desired mode, its amplitude mismatch still excites undesired modes into the MMF, thus creates crosstalk between different mode channels.

Spot-based mode coupler is another interesting device for MDM [13]. The principle is based on that, for MMFs with relative large diameter, one can excite desired modes by controlling the spatial positions of the beam spots focusing on to the MMF facet. With proper configuration of the beam spot radius, positions and relative phases, selectively excitation of different LP modes can be achieved. Spot-based mode coupler supports a large number of modes with low insertion loss.

"Photonic lantern" can be considered as an extension of the spot-based mode coupler. It is initially used in astronomy to increase the system aperture while remaining single mode performance [15-17, 96-98]. A standard photonic lantern is fabricated by inserting a bundle of SMFs into a low-index capillary tube, and adiabatically tapping down them to form a new MMF, in which the SMF core vanishes and the SMF cladding becomes the new core and the capillary tube becomes the cladding [98]. Light can be coupled between SMFs and the MMF via the gradual taper transition, and orthogonal combination of modes is excited in the MMF. At the receiver side, the same photonic lantern can be used as mode demultiplexer, and signals from individual channels can be retrieved by using the MIMO DSP. Photonic lantern is theoretically lossless, and low-loss mode multiplexers based on photonic lantern have been demonstrated [16]. By choosing dissimilar SMF to fabricate the photonic lantern, mode selective photonic lantern can be built, in which launching light in different SMF will excited different fiber modes in the MMF [97]. The most important advantage of photonic lantern is that it supports a large

number of channels without increasing loss. Experimentally, a photonic lantern supporting 12 FMF modes has been demonstrated [17].

For all above mode multiplexers, they can basically be categorized as spatial matching type. Another group of mode multiplexers are based on mode coupling with phase matching. One of such mode convertor is the fiber LPG [6, 99]. LPG-based mode convertor has been used in early MDM experiments [99]. By pressing a metallic mask grating on the TMF, LPG can be formed in the TMF for mode conversion between LP_{01} and LP_{11} modes. Additionally, mode selective couplers (MSCs) based on phase matching are developed as mode multiplexers in MDM [35-37]. The structure of a typical MSC includes a SMF and a FMF. By proper pre-pulling techniques, phase matching conditions can be satisfied at the coupling region of the MSC, and mode multiplexing /demultiplexing can be accomplished in the FMF. MSCs provide an all-fiber solution for mode multiplexing and demultiplxing. They can be easily fabricated with low-loss, low-cost and high reliability. Similar to MSCs, mode multiplexer/demultiplexer can be fabricated with planar waveguide structures. Various silicon waveguide based on-chip mode-division multiplexer have been demonstrated [100-102].

For all these methods mentioned above, they are "static" mode control techniques. Dynamic and adaptive mode control can be accomplished based on CGH [5, 19, 20, 31, 33]. By placing the SLM on the Fourier plane of the fiber proximal end, one can calculate the desire phase patterns matching specific LP modes simply by Fourier transform, and show that on the SLM for selective excitation of fiber modes in MMFs. Both phase-only [19, 31] and amplitude-and-phase [20] based holography has been investigated for selective mode excitation. Optimization algorithms have been applied for finding the optimal holography patterns [19]. The CGH-based mode multiplexer/demultipler is dynamic. It has low cross-talk, while proper alignment might be required. Our AO-based mode control method is different from the CGH-based method, and details can be found in Section 2.7.

Additionally, optical orbital angular momentum-based [103] and SMF-MMF-FMF structure based [104] multiplexers have also been reported in recent research.

2.6 Recent Development of AO

Adaptive optics is widely used in astronomy to correct the aberration introduced by atmospheric turbulence in the optical path [105, 106]. Generally, the aberration is measured from a "guidestar", which could be either a real star or a virtual one created by laser in the sky. The measured aberration can be compensated by using AO devices for sharper images, such as using deformable mirrors (DMs).

For systems with strong scattering, for example in turbid media, the optical field is complexly scrambled, and it is impossible to use AO techniques well-established in astronomy to control light propagating in such systems. However, the recent developed "wavefront shaping" techniques demonstrate successful coherent control of scattering light in turbid media [23]. Although there are some differences between "wavefront shaping" techniques and AO in astronomy, they are both based on AO devices, such as SLMs and DMs. Thus, we still categorize the "wavefront shaping" techniques in AO.

The first experiment demonstrated wavefront shaping in scattering media is carried out by Vellekoop et.al. in 2007 [23], in which they show that one can focus light through opaque scattering media by utilizing a SLM to control the wavefront of the incident light. The schematic illustrations of light propagating in the turbid media before and after wavefront shaping are shown in Figs. 2.6.1(a) and 2.6.1(b) [23]. The principle is based on the linear relationship between the incident and scattered fields during the scattering process. If we divide the wavefront into N different segments, the light intensity at the target position behind the turbid media is a linear combination of scattered fields coming from N different wavefront segments as

$$E_m = \sum_{n=1}^{N} t_{mn} A_n e^{i\phi_n} \tag{2.7.1}$$

where A_n and ϕ_n are amplitude and phase of light from the nth wavefront segment respectively, E_m is the field at the target position behind the turbid media. As shown in Figs. 2.6.1(c) and 2.6.1(d), by adjusting the phases of individual wavefront segments, we can "line up" the scattered fields from individual wavefront segment to form constructive

inference (green arrow), which is significantly stronger than the combination result of the filed at the target position before wavefront shaping (red arrow).

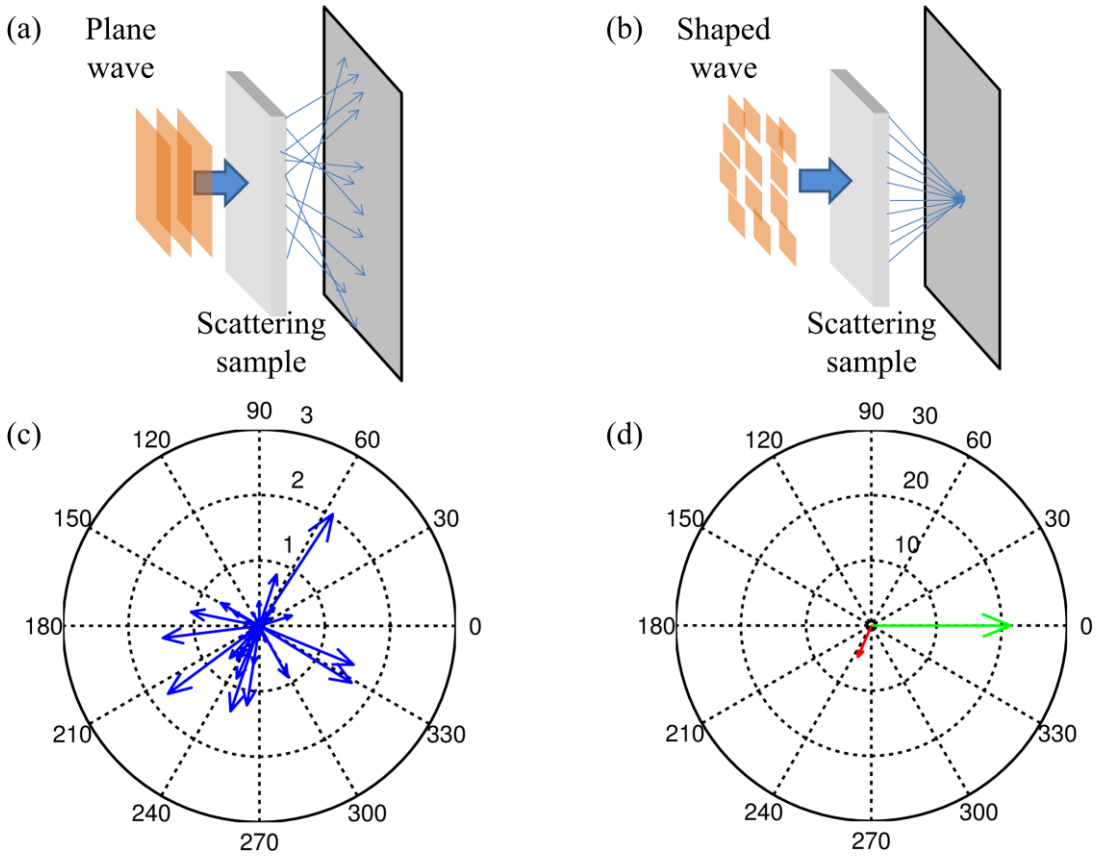

Fig. 2.6.1 Principle of wavefront shaping in turbid media. Light propagation (a) before and (b) after wavefront shaping; Schematic illustration of (c) the distribution of scattered fields from individual wavefront segments; and (d) optical field at the target position before (red) and after (green) wavefront shaping.

In order to find the optimal wavefront, Vellekoop et.al. apply three different optimization algorithms in [24]: stepwise sequential, continuous sequential, and random partition algorithms. The stepwise sequential algorithm can be described as the following: iteratively vary the phase of each wavefront segment from 0 to 2π, and record the intensity versus the phase at the target position. For each wavefront segment, record its optimal phase as the one maximizing the intensity. After this process is performed for all wavefront segments, set the phase of each wavefront segment to its optimal value. Repeat this process until the light intensity at the target position converges. The continuous sequential algorithm is similar to the stepwise algorithm. The only difference is that the

phase value of each wavefront segment is updated to the optimal value at the end of each wavefront segment optimization. The random partition algorithm can potentially improve the system SNR during phase optimization, in which wavefront shaping is carried out by randomly choosing half of the wavefront segments for phase optimization.

The scattering media virtually improve the numerical aperture of the system. Experiment results have demonstrated sub-diffraction-limit focusing through turbid media [107, 108]. This conclusion potentially enables high-resolution imaging in turbid media with deep penetration. In order to form an image, one needs to focus light at multiple target positions on the object plane behind or within the turbid media. However, due to the random scattering process in turbid media, wavefront shaping for focusing through turbid media is highly position dependent.

There are mainly two approaches to solve this problem. The first method takes advantages of the linear relationship between the incident and scattered fields, and the scattering of the turbid medium is characterized as a TM in advance [25]. The first experiment measuring the TM of a turbid medium is demonstrated by Popoff et. al., and the method is based on phase modulation together with full-field interference [25]. In MMF-based imaging, the TM is mainly measured by using holography [7, 9] or OPC [8]. The holography based approach usually works with full-field interference together [9]. By varying the phase of individual wavefront segment, one can retrieve its amplitude and phase dependence with all target positions simultaneously by using interference, thus the TM can be retrieved after this measurement is carried out for all wavefront segments. Optical phase conjugation is another popular method for wavefront shaping in both turbid media and MMF. Briefly, for measuring the TM of a MMF (in turbid media, it is similar), a point light source is created at the distal end of the MMF (by focusing), and the phase information of light propagating to the proximal end can be retrieved by off-axis holograph. By showing the conjugate phase on the SLM, light from the proximal end can be focused at the distal end. Spatially scanning the point source, the corresponding phase pattern for each spatial position can be acquired. Afterwards, the TM can be derived from the group of phase patterns.

The other approach for imaging through turbid media is based on the optical “memory effect”, which has been known since 1988 [109, 110]. Simply, tilting the incident

wavefront leads to corresponding tilt of the transmitted field. Thus, once a focus is created within/behind the turbid media, it can be scanned across without significant decorrelation by simply tilting the corrected wavefront, up to an angle known as the memory effect angle. Fluorescent microscopes based on this principle have been demonstrated with high resolution and deep penetration [29, 30]. Both OPC and optimization based approach can be applied to create the focus and both methods require a guidestar. In deep tissue imaging, guidestars created by utilizing the photo-acoustic effect and nonlinear process, such as two-photon fluorescence emission and second harmonic generation, have been demonstrated [111-113].

For optimization based wavefront shaping, the optimization algorithm plays important roles. Significant efforts have been devoted to improving the wavefront optimization speed. Some researches focus on finding better optimization algorithms, for example, the coordinate descent algorithm [114] and the genetic algorithm [115] have been demonstrated for fast wavefront shaping. Some researchers simply improve the optimization speed by using fast hardware such as FPGA for signal processing [116]. Cui proposed an interesting parallel algorithm for wavefront optimization, in which each wavefront segment has a unique phase modulation frequency, and the optimization is simultaneously carried out for all wavefront segments. The optimal phase value for individual wavefront segment can be extracted by taking the Fourier transform of the intensity signals. This algorithm has been successfully applied in both turbid media focus [26] and deep tissue imaging [112], and it significantly shortens the time required for phase optimization. The wavefront optimization is mainly affected by the phase modulation element (AO devices). To date, the fastest optimization experiment takes 33.8 ms to create focus through turbid media or MMF with 256 wavefront segments [27, 116].

2.7 Principle of AO based Mode Control in TMF

The AO-based mode control method developed in this thesis is very similar to those used in astronomy and scattering medium focusing [23, 24]. The general idea is illustrated in Fig. 2.7.1. It requires a feedback signal that is directly associated to desired mode properties. For example, in Chapter 3, the desired outcome is that the optical field at the

fiber output becomes specific LP modes or their combinations, and the feedback signal is simply the correlation between the desired mode profile and the optical field distribution captured by a CCD camera. In Chapter 4, we use a directional coupler for AO-based mode control, and the feedback signal is the power coupling ratio of the directional coupler. In Chapter 5 and 6, the feedback signal becomes the ratio of the transmission power and the reflection power from an FBG. Potential candidates for feedback signals, however, are by no means restricted to these particular choices. In the future, the feedback signal could be nonlinear signals generated by processes such as Brillouin scattering, Raman scattering, and four-wave mixing.

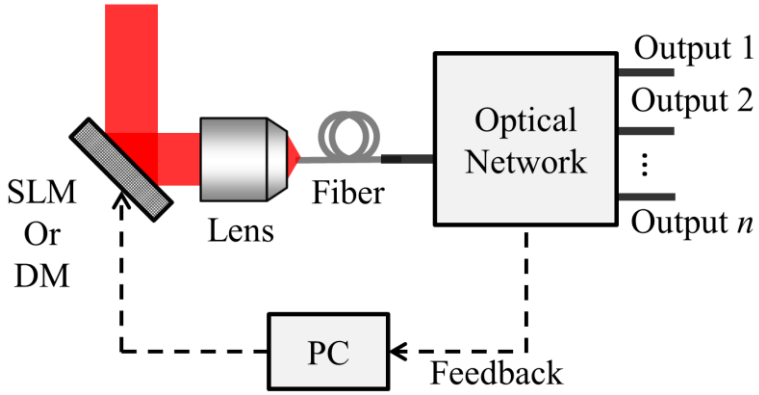

Fig. 2.7.1 Principal of AO-based mode control

With proper feedback signals $f(k)$, we can use the SLM or DM to modify the wavefront and measure $f(k)$ produced by the new wavefront. The modified wavefront is retained (or rejected) depending on whether the feedback signal suggests better (or worse) match between the measured outcome and the desired target. This optimization cycle is repeated until the desired target is reached.

The optimization procedure basically follows the continuous sequential algorithm in [24]. We choose the continuous sequential algorithm instead of others because: It is easy to implement, comparing with other complex algorithms such as the genetic algorithm [115], and the parallel optimization algorithm [26] requires advanced devices. As shown in Fig. 2.7.2, the optical wavefront is divided to $N \times N$ blocks, and the wavefront of each of the block can be modulated independently in M different phase shifts between 0 to 2π for wavefront control. The system feedback signal $f(k)$ can be treated as the combination of the feedback signals from each of the phase modulation blocks. Each block is optimized

individually using the sequence shown in Fig. 2.7.2. During the optimization process, we change the phase shift of one, and only one phase block. As we cycle the phase shift ϕ of each block from 0 to 2π, the feedback signal $f(k)$ changes accordingly. After obtaining the M objective functions produced by the M different phase shifts, we set the phase shift of the current block to the one that minimizes/maximizes the objective function (ϕ_k). Then, we move to the next phase block and repeat this optimization procedure. This optimization process is sequentially carried out for all phase blocks, and is referred to as one optimization cycle.

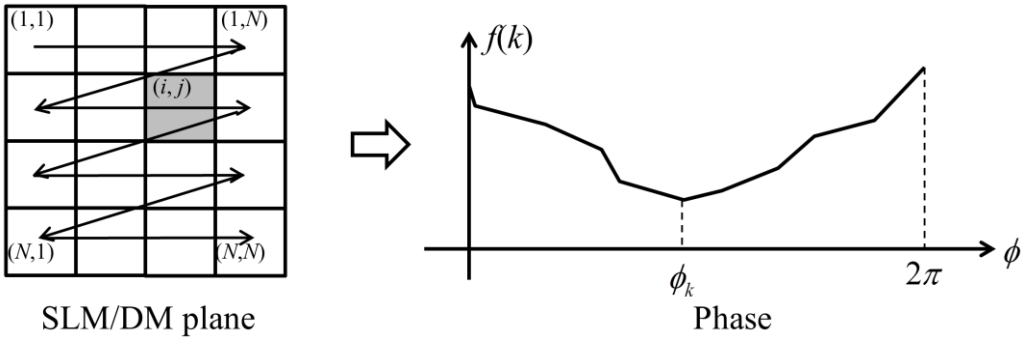

Fig. 2.7.2 Illustration of the optimization algorithm for AO-based mode control

Comparing with existing mode control methods in Section 2.5, the AO-based mode control method developed in this thesis has several advantages. First of all, the method requires no prior knowledge of the optical system or the intermodal coupling within the fiber network. In fact, our method treats the entire optical system, including both the input coupling system and the TMF itself, as a "black box". In contrast, methods reported in [5, 19, 20, 31, 33] require knowledge of the optical system and are based on linking optical near field to far field through a Fourier transform. Second, the method developed here can be used to control mode *within* the TMF as long as there is an appropriate feedback signal associated with the mode filed *within* the TMF network, while in existing literature most of the mode control methods can only excite specific mode either at the input or output ports of the fiber. In addition, the method developed here is dynamic and versatile.

Chapter 3

Adaptive Mode Control Based on Mode Correlation Functions

The main goal of this chapter is to develop a generic AO algorithm for mode control. As a proof-of-concept demonstration, we choose a simple feedback function, which is based on the correlation between the spatial profile of the desired waveguide mode (i.e., target) and the guided wave images at a specific location (the distal end of the TMF), as measured by a CCD camera. The feedback requires direct imaging of the fiber distal end, and we only use this feedback function to demonstrate the feasibility of AO-based mode control in this chapter. In the next few chapters, we will extend the image-based approach into an intensity-based approach, where AO-based mode control is implemented using a directional coupler or an FBG, which are more suitable for applications involving complex multimode networks.

3.1 Experiment Setup and AO Algorithm

The experimental system is shown in Fig. 3.1.1. Light from a linearly polarized He-Ne laser (632.8nm) is collimated and expanded. The expanded beam is reflected by a phase-only SLM (Holoeye, Pluto) and focused into a silica fiber (Thorlabs 980HP, length approximately 1.5m) using an objective lens (20×, NA=0.40). At the output plane of the fiber, a second objective lens (100×, NA=0.70) and a CCD camera (Stingray F-145B) are used to measure the output intensity profile, which will be used as the feedback signal.
The light polarization in the system is controlled by a half-wave plate and three polarizers. The first two polarizers (P1 and P2) select optical waves with polarization direction

parallel to the optical table, which also coincides with the phase modulation axis of the SLM. The polarizer in front of the CCD (P3) ensures that we only monitor a single polarization component of the optical output. The polarization direction of P3 is randomly chosen without being orthogonal to P2. The expanded He-Ne laser beam is projected onto the SLM. The total area of SLM pixels that can be phase modulated is approximately 6.2 mm by 6.2 mm. The size of the expanded beam is similar. The SLM modulation area is evenly divided into 13×13 phase blocks to control the wavefront of the incident beam. Within each phase block, the phase shifts produced by the SLM are identical. The fiber is a TMF that supports the LP_{01} and the LP_{11} modes. (The fiber's normalized frequency is V=3.57 at the operation wavelength according to the specification).

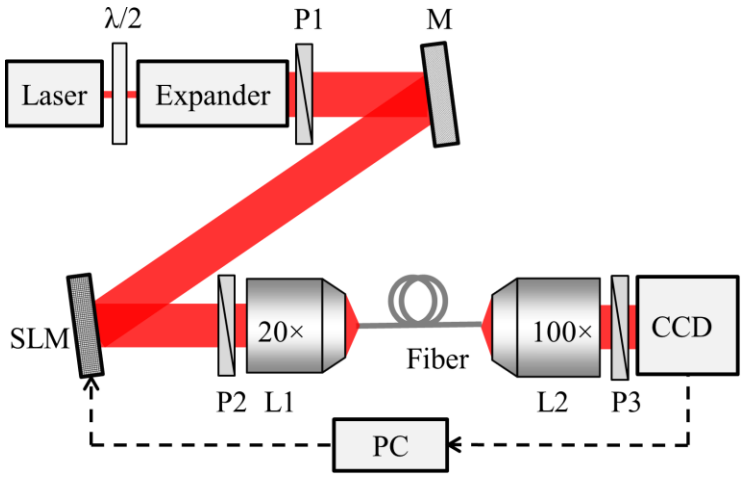

Fig. 3.1.1 Schematic of the setup: $\lambda/2$, half-wave plate; Expander, 1:5 beam expander comprise of two lenses; M, mirror; SLM, phase-only spatial light modulator; P1, P2 and P3, polarizer; L1, 20× objective lens, NA=0.40; Fiber, Thorlabs 980HP, ~1.5m; L2, 100× objective lens, NA=0.70; CCD, CCD camera.

AO-based mode control is carried out as follows. From the fiber specification, we can theoretically calculate the desired target profile at the fiber output. More specifically, a linear combination of the LP_{01} and the LP_{11} modes with a specific polarization can be expressed as:

$$\begin{aligned} I(r,\varphi) &= \left| A_{01}E_{01}(r,\varphi)e^{-j\beta} + A_{11}E_{11}(r,\varphi) \right|^2 \\ &= A_{01}^2E_{01}^2(r,\varphi) + A_{11}^2E_{11}^2(r,\varphi) + 2A_{01}A_{11}\cos\beta E_{01}(r,\varphi)E_{11}(r,\varphi) \end{aligned} \tag{3.1.1}$$

Here $E_{01}(r, \varphi)$ and $E_{11}(r, \varphi)$ denote electric fields of the LP_{01} and LP_{11} modes with a specific polarization, respectively. A_{01} and A_{11} are the amplitudes of two modes, and β represents their relative phase difference. To simplify the procedure for mode decomposition in later sections, we assume both $E_{01}(r, \varphi)$ and $E_{11}(r, \varphi)$ to be real.

With the theoretical mode profile known, we can calculate the correlation between the target intensity profile and the measured intensity profile at the fiber output, and use this correlation function as the feedback for mode control. Specifically, we define an objective function based on the CCD intensity profile I_k and the target intensity profile I_0:

$$f(k) = 1 - \frac{\sum (I_0(x,y) - \overline{I_0})(I_k(x,y) - \overline{I_k})}{\sqrt{\sum (I_0(x,y) - \overline{I_0})^2 \sum (I_k(x,y) - \overline{I_k})^2}} \tag{3.1.2}$$

where $\overline{I_0}$ and $\overline{I_k}$ are the average of I_0 and I_k, respectively. According to Eq. (3.1.2), it is clear that the optimization function $f(k)$ quantitatively described the difference between the actual CCD intensity profile and the desired target, with smaller $f(k)$ indicating better match. Ideally, if the CCD intensity profile forms a perfect match with the target profile, $f(k)$ should become 0.

The optimization procedure follows the optimization algorithm described in Chapter 2.7. In our case, mode control is achieved by adjusting the SLM to minimize the objective function $f(k)$ defined in Eq. (3.1.2). The SLM is grouped into 13×13 equally sized blocks. Upon reflection, every block can produce 11 different phase shifts between 0 to 2π for wavefront control. Every block is optimized individually using the sequence shown in Fig. 2.7.2. During the optimization process, we change the phase shift of one, and only one phase block. As we cycle the phase shift of each block from 0 to 2π, the optical intensity at the fiber output changes accordingly. In particular, at each phase level, we use the intensity profile captured by the CCD camera to calculate the optimization function $f(k)$, which should depend on the value of the phase shift. After obtaining the 11 objective functions produced by the 11 different phase shifts, we fix the phase shift of the current block to the one that minimizes the objective function. Then, we move to the next phase block and repeat this optimization procedure. This optimization process is sequentially carried out for all phase blocks, and we repeat this optimization process for 7 cycles. The time required for one optimization cycle with 13×13 phase blocks is roughly 192 s. In

future, faster algorithms and methods described in Section 2.6 should significantly improve the speed of selective mode excitation.

3.2 Experiment Results

By using the experimental setup and adaptive algorithm described above, we have adaptively controlled the optical field at the fiber output. During the experiment, only the optical field within or near the fiber core (approximately 5.4 μm ×5.4 μm in size) is used in the evaluation of the optimization function. (It corresponds to a 61×61 pixel block in the CCD image. The fiber core, with a radius of 1.8 μm, is completely contained within this region.) In our studies, we considered three different cases. In case 1 and 2, we adaptively covert the optical mode at the fiber output to be either purely LP_{01} (in case 1) or purely LP_{11} (in case 2). Then, in case 3, we excite a mixture of LP_{01} and LP_{11} modes with pre-determined mode coefficients.

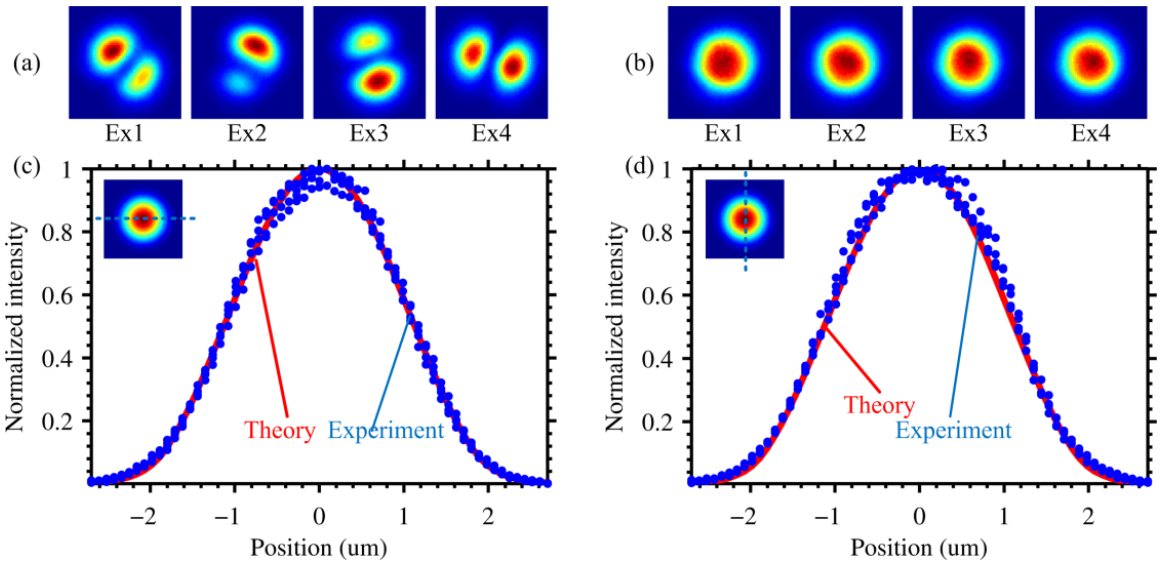

Fig. 3.2.1 Selective excitation of the LP_{01} mode. (a) and (b) show the initial and optimized field distributions at the TMF output for four representative experiments (Ex1-Ex4); (c) and (d) show the horizontal and the vertical cross-section of the intensity profiles (along the dashed blue line in the inset) of both the theoretical target (solid line) and the experiment results (dots), respectively.

The results for case 1, i.e., exciting only the LP_{01} mode, are shown in Fig. 3.2.1. Figures 3.2.1(a) and 3.2.1(b) show the initial and optimized optical intensity profiles at the TMF output for four representative experiments (labelled Ex1 to Ex4) with randomly selected initial filed distributions. The difference between the optimized intensity distribution and the theoretical target is less than 0.19% for all four cases. The cross-sections of the optimized field intensity (as captured by the CCD camera, represented as dots) and the theoretical target (represented as solid lines) are shown in Figs. 3.2.1(c) and 3.2.1(d). After optimization, the agreement between the actual mode profile and the theoretical target is excellent.

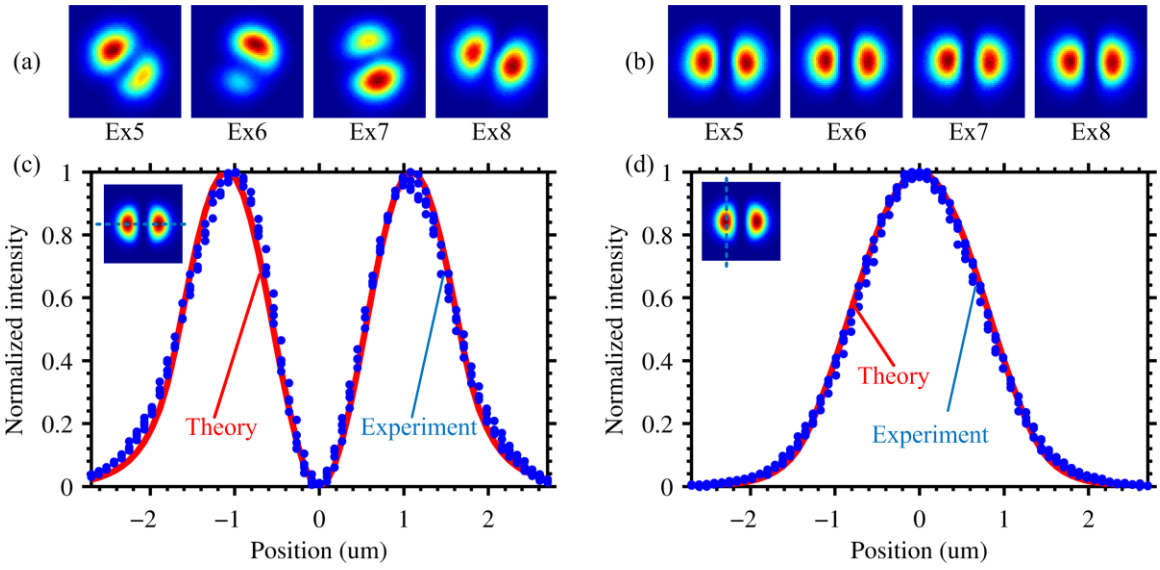

Fig. 3.2.2 Selective excitation of the LP_{11} mode. (a) and (b) show the initial and optimized field distributions at the TMF output for four representative experiments (Ex5-Ex8); (c) and (d) show the horizontal and the vertical cross-section (along the dashed blue line in the inset) of the intensity profiles for both the theoretical target (solid line) and the experiment results (dots), respectively.

Figure 3.2.2 shows experimental results for case 2, where we excite only the LP_{11} mode at the fiber output. Again, Figs. 3.2.2(a) and 3.2.2(b) show initial and optimized optical intensity profiles at the TMF output for four representative experimental studies with different initial intensity profiles. After optimization, the difference between the actual CCD camera image and the theoretical target is less than 0.75% for all four cases. As

previously, the cross-sections of theoretical and actual "after" optimization mode profiles are shown in Figs. 3.2.2(c) and 3.2.2(d).

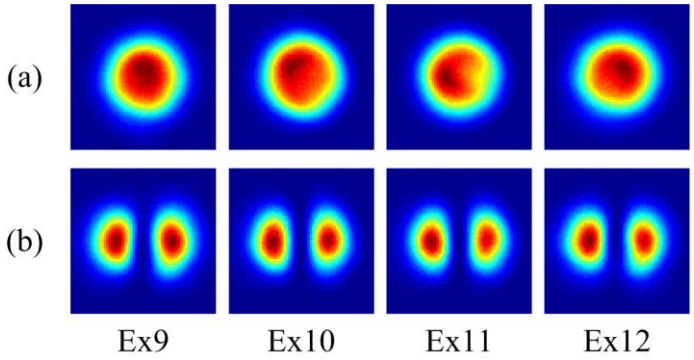

Fig. 3.2.3 Converting the LP_{01} mode (shown as the initial distributions in (a)) to the LP_{11} mode (shown as the optimized intensity profiles in (b)). Figures labeled as the same experiment number belong to the same optimization process.

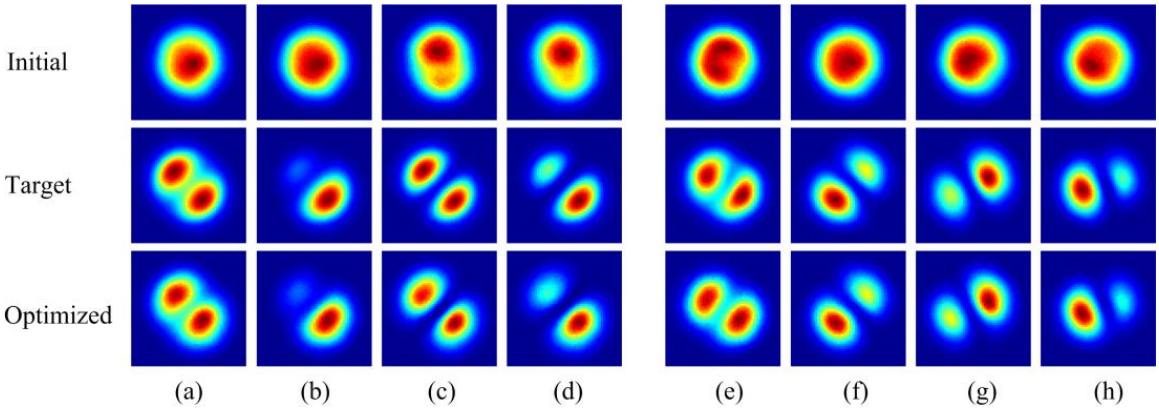

Fig. 3.2.4 Excitation of a specific mixture of the LP_{01} and the LP_{11} modes. Targets in (a) to (d) are obtained through theoretical calculations, with specific amplitude ratios (AR=A_{01}/A_{11}) and phase differences β, as defined in Eq. (3.1.1). (a) AR=0.5, $\beta=\pi/2$. (b) AR=0.5, $\beta=\pi/4$ (c) AR=0.2, $\beta=\pi/2$. (d) AR=0.2, $\beta=\pi/4$. In (e)-(f), we choose four representative CCD camera images, captured experimentally, as the targets used in the optimization process.

Results in Figs. 3.2.1 and 3.2.2 demonstrate that the AO-based approach can produce either the LP_{01} or the LP_{11} mode with very high selectivity, regardless of the initial mode profiles. Next, we consider, in some sense, the worst case scenario, where we deliberately choose the LP_{01} mode as the initial profile and select the LP_{11} mode as our target. The

"before" and "after" optimization images, as captured by the CCD camera, are shown in Figs. 3.2.3(a) and 3.2.3(b). Again, it is clear that we can achieve complete mode conversion from the LP_{01} to the LP_{11} mode.

Finally, we consider case 3, where we use the adaptive algorithm to excite a superposition of LP_{01} and LP_{11} modes. The results are shown in Fig. 3.2.4. In Figs. 3.2.4(a)-3.2.4(d), the target intensity profiles are generated using the theoretical LP_{01} and LP_{11} mode profiles with different amplitude ratios and phase contrasts. The difference between theoretical targets and actual CCD camera images are less than 1%. In Figs. 3.2.4(e)-3.2.4(h), we use some arbitrarily chosen CCD camera images as target profiles. The differences between the target profile and the "optimized" results are less than 0.7% for all four cases.

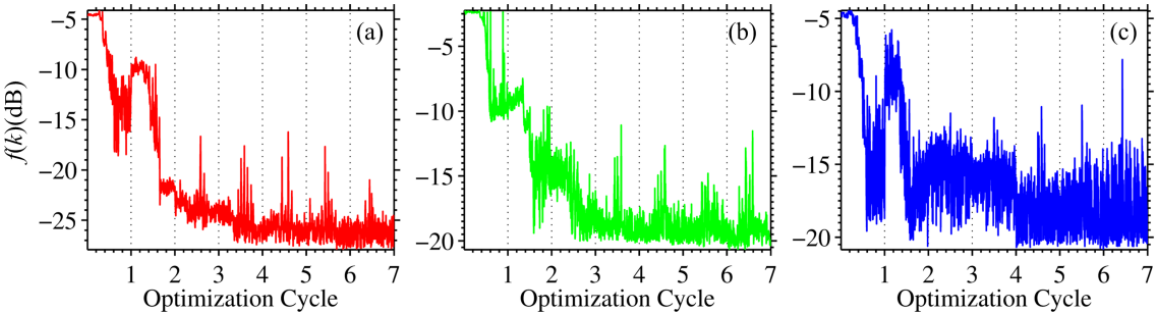

Fig. 3.2.5 Variations of the objective functions obtained during the optimization processes: (a) Optimize the mode to LP_{01} mode; (b) Optimize the mode to LP_{11} mode; (c) Optimize towards a mixed LP_{01}/LP_{11} mode.

Figure 3.2.5 shows the variations of objective functions during seven optimization cycles. We consider three different cases, with the LP_{01} mode being the target in Fig. 3.2.5(a), the LP_{11} mode as the target in Fig. 3.2.5(b), and a mixed mode as the target in Fig. 3.2.5(c). All results in Fig. 3.2.5 are divided into individual cycles, as indicated by the dashed lines. Within each cycle, the objective function exhibits significant variations as we adjust the phase shift for each of the 13×13 SLM blocks. This is to be expected, since for any SLM block, a "wrong" phase shift can certainly increase the difference between the captured CCD image and the target profile. Furthermore, recall that for each optimization cycle, we use the minimum value of the objective function to determine the optimal phase shift for the desired incident wavefront. Consequently, the results in Fig.

3.2.5 suggest that it only takes 3-4 cycles to reach the optimal wavefront for selective mode excitation. After seven optimization cycles, the deviation between the actual CCD image and the target profile are less than -27 dB for the LP_{01} case and fewer than -20 dB case for the LP_{11} case. Several factors may account for the differences between the theoretical targets and the actual optimized field distributions. For example, the actual index distribution of the fiber may not be the simple step-index profile assumed in our theoretical calculations. Additionally, the fiber output facet may not be perfectly flat, which can also cause deviations between the theoretical target profiles and the CCD camera images.

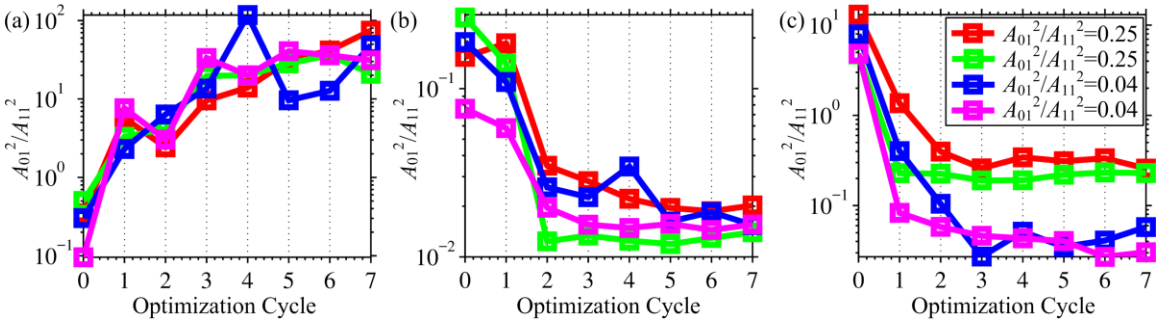

Fig. 3.2.6 Variations of mode ratios A_{01}^2/A_{11}^2 during the optimization cycles. Mode is shaping to (a) LP_{01} mode, (b) LP_{11} mode, and (c) mixed modes. The legend in (c) shows the mode ratios A_{01}^2/A_{11}^2 of the targets used in optimization.

We also analyze the mode profiles captured by the CCD camera after each optimization cycle. Specifically, we decomposed the CCD image into a linear superposition of the LP_{01} and the LP_{11} mode components. The square of the amplitude ratios of LP_{01} mode to LP_{11} mode are shown in Fig. 3.2.6. Figures 3.2.6(a) and 3.2.6(b) confirms that after optimization, the optical mode at the fiber output is clearly dominated by the desired target, i.e., LP_{01} for Fig. 3.2.6(a) and LP_{11} for Fig. 3.2.6(b). Figure 3.2.6(c) shows the mode decomposition results of the four cases shown in Figs. 3.2.4(a)-3.2.4(d), where we use a mixed mode as the optimization target. In Figs. 3.2.4(a) and 3.2.4(b), the target mode amplitude ratio between the LP_{01} and the LP_{11} mode is A_{01}/A_{11}=0.5. The corresponding values of A_{01}^2/A_{11}^2 measured during the optimization process, are shown as the red and green lines in Fig. 3.2.6(c). In Figs. 3.2.4(c) and 3.2.4(d) the target mode amplitude ratio is A_{01}/A_{11}=0.2, and the corresponding values of A_{01}^2/A_{11}^2 measured during

the optimization processes, are represented as the blue and magenta lines in Fig. 3.2.6(c). Results in Fig. 3.2.6 also suggest that we can reach the LP modes or their mixtures after only 3-4 optimization cycles.

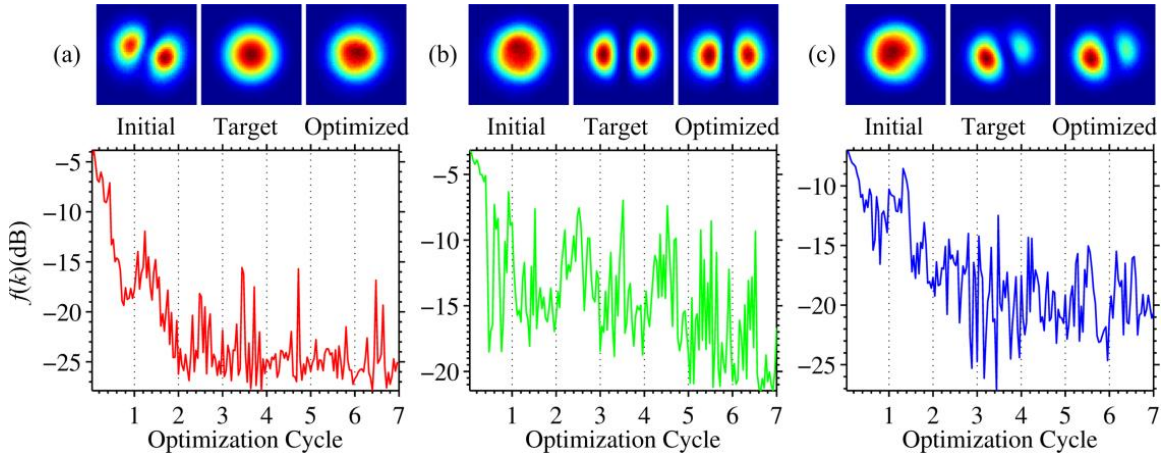

Fig. 3.2.7 Results of selective mode excitation using 5×5 blocks with different initial and target intensity profiles. The initial intensity distributions, the target intensity distributions, and the optimized images are labelled accordingly in (a)-(c). The optical output field is shape to (a) the LP_{01} mode; (b) the LP_{11} mode and (c) a mixture of the LP_{01}/LP_{11} modes (the target is an experimentally captured CCD camera image). The objective functions obtained during the optimization process are also shown in (a)-(c).

Finally, for certain applications in optical communications and sensing, it is often desirable to reduce the amount of independent SLM phase blocks used in selective mode excitation. (For example, fewer independent blocks should increase optimization speed and reduce system cost.) Here, we show that it is possible to use only the central 5×5 SLM blocks (out of the 13×13 phase blocks) to achieve highly selective mode excitation. Three different sets of "before" and "after" optimization images, as well as their corresponding target intensity distributions, are shown in Figs. 3.2.7(a)-3.2.7(c). For all three cases, the deviation between the target and the optimized image is less than 0.6 %. The variations of objective functions during 7 optimization cycles are also shown in Figs. 3.2.7(a)-3.2.7(c). Comparing the results shown in Fig. 3.2.7 (5×5 blocks) with the results obtained using 13×13 blocks in Figs. 3.2.5(a)-3.2.5(c), there is no significant degradation in the performance of SLM-based optimization.

We further reduce the independent SLM phase blocks from 5×5 to 3×3 central blocks (out of the 13×13 phase blocks). With fewer phase blocks, the performance of SLM optimization degrades noticeably. Figure 3.2.8 shows two representative examples, where the target mode is the LP_{01} and the LP_{11} mode, respectively. The difference between the target mode and the optimized intensity distribution is ~7.5% and ~6.0% respectively, and is noticeable through visual comparison.

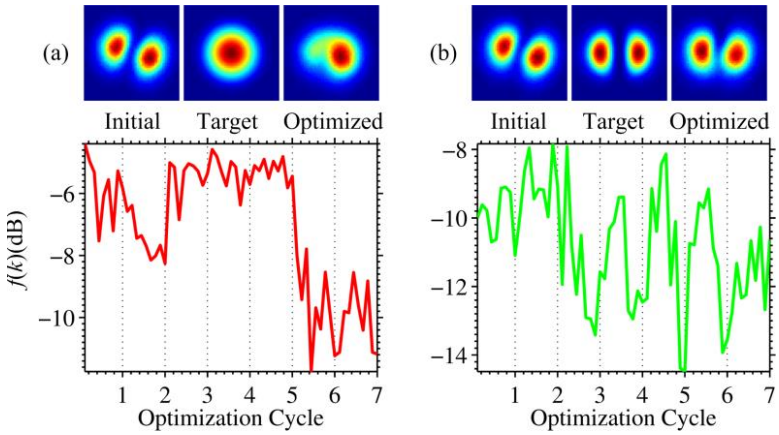

Fig. 3.2.8 Results of selective mode excitation using 3×3 blocks with different target intensity profiles. The initial intensity distributions, the target intensity distributions, and the optimized images are labelled accordingly in (a)-(b). The optical output field is shape to (a) the LP_{01} mode; (b) the LP_{11} mode. The objective functions obtained during the optimization process are also shown in (a) and (b).

3.3 Discussion and Conclusions

In present work, we do not consider the issue of coupling efficiency. Primarily, this is because for applications such as optical sensing, coupling efficiency is not as critical as in optical communications. Additionally, it should not be too difficult to incorporate coupling efficiency into the optimization process. For example, during the wavefront optimization procedure, we can take both the coupling ratio and the feedback signal into account. Given the fact that the algorithm described here has been widely used for optical focusing through diffusive media [23], where optical power is a critical factor, the issue of coupling efficiency should not become a major hurdle for our AO-based approach.

Additionally, we consider only a single polarization component for both the input and the output optical fields. While during the experiments, the orientation of P3 is randomly chosen, and we did not observe any dependence or correlation between the optimization results and P3 orientation. For more general scenarios, we may replace P2 in Fig. 3.1.1 with a polarization beam splitter (PBS) and P3 with another PBS. In this case, the study carried out here corresponds to a specific combination (out of four possible choices) for the input / output polarization channels. We can add more bulk optics components so that all four input / output polarization channels are monitored simultaneously using the same SLM and CCD camera.

Finally, the results presented here are obtained using a TMF. For a FMF that supports a limited number of modes (for example, 4 or 6), the results reported here should remain applicable. However, for a MMF that supports hundreds of modes, some of the conclusions may no longer apply. For example, we may need to use more phase control elements to distinguish different LP modes within the MMF. However, the overall framework of the AO-based approach should still apply. Again, this expectation is based on the successful demonstration of AO-based focusing, which involves hundreds, if not tens of thousands independent scattering channels.

In summary, we experimentally demonstrate the feasibility of using AO to achieve highly selective mode excitations in a TMF. In this proof-of-concept demonstration, we use the correlation between the CCD camera image and the theoretical target intensity profile as the feedback for AO-based mode control. The target profile can be purely LP_{01}, purely LP_{11}, or a mixture of the two modes. Furthermore, selective mode control can be accomplished using as few as 5×5 independent phase elements. While the mode control results degrade significantly if the number of independent phase control blocks decreases to 3×3. The method developed here can be easily generalized to cases where the feedback signal is provided by mode-selective elements, including MSCs and FBGs. The AO-based approach may find applications in MDM-based fiber optical communications, optical sensing and imaging.

Chapter 4

Adaptive Mode Control Using a Directional Coupler

In this chapter, we experimentally demonstrate that one can use AO and all fiber devices to control the guided modes within the TMF, as long as the fiber devices can generate appropriate feedback signals. The fiber device we are using for AO feedback is a TMF directional coupler. Instead of using image based method, the feedback signal is provided by either the coupling ratio, or the absolute optical power within the two output ports of the TMF directional coupler. The theoretical principle behind this experiment is that, for the two LP modes, the higher order LP_{11} mode extends much further into fiber cladding, which leads to a much larger coupling coefficient for the LP_{11}. Therefore, by maximizing or minimizing the coupling ratio, we should be able to adaptively control the LP modes in the TMF. Experiment results using only the absolute optical power of the output ports as feedback signals are also shown in this chapter.

4.1 Experiment Setup and AO Algorithm

The experiment setup is shown in Fig. 4.1.1, which is very similar to the previous setup shown in Fig. 3.1.1. The major difference is the addition of a directional coupler. Specifically, the TMF used in the previous experiments (Thorlabs 980HP, V = 3.57, length approximately 1.0m) is spliced to the input port of a directional fiber coupler (Thorlabs, FC980-50B). The directional coupler is fabricated using a similar TMF with a specified normalized frequency of V=3.71 at the operation wavelength. Therefore both the TMF and the directional coupler support the LP_{01} and the LP_{11} modes. At the output end of the fiber coupler, two additional pieces of TMF (Thorlabs 980HP, V = 3.57, length

approximately 1.0m) are spliced to the two output ports of the fiber coupler. These two coupler ports are respectively designated as the throughput port and crossover port, as indicated in Fig. 4.1.1. The end facets of the two output ports are carefully aligned to ensure that the cleaved fiber surfaces are located within the same object plane for imaging. The same objective lens (100×, NA=0.70) and CCD camera in Fig. 3.1.1 are used to capture the intensity profiles of both coupler ports simultaneously. The main purpose of the CCD camera is to analyze the mode composition at the two output ports of the coupler. The AO control is achieved through intensity measurements only, and does not require knowledge of optical field distributions.

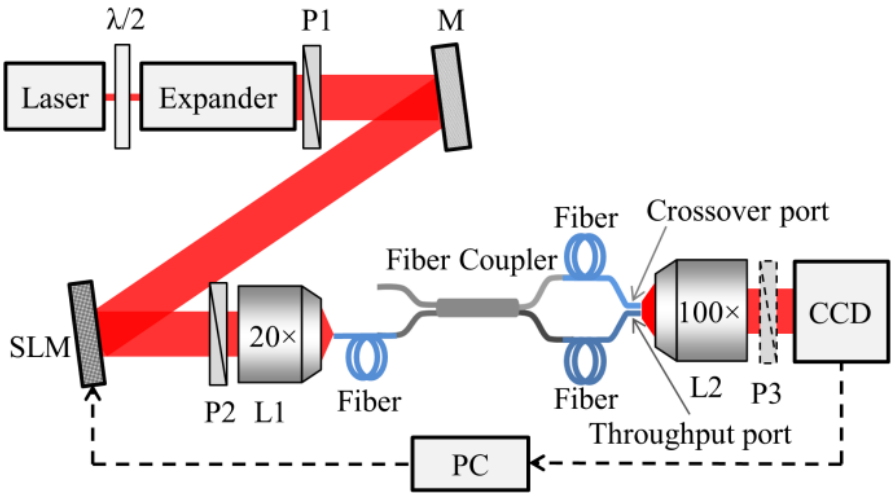

Fig. 4.1.1 Using a directional coupler to achieve mode control. Schematic of the setup: $\lambda/2$, half-wave plate; Expander, 1:5 beam expander comprise of two lenses; M, mirror; SLM, phase-only spatial light modulator; P1 and P2, polarizers; Polarizer P3 is optional, and is only added for experiments involving polarized output; L1, 20× objective lens, NA=0.40; Fiber, Thorlabs 980HP, ~1 m; Fiber Coupler, Thorlabs FC980-50B; L2, 100× objective lens, NA=0.70; CCD, CCD camera.

During experiments, the light polarization is controlled by a half-wave plate and two polarizers (P1 and P2), which select optical waves with polarization direction parallel to the optical table. The incident wave polarization also coincides with the phase modulation axis of the SLM. For studies involving linearly polarized output, an optional polarizer (P3) is added between the crossover / throughput port and the CCD camera.

AO-based mode control in this section basically follows the optimization algorithm described in Chapter 2.7, while the feedback signal, *i.e.* the objective function, for AO-based mode control is either the coupling ratio or the absolute power in the coupler's output ports. We use 11×11 phase blocks to control the wavefront of the incident beam for all experiments. Mode control is achieved by adjusting the SLM to minimize the objective function. In this process, each one of the 11×11 SLM blocks produces 11 different phase shifts between 0 to 2π for the reflected wave. The phase modulation procedure is the same as that mentioned in Chapter 3.1. During optimization, we change the phase shift of one, and only one phase block. As we cycle the phase shift of each block from 0 to 2π, the feedback signal changes accordingly. After obtaining the 11 objective functions produced by the 11 different phase shifts, we fix the phase shift of the current block to the one that minimizes the objective function. Then, we move to the next phase block and repeat this optimization procedure. This optimization process is sequentially carried out for seven optimization cycles in all the following experiments.

During the experiment, the optical power within the two output ports of the directional coupler is extracted from the CCD camera images, by summing the values of CCD pixels within the given coupler port, and the coupling ratio is defined as the percentage of optical power in the crossover port. In practice, it would be much easier to measure the optical power or the coupling ratio using two photodetectors. The main reason for using a CCD camera for power measurements is to ensure that we can obtain the spatial profiles of the guided waves for validation. Only the optical fields within two square windows (~5.6 μm ×5.6 μm in size, one for crossover port and one for throughput port) are used in power calculations and data analyses. This area corresponds to a 49×49 pixel block in the CCD images. The fiber core, with a radius of 1.8 μm, is completely contained within this region.

In the following discussion, we consider using either the absolute power or the coupling ratio as feedback signals. In the absolute power case, the objective function is simply the total optical intensity carried by the crossover port I_{cross} or the throughput port I_{through}. For cases with feedback based on coupling ratio (The coupling ratio always refers to the percentage of optical power within the crossover port), the objective function is defined as:

$$f(k) = \left| K - \frac{I_{\text{cross}}}{I_{\text{cross}} + I_{\text{through}}} \right| \tag{4.1.1}$$

where K is the target coupling ratio.

4.2 Experiment Results

First we discuss experimental studies where we use the coupling ratio as the feedback signal, without adding the polarizer P3. Using the algorithm described above, we adaptively set the coupling ratio of the directional coupler to seven different values. The target coupling ratio ranges from 0 to 0.27, with 0.27 being the highest coupling ratio that can be achieved in our experiments. For all seven cases, the initial field distributions and the final optimized intensity profiles for the crossover and the throughput ports are shown in Fig. 4.2.1. The initial coupling conditions are arbitrarily chosen, which typically leads to some small initial coupling into the crossover port. As a result, the initial field distribution in the crossover port tends to weak and contains substantial noises, as can be seen in Fig. 4.2.1.

In Fig. 4.2.1(a), the coupling ratio of the crossover port is optimized towards zero. After adaptive optimization, the field distribution within the throughput port is almost purely LP_{01}. This is to be expected, since within the coupler, the LP_{11} mode extends much further into the fiber cladding. As a result, the coupling ratio for the LP_{11} mode should be much higher than that of the LP_{01} mode. Hence the condition of zero crossover coupling should be equivalent to the requirement that the mode within the throughput port should be LP_{01} only. For all other cases, after optimization, the intensity profile of the crossover port is dominated by the LP_{11} mode. Again, this is consistent with the observation that only LP_{11} mode exhibit significant crossover coupling. For the throughput port, its intensity profile gradually changes from the LP_{01} mode to the LP_{11} mode, as we increase the target coupling ratio from 0 in Fig. 4.2.1(a) to 0.27 in Fig. 4.2.1(g).

Figure 4.2.2(a) shows variations of coupling ratios during seven optimization cycles for K = 0, 0.10, and 0.27, with individual cycles indicated by the dashed lines. Within each cycle, the coupling exhibits significant variations as we adjust the phase shift for each of the 11×11 SLM blocks. This is to be expected, since for any SLM block, a “wrong”

phase shift can certainly increase the difference between the actual and the target crossover coupling. The results in Fig. 4.2.2(a) suggest that it only takes 3-4 cycles to reach the target coupling ratios.

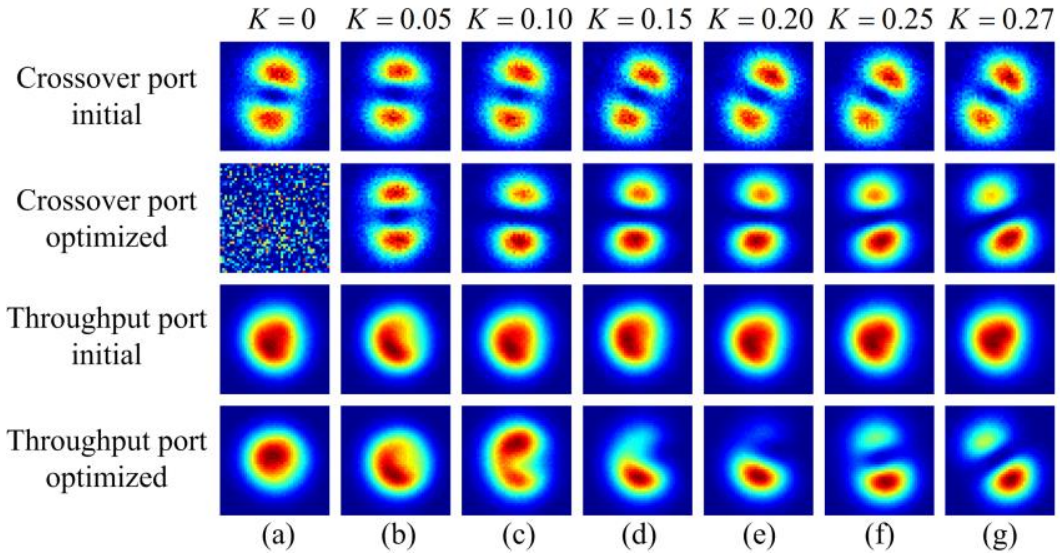

Fig. 4.2.1 Optimization results with different crossover coupling ratios *K*. The optimized images of both ports are labelled accordingly. All images are normalized to their maximum intensities.

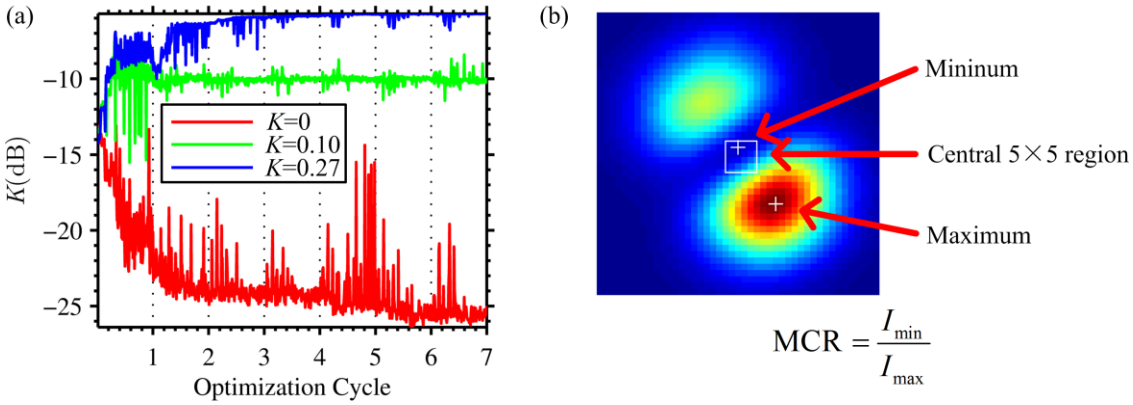

Fig. 4.2.2 (a) Variations of coupling ratios obtained during different optimization processes. (b) Definition of the ratio MCR.

In order to quantitatively analyze mode compositions of two coupler ports, we define a mode contrast ratio (MCR) as illustrated in Fig. 4.2.2(b). First, we define a small 5×5 pixel block that corresponds to the center of the fiber core. Then, we find the minimum

intensity I_{min} within the central block as well as the maximum intensity I_{max} in the entire intensity profile. The MCR is defined as:

$$\mathrm{MCR} = \frac{I_{\min}}{I_{\max}} \tag{4.2.1}$$

Notice that MCR is positive and always less than 1. The MCR is quantitatively related to the percentage of LP_{01} mode power. Since the LP_{11} mode must be zero at the fiber center, a small MCR that is close to 0 indicates that the majority of the optical power is carried by the LP_{11} mode. On the other hand, if MCR is close to 1, then guided wave should be dominated by the LP_{01} mode.

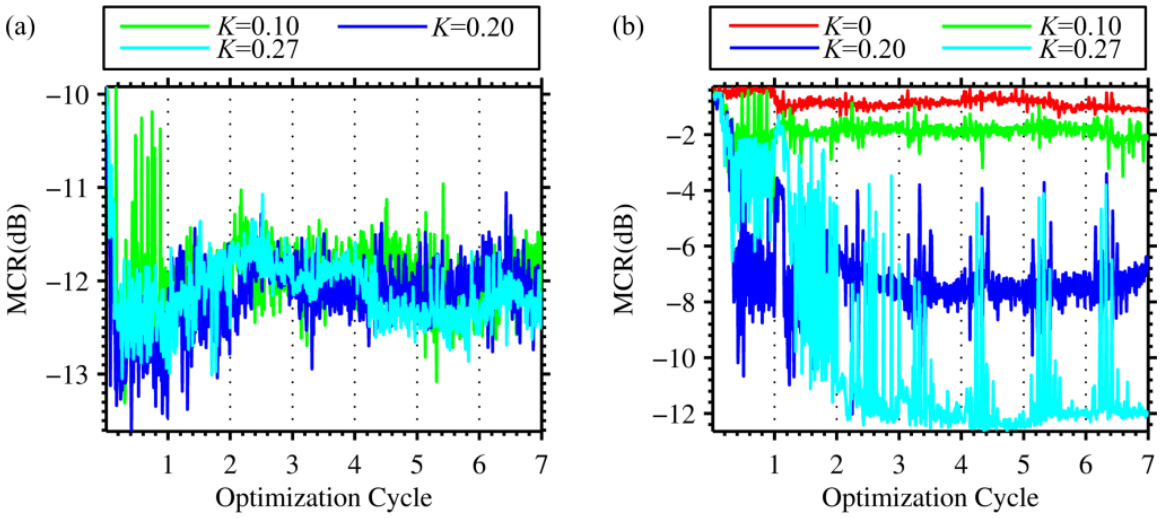

Fig. 4.2.3 Variations of the MCR obtained during different optimization processes for (a) the crossover port; (b) the throughput port.

We analyzed the MCR for both the crossover and the throughput ports for different target coupling ratios. The values of MCR during the entire optimization cycles are shown in Fig. 4.2.3 for several different target coupling ratios. From Fig. 4.2.3(a) we can see that for the crossover port, the fluctuation of MCR is relatively small for three representative cases, and the ratio value is close to 0.06. This quantitatively confirms that the optical field within the crossover port is dominated by the LP_{11} mode. For the throughput port, it is clear that the MCR decreases as the target coupling ratio increases. This suggests that as the target K increases, the mode composition of the throughput port is increasingly dominated by the LP_{11} mode. Again, this result is consistent with the images in Fig. 4.2.1.

To further illustrate the relation between *K* and MCR, we plot MCR versus *K* for both the crossover and throughput ports in Fig.4.2.4, where each dot represents the values of *K* and MCR obtained using a specific SLM phase setting. Different dot color represents data obtained under different target *K*, with red for *K* = 0, green for *K* = 0.05, blue for *K* = 0.10, cyan for *K* = 0.15, yellow for *K* = 0.20, magenta for *K* = 0.25, and black for *K* = 0.27. In Fig. 4.2.4 (a), we can see that excluding the obvious exception of *K* = 0, the MCR is always less than 0.1, regardless of *K* values. In Fig. 4.2.4(b), it is clear that the MCR of the throughput port decreases as the coupling ratio of the crossover port increases. Again, for the throughput port, the relationship between *K* and MCR clearly indicates that as we increase the target *K* values, we can gradually shift the composition of the throughput port mode from being dominated by the LP_{01} component to being dominated by the LP_{11} component.

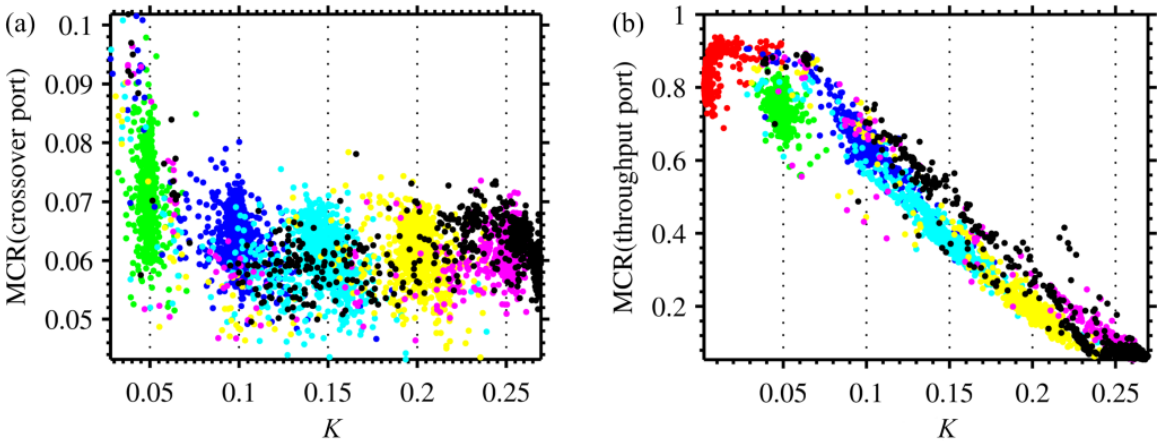

Fig. 4.2.4 MCR versus the coupling ratio of the crossover port: (a) MCR of the crossover port; (b) MCR of the throughput port.

It is worth pointing out that the intensity distributions in Fig. 4.2.1 suggest that the guided mode in the crossover port may contain a small percentage of the LP_{01} mode. The deviation is likely caused by intermodal coupling in the TMF. First, we note that the fused directional coupler contains taper transition regions, which may induce some coupling between the LP_{01} and the LP_{11} mode. Second, the TMF is not completely straight and contains circular bends. Third, the TMF and the directional coupler are not based on the same type of TMF. Therefore, any offset at the splice point may cause intermodal coupling. We want to point out that all the above experimental data are

obtained without using any polarizer in front of the objective lens L2 or the CCD camera. In fact, the images in Fig. 4.2.1 are in general the sum of optical intensities associated with two independent polarization channels. It is interesting to note that using coupling ratio as the feedback, we can adaptively control spatial profiles of transmitted modes without considering their polarizations.

In the second case, we incorporate polarizer P3 in our setup. Again, we use the coupling ratio as the feedback signal for adaptive control. During the experiment, the polarizer P3 selects a specific polarization for both the crossover port and crossover port, and the polarized coupling ratio is calculated based on the intensity profiles captured by the CCD camera. In the experiments, we find the highest possible coupling ratio for the crossover port is 0.70. Figures 4.2.5(a)-4.2.5(c) show results of adaptively setting the polarized coupling ratio to three different values. Again, the initial coupling conditions are arbitrarily chosen.

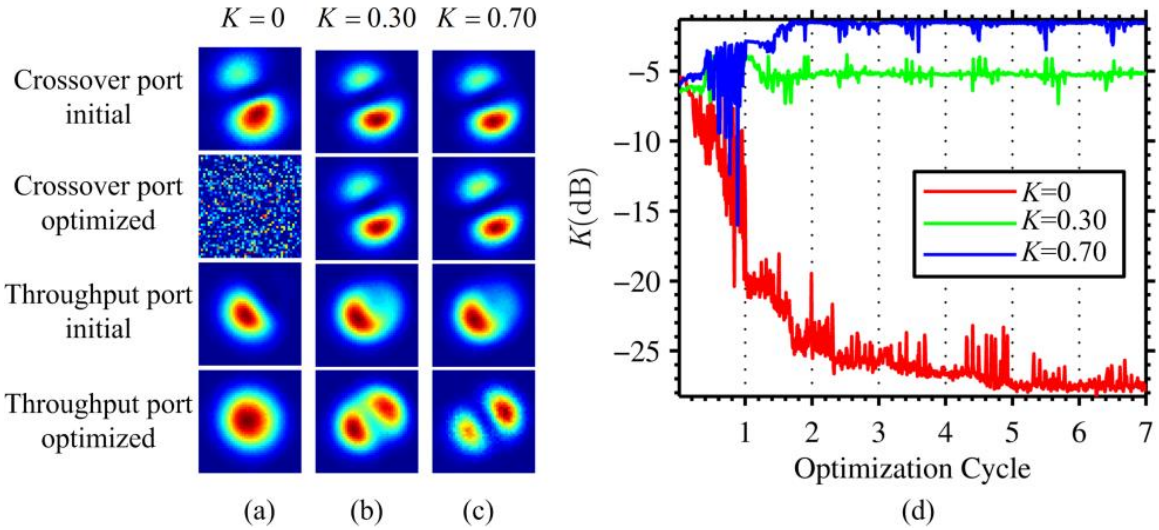

Fig. 4.2.5 Optimization results with different crossover coupling ratios, with polarizer P3 incorporated. The optimized images of both ports are labelled accordingly in (a)-(c). All images are normalized to their maximum intensities. (d) Variations of coupling ratios obtained during three different optimization processes.

Similar to Fig. 4.2.1(a), after optimizing the coupling ratio of the crossover port towards zero [Fig. 4.2.5(a)], the field distribution within the throughput port becomes almost

purely LP_{01}. For the other two cases, after optimization, the intensity profile of the crossover port is dominated by the LP_{11} mode. For the throughput port, its intensity profile gradually changes from the LP_{01} mode to the LP_{11} mode, as we increase the target coupling ratio from 0 in Fig. 4.2.5(a) to 0.70 in Fig. 4.2.5(c). Figure 4.2.5(d) shows the corresponding variations of coupling ratios during seven optimization cycles for K = 0, 0.30 and 0.70. For all cases, the target coupling ratio is reached after 3-4 cycles.

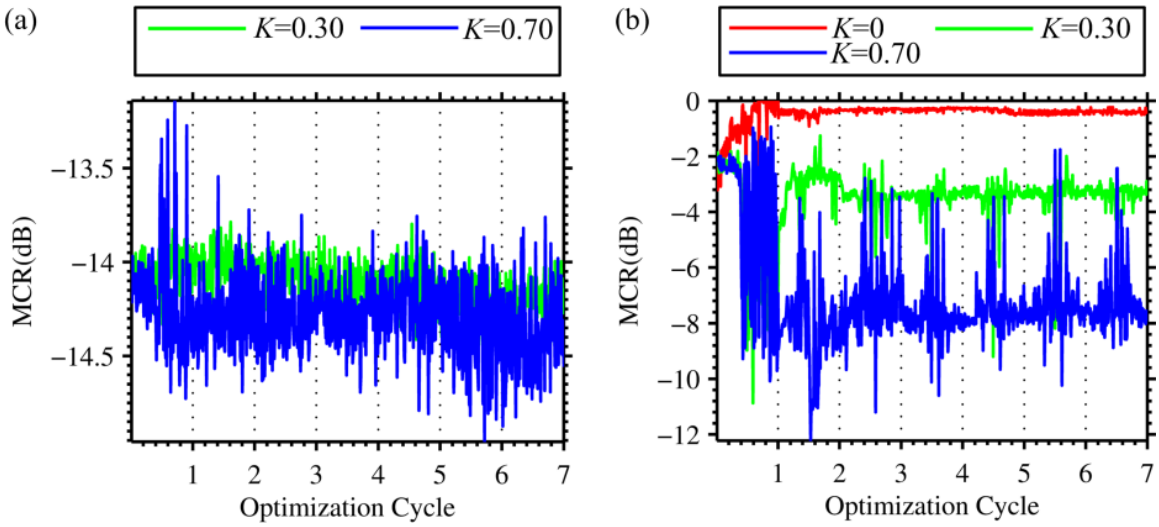

Fig. 4.2.6 Variations of the MCR obtained during optimization processes by using the polarizer P3 for (a) the crossover port; (b) the throughput port.

We analyzed the MCR for both the crossover and the throughput ports for different target coupling ratios shown in Figs. 4.2.5(a)-4.2.5(c) as well. The values of MCR during the entire optimization cycles are shown in Fig. 4.2.6 for different target coupling ratios. From Fig. 4.2.6(a), we can see that for the crossover port, the MCR is even smaller than the results shown in Fig. 4.2.3(a). For the throughput port results in Fig. 4.2.6(b), the MCR decreases as the target coupling ratio increases, which is consistent with non-polarized results shown in Fig. 4.2.3(b).

Given the similarity between the results in Figs. 4.2.5 and Figs. 4.2.6 and those in Figs. 4.2.1-4.2.3, our studies suggest that the coupler-based AO mode control can be extended to cases where wave polarization is important. One major difference is the maximum coupling ratio: in the polarized case, it is 0.7, whereas in the non-polarized case, it is only 0.27. This difference can potentially be explained by noting that optical field polarization

may change within the coupler as well as in the TMF. Furthermore, the changes of wave polarization in the throughput port and the crossover port may not be identical. Therefore, by adding the polarizer P3, which only allows the same linearly polarized light to pass through for both coupler ports, the maximum coupling ratio as captured by the CCD camera can vary significantly.

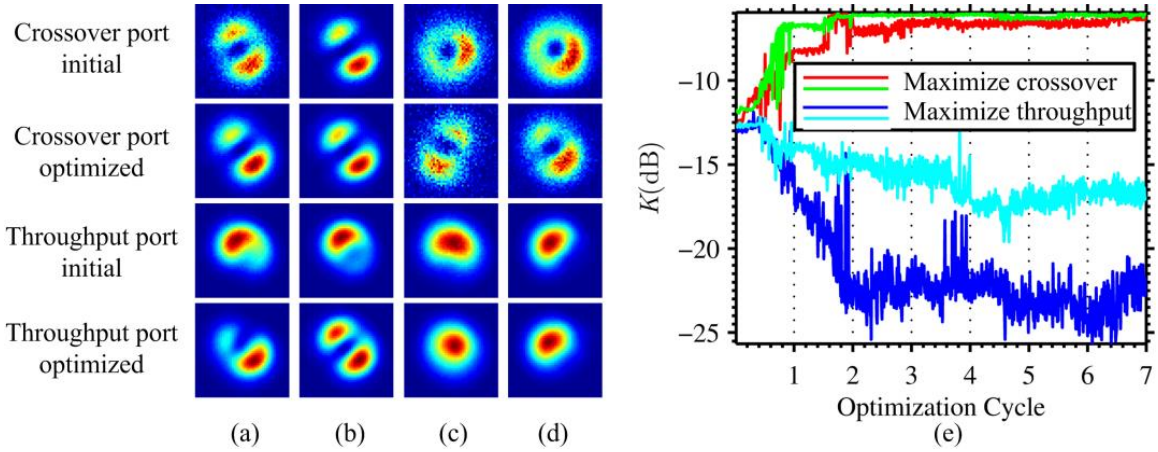

Fig. 4.2.7 Optimization results with feedback provided by the absolute intensity of the two output ports. Polarizer P3 is removed from the setup. (a)-(b) maximize the absolute intensity of the crossover port. (c)-(d) maximize the absolute intensity of the throughput port. The optimized images of both ports are labelled accordingly in (a)-(d). All images are normalized to their maximum intensities. (e) Variations of the coupling ratios obtained during different optimization processes.

In the third case, we consider the possibility of using the absolute power within either the crossover or the throughput port as the feedback signal for mode control. For these studies, the polarizer P3 is removed. The optimization procedure is similar to our previous studies, where we simply maximize the intensity of the crossover port or the throughput port. Figures 4.2.7(a)-4.2.7(b) show results of maximizing the intensity of the crossover port, and Figs. 4.2.7(c)-4.2.7(d) show results of maximizing the intensity of the throughput port. Again, the initial coupling conditions are arbitrarily chosen.

Form Figs. 4.2.7(a) and 4.2.7(b), we can see that after maximizing the intensity of the crossover port, both the crossover and throughput ports are dominated by the LP_{11} mode. From Fig. 4.2.7(e), we can see the result of maximizing the crossover port is very similar with the result of maximizing the coupling ratio of the crossover port. When maximizing

the throughput port power, though the throughput port field is not always close to the pure LP_{01} mode, it tends to be dominated by LP_{01} mode. For some cases [Figs. 4.2.7(c) and 4.2.7(d)], we can still identify some residual LP_{11} component in the crossover port after optimization. This conclusion can also be corroborated by the results in Fig.4.2.7(e), which shows that maximizing the absolute intensity of the throughput port does not necessarily guarantee that the coupling ratio of the crossover port converges to its lowest value. Specifically, we can see the coupling ratios shown in Fig. 4.2.7(e) for cases in Figs. 4.2.7 (c) and 4.2.7(d) are not as low as those shown in Fig. 4.2.2(a) or Fig. 4.2.5(d).

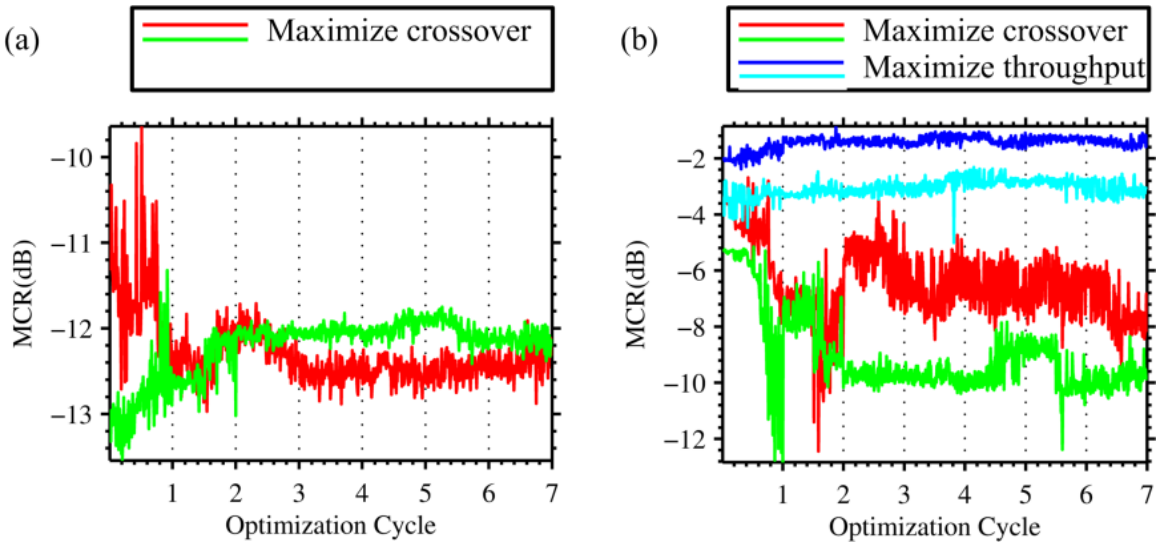

Fig. 4.2.8 Variations of the MCR obtained during different optimization processes. The absolute intensity of the crossover or the throughput port is maximized during the optimization process. Polarizer P3 is removed. (a) is the MCR of the crossover port. Results obtained by maximizing throughput port power are not shown, since for these cases, the crossover port carries low optical power and the corresponding field distribution is noisy. (b) shows the MCR of the throughput port.

The MCRs for results obtained using absolute power as AO feedback are also analyzed. The values of MCR during the entire optimization cycles are shown in Fig. 4.2.8 for four different cases in Figs. 4.2.7(a)-4.2.7(d). Again, from Fig. 4.2.8(a), it is clear the crossover port is dominated by the LP_{11} mode when we maximizing the intensity of the crossover port, and the MCR values are as small as the results shown in Fig. 4.2.3(a).

Maximizing throughput port power, however, sometimes yield less than ideal results. For example, from Fig. 4.2.8(b), we can see that in some cases (e.g., the cyan line), the MCR can sometimes be substantially less than 1. It indicates that even after optimization, the throughput port may contain a substantial percentage of the LP_{11} component.

4.3 Discussion and Conclusions

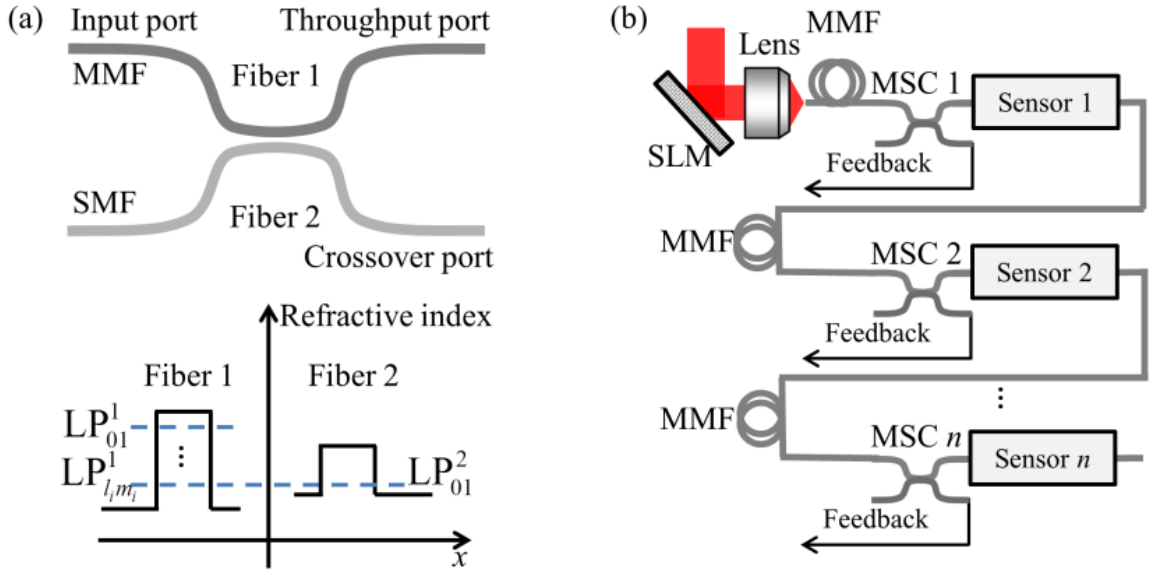

Fig. 4.3.1 (a) Schematic of a 2×2 MSC that contains a MMF arm and a SMF arm. Its refractive index profile is shown in the bottom panel. Dashed lines in the refractive index profiles in (a) indicate the effective indices of various LP modes in fiber 1 and 2. (b) Schematic of a quasi-distributed sensor network that utilizes MSCs to provide feedback signals.

The directional coupler based mode control method can also be generalized to other types of MSCs [35-37]. Fig. 4.3.1 (a) illustrates a MSC where fiber 1 (i.e., the input and the throughput ports) is a MMF that supports N LP modes ($N \geq 2$), and fiber 2 (i.e., the crossover port) is a SMF. Through proper fiber design or by applying techniques such as fiber pre-pulling, we can ensure that the effective index of the LP_{01} mode in fiber 2 to be very close to the effective index of the ith LP mode in fiber 1, *i.e.*, $LP^1_{l_i m_i}$, as illustrated in the bottom panel of Fig. 4.3.1(a). Since different LP modes possess different effective indices, it should be possible to ensure that only the ith LP mode in the MMF is coupled

into the SMF. Such a MSC can be demonstrated using existing methods. For mode monitoring in a sensor network, we can use the MSCs depicted in Fig. 4.3.1(a) and choose small coupling ratios (e.g., 1%). In this case, the MSCs essentially serve as mode selective tap couplers. Fig. 4.3.1(b) shows the schematic of a quasi-distributed MMF sensor network with *n* fiber sensors, where each sensor is monitored by a MSC. Under this design, if we fix the total power of the incident signal, by maximizing or minimizing the optical power carried by the crossover port of a specific tap coupler, we should be able to select the form of the LP mode that enters into the corresponding fiber sensor. Our results in Fig. 4.2.4(b) suggest that it may also be possible to adaptively control the interrogation signal entering into any given fiber sensor to be a specific mixture of different LP modes. A detailed design of such a sensor network, however, is beyond the scope of this research.

In conclusion, we demonstrate that it is possible to use the coupling ratio of a directional coupler as feedback signal for adaptive mode control. Specifically, by minimizing the coupling ratio of the crossover port, we can ensure that the optical field within the throughput port is dominated by the LP_{01} component. Conversely, by maximizing the coupling ratio, we can ensure that the optical fields in both the crossover and the throughput ports are dominated by the LP_{11} component. We find that this conclusion holds for both polarized cases as well as non-polarized cases. Finally, we demonstrate that under certain circumstances, it is possible to use absolute power as the feedback signal for mode control. For example, by maximizing optical power carried by the crossover port, we can ensure that the optical field in the crossover and the throughput port are dominated by the LP_{11} components. However, if we use the throughput power as the feedback signal, the mode control performance is not as good at that of using the coupling ratios as feedback signals. The work can serve as a proof-of-concept demonstration that by incorporating multiple feedback elements within a MMF network, it is possible to adaptively control the guided modes *within* the MMF network in a quasi-distributed manner.

Chapter 5

Adaptive Mode Control Based on Fiber Bragg Gratings

In this section, we experimentally demonstrate that one can use AO and an FBG in TMF to control the guided modes *within* a TMF. For many applications, the FBG-based adaptive mode control is superior to the coupler-based approach in Chapter 4. Fiber gratings have been used in MDM for mode conversion [6]. Components such as SLMs have also been used to characterize few-mode fiber based FBGs [21]. However, to the best of our knowledge, this experiment presents the first demonstration showing that one can use AO and FBGs to control the guided modes *within* TMFs. In particular, by inscribing multiple ultra-weak FBGs within a TMF network and applying the TDM technique developed in [43], we can use the method developed here for quasi-distributed mode control *within* the TMF network, regardless of the mechanism and strength of mode coupling. In the future, the work presented here can be used to separately interrogate the responses of TMF-based sensors under different incident modes.

5.1 Experiment Setup and AO Algorithm

The experiment setup is shown in Fig. 5.1.1. A distributed feedback (DFB) laser (QPhotonics, QDFBLD-1550-20) is thermally tuned to operate at 1529.70 nm. The laser is coupled into free space using a collimator (L1). The free space beam is reflected and modulated by a DM with 140 blocks (Boston Micromachines) and focused into a ~2 meter long TMF by an objective lens (L2, 20×). The TMF is purchased from OFS and possesses a step-index profile that supports the LP_{01} and the LP_{11} modes at the operation

wavelength. A standard FBG (commercially written in the TMF by Ascentta Inc.) is spliced to the output port of the TMF. The FBG reflection spectrum is measured using a component test system (CTS, Micron Optics, HR-SLI) and a circulator, as shown in Fig. 5.1.2(a). A typical measured result, as shown in Fig. 5.1.2(b), contains a dominant peak at ~1529.70 nm and a much weaker one at ~1528.35 nm. According to theoretical results of FBGs (in Section 2.3) based on the coupled-mode theory, the peak reflection wavelength of the FBG is expressed as $2n_{\text{eff}}\Lambda$ in Eq. (2.3.8). For a TMF, the effective refractive index of the LP_{11} mode is lower than the LP_{01} mode, thus we attribute the stronger reflection peak at the longer wavelength to the LP_{01} mode and the much weaker peak at the shorter wavelength to the LP_{11} mode. This result agrees with experimental observations in [22]. The apparent difference in the measured reflection magnitude can perhaps be explained as an artifact of the measurement system, since both the CTS and the circulator use standard SMF as the input / output ports, and the TMF is directly spliced to the SMF. In this case, the incident light as "seen" by the FBG in the TMF is dominated by the LP_{01} mode, hence the apparently much higher reflection.

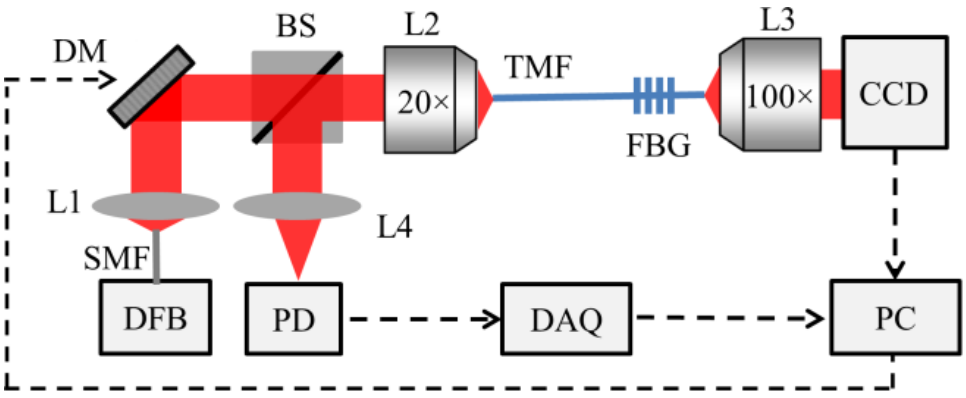

Fig. 5.1.1 Experimental setup of AO-based mode control: DFB, distributed feedback laser; L1, collimator; DM, deformable mirror; BS, beam splitter; L2, 20× objective lens, NA=0.40; TMF, OFS two mode fiber; FBG, fiber Bragg grating; L3, 100× objective lens, NA=0.70; CCD, infrared CCD camera; L4, lens; PD, photodetector; DAQ, data acquisition device.

At the output of the TMF, we use an objective lens (L3, 100×) and an infrared CCD camera (Hamamatsu, C10633-13) to capture the output intensity profile. A beam splitter (BS) is placed before L2 to collect the FBG reflection signal. The strength of the

reflection signal is measured using a photodetector (PD) and a data acquisition (DAQ) device. The PD and the CCD together provide the feedback signal for mode control.

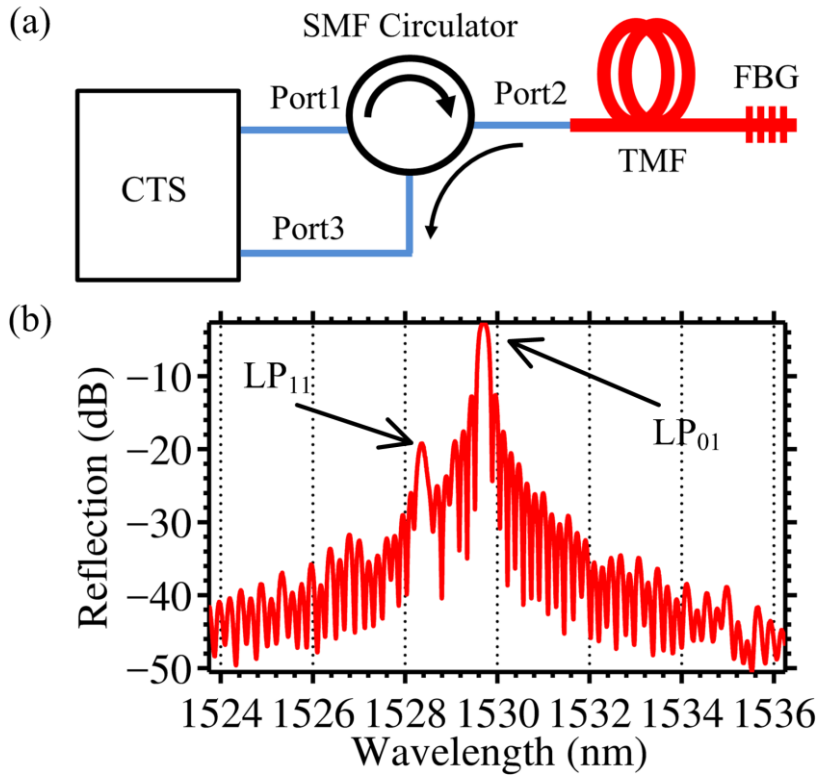

Fig. 5.1.2 (a) FBG reflection spectrum measurement; The FBG is written in a TMF (thick red line). All other components are connected using SMF (thin blue line). (b) A representative FBG reflection spectrum.

Similar to previous sections, the algorithm for adaptive mode control is based on the optimization algorithm described in Section 2.7, and here we define an objective function F for AO feedback:

$$F = \frac{I_{\mathrm{CCD}}}{V_{\mathrm{PD}} - V_{\mathrm{BG}}} \propto \frac{P_T}{P_R - P_{\mathrm{BG}}} \tag{5.1.1}$$

where P_R is the total reflected power detected by the PD, P_T is the transmitted power, and P_{BG} is the background reflection due to all optical components other than the FBG. In our experiments, P_T is represented by I_{CCD}, which is extracted from the CCD images by averaging the optical intensity of an 80×80 pixel block (a ~20.0 μm × 20.0 μm region) that contains optical signals guided in the fiber core. In practice, it would be much easier

to measure P_T using a PD. However, by using the CCD camera as a detector, we can easily capture the spatial distribution of the output field for mode control validation. Similarly, the total reflected power and the background reflection are replaced by the corresponding PD voltage, i.e., V_{PD} and V_{BG}. Based on Eq. (5.1.1), it is clear that our feedback signal F is proportional to the ratio of optical transmission and reflection of the inline FBG. To determine V_{BG}, we fix the DFB laser power at 3.0 mW and tune the laser wavelength far away from the reflection wavelength of both the LP_{01} and the LP_{11} mode. Under this condition, the average PD signal generated by background reflection is approximately 10 mV. During experiments, we set V_{BG} = 9.4 mV, a value slightly less than the measured mean background. With this choice, we eliminate most of the background reflection from the feedback signal, while at the same time, ensure $V_{PD} - V_{BG} \neq 0$.

We can use Eq. (5.1.1) to explain the principle of FBG-based mode control. First, we tune the laser wavelength to 1529.70 nm, which is the reflection peak of the LP_{01} mode. If the incident wave is purely LP_{01}, it experiences maximum reflection and minimum transmission, which means a relatively small value for F. On the other hand, if the incident signal is purely LP_{11}, the FBG reflection is minimal. Correspondingly, the feedback function F can become very large. Therefore, maximizing the feedback function F in Eq. (5.1.1) should lead to a pure LP_{11} mode. Experimentally, this is achieved by adjusting the DM, where each of the 140 DM blocks produces 18 different phase shift values between 0 to ~2π upon reflection. During the optimization, we sequentially cycle the phase shift of one and only one DM block through the 18 different values. We record the feedback function F at each phase shift value. For any given DM block, at the end of each phase shift cycle, we select its phase shift value to be the one that maximizes F, and move on to the next DM block. A single iteration, sequentially carried out for all 140 blocks, is referred to as one optimization cycle.

5.2 Experiment Results

Using the algorithm described above, we can adaptively control the modal composition of the optical field at the FBG location. We first show experimental results of selective

excitation of the LP_{11} mode. Figure 5.2.1 gives the initial and the intermediate field distributions at the end of each optimization cycle (1-7) of four representative experiments (labelled Ex1 to Ex4). The initial distributions are intentionally chosen to be significantly different from the desired LP_{11} mode profiles. From Fig. 5.2.1 we can see that, after seven cycles of optimization, the final intensity profiles are the superposition of two degenerate LP_{11} modes, since the pixel intensities at the center are very close to zero. The fringe patterns in Fig. 5.2.1 are likely caused by a thin film within the CCD camera, which is placed there to protect the CCD chip.

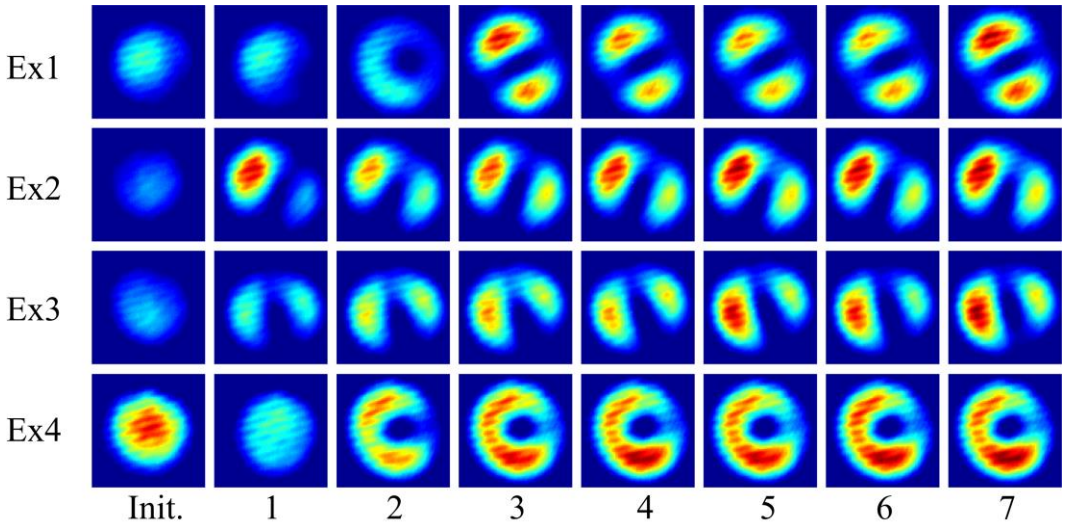

Fig. 5.2.1 Initial (labeled as "Init.") and the intermediate intensity profiles at the TMF output for four representative experiments (Ex1 to Ex4) that show selective excitation of the LP_{11} mode. Each optimization cycle (1-7) is labelled accordingly.

In Figs. 5.2.2(a)-5.2.2(c), we show the values of I_{CCD}, $V_{PD} - V_{BG}$, and the feedback function F obtained during the entire optimization process (i.e., all seven cycles) of Ex1 to Ex4. Within each optimization cycle, all three values exhibit significant variations. This is to be expected, since during any optimization cycle, all DM blocks produce phase shift from 0 to 2π, which inevitably leads to numerous "wrong" wavefronts for the desired outcome. However, some general trends are clear. From Fig. 5.2.2(a) we observe that I_{CCD} generally increases after completing all seven optimization cycles, whereas the PD signal (associated with FBG reflection) tends to decrease consistently throughout the entire optimization process. Additionally, from the feedback function F shown in Fig.

5.2.2(c), we can see that generally after 3-4 cycles of optimization, the value of the feedback function become reasonably close to its final outcome. It suggests that less than four cycles of optimization is sufficient for the output field to become almost purely LP_{11}. This observation can be confirmed from Fig. 5.2.1, in which the TMF output at the end of each optimization cycle is shown for Ex1-Ex4.

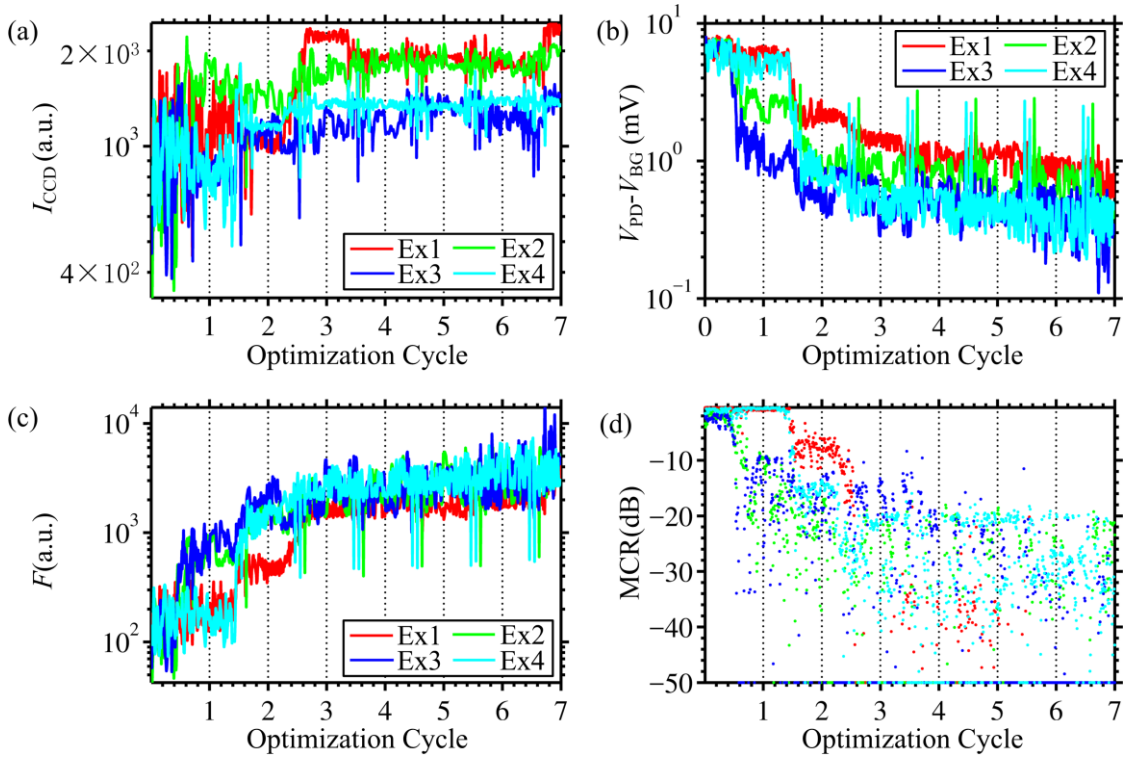

Fig. 5.2.2 Experimental results show selective excitation of the LP_{11} mode. Variations of (a) the average CCD intensity; (b) the PD signal with V_{BG} subtracted; (c) the value of the feedback function F; and (d) MCR during obtained during seven optimization cycles for the four representative experiments (Ex1-Ex4); Since MCR may become very small and occasionally reach 0 during optimization, all data points with MCR ≤ -50dB are replaced by MCR = −50dB for easier visualization.

To quantitatively analyze the composition of the LP modes during optimization, we utilize the MCR defined in Chapter 4.2 and Eq (4.2.1). One minor difference is that I_{min} is now defined in a small 7×7 pixel block at the center of the fiber core. For Ex1 to Ex4, variations of MCR during optimization are given in Fig. 5.2.2(d). From Fig. 5.2.2 (d) we

can see that after 3-4 optimization cycles, the MCR for all four representative experiments falls below −20dB. For the next few optimization cycles, MCR tends to fluctuate at a level less than −20dB, which indicates that optical fields at the TMF output are nearly pure LP_{11}. This result agrees well with our observation in Fig. 5.2.2(c).

The above AO algorithm can also be used to selectively excite the LP_{01} mode at the FBG location. Since our DFB laser cannot be tuned to 1528 nm, we replace the DFB laser in Fig. 5.1.1 with a tunable laser (New Focus, 6328). Except for the change of laser source, our experimental procedure remains the same. As mentioned previously, for selective excitation of the LP_{01} mode, the tunable laser is set at the reflection peak associated with the LP_{11} mode, i.e., at ~1528.35 nm.

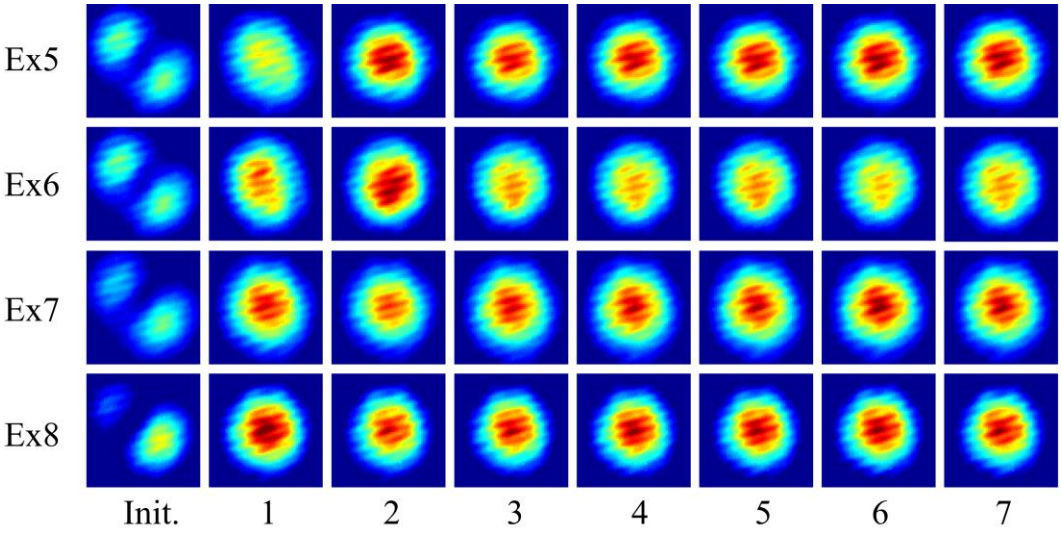

Fig. 5.2.3 Initial and the intermediate intensity profiles at the TMF output for four representative experiments (Ex5 to Ex8) of selective excitation of LP_{01} mode. Each optimization cycle (1-7) is labelled accordingly.

Using the same algorithm, we adaptively control the optical field at the FBG to be the pure LP_{01} mode. Figure 5.2.3 shows the initial and the optimized field distributions at the end of each of the seven cycles of four representative experiments (labelled Ex5 to Ex8). Again, the initial distributions are intentionally chosen to be significantly different from the desired LP_{01} mode profiles. Figure 5.2.3 shows that after optimization, the final intensity profiles are very similar to that of the LP_{01} mode. During experiments, the

background value V_{BG} is similarly measured as previous, and is set at 7.2 mV for Ex5, 6.9 mV for Ex6, 7.35 mV for Ex7, and 7.25 mV for Ex8.

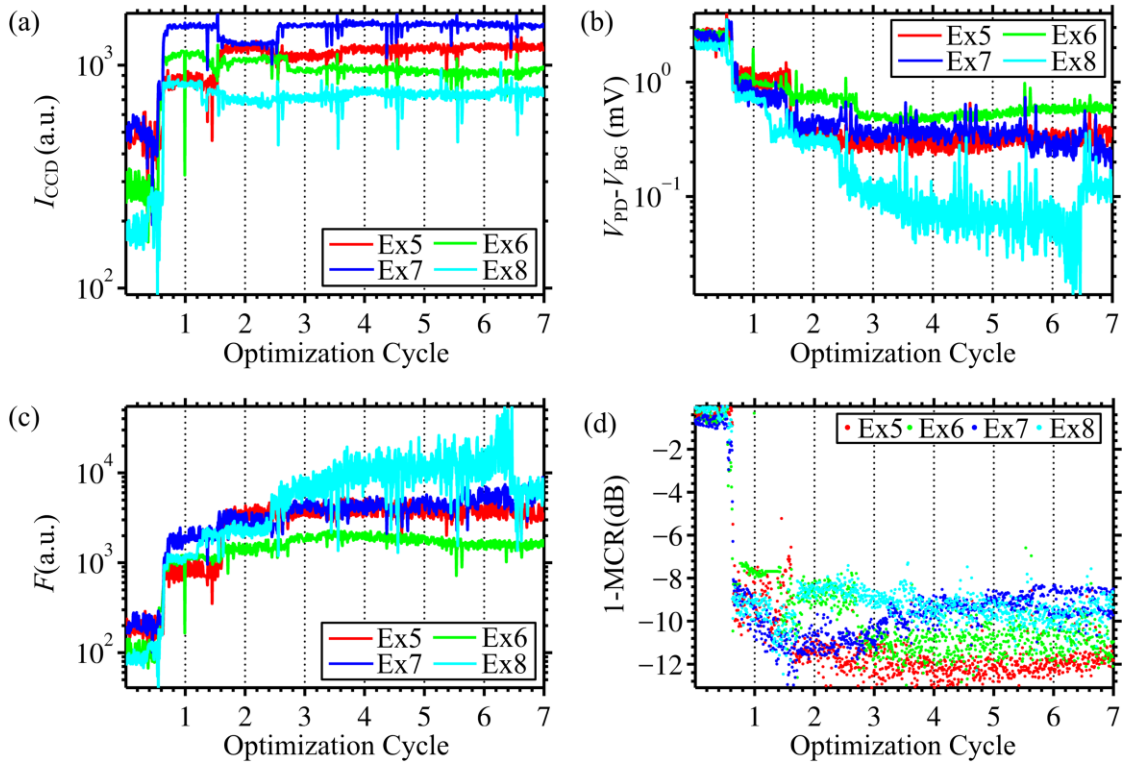

Fig. 5.2.4 Experimental results show selective excitation of the LP_{01} mode. Variations of (a) the average CCD intensity; (b) the PD signal with V_{BG} subtracted; (c) the value of the feedback function F; and (d) 1−MCR obtained during seven optimization cycles of four representative experiments (Ex5 to Ex8).

Figures 5.2.4(a)-5.2.4(c) shows the values of I_{CCD}, $V_{PD} - V_{BG}$, and the feedback function F obtained during the seven optimization cycles of Ex5 to Ex8. Similar to Fig. 5.2.2, from Fig. 5.2.4(a) we observe that I_{CCD} generally increases after seven optimization cycles, and the PD signal tends to decrease. Fig. 5.2.4(c) shows after three optimization cycles, the value of the feedback function F is reasonably close to the final outcome, which suggests three optimization cycles might be sufficient for the output field to become almost purely LP_{01}. In this aspect, the experimental result is consistent with that of Fig. 5.2.2(c). The CCD images in Fig. 5.2.3 also confirm this observation.

To quantitatively describe the variations of LP mode composition, Figure 5.2.4(d) provides the values of 1−MCR during the optimization. As we can see from Fig. 5.2.4(d),

after three cycles of optimization, the value of 1−MCR decreases to around −10 dB, starting from the initial value that is close to 0 dB. This result again suggests that it may only takes three cycles of optimization to accomplish selective excitation of the LP_{01} mode. The artificial fringes produced by the CCD camera itself may explain why the minimal values of 1−MCR "saturates" at only around −10dB.

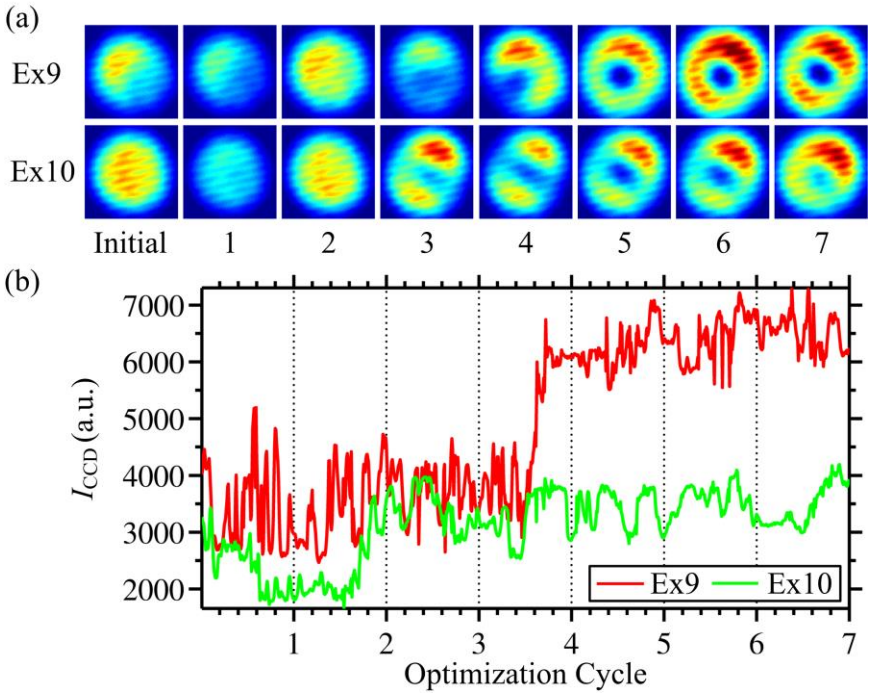

Fig. 5.2.5 Adaptive mode control for the LP_{11} mode using only I_{CCD} as feedback. (a) Initial and the intermediate intensity profiles at the TMF output for two different experiments (Ex9 and Ex10). Each optimization cycle (1-7) is labeled accordingly; (b) Variations of the average CCD intensity obtained during seven optimization cycles.

In addition to the method based on the ratio of FBG reflection and transmission, we also explore an alternative approach, where the feedback for wavefront modulation is based on the total transmitted power only. More specifically, the optimization procedure is almost exactly the same as above, except that the feedback signal is I_{CCD} only. During the experiments, we operate the tunable laser at 1529.70 nm, which is the wavelength associated with the LP_{01} reflection peak, and maximize I_{CCD}.

The experiment results are shown in Fig. 5.2.5. Figure 5.2.5(a) shows the initial and intermediate field distributions at the end of each optimization cycle (1-7) of two different experiments, labelled as Ex9 and Ex10, respectively. Again, the initial field is intentionally chosen to be significantly different from the final target, which is the LP_{11} mode. Figure 5.2.5(b) plots the value of the feedback signal I_{CCD} obtained during the optimization. As we can see from Fig. 5.2.5(a), in Ex9, the final optimized field is reasonably close that of the LP_{11} mode. On the other hand, in Ex10, the final optimized field seems to be a superposition of the LP_{01} and the LP_{11} modes.

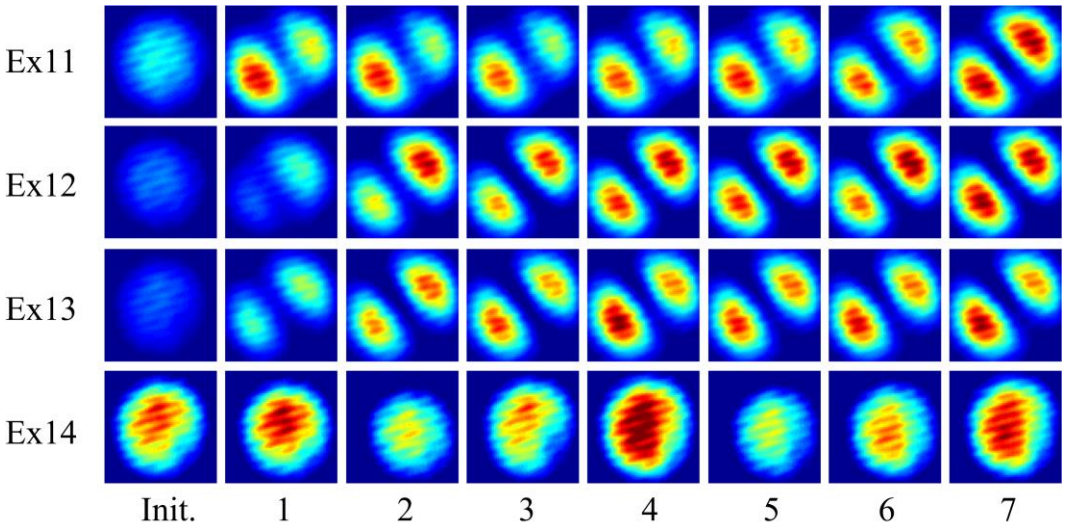

Fig. 5.2.6 Initial and the intermediate intensity profiles at the TMF output for 4 representative experiments (Ex11 to Ex14) of selective excitation of LP_{01} mode with V_{BG}=7.4mV, 5.4mV, 3.4mV, and 1.4mV respectively. Each optimization cycle (1-7) is labelled accordingly.

Figure 5.2.5(b) gives the variations of the feedback function (i.e., I_{CCD}) recorded during the optimization processes. We observe that after optimization, the final transmitted power in Ex9 is much higher than that of Ex10. The difference in transmitted power can be explained by the following observations. First, we note that the final output field for Ex10 contains significant LP_{01} component, whereas that of Ex9 is almost purely LP_{11}. Therefore, at the operation wavelength (1529.70 nm), which is the reflection peak associated with the LP_{01} mode, the optical field with significant LP_{01} component (i.e., Ex10) should experience higher reflection and therefore lower transmission. However,

the total transmitted power is a product of the incident power and the fiber transmission, and therefore depends on both factors. Therefore, in some cases (such as Ex10), maximizing I_{CCD} does not always lead to a pure LP_{11} mode.

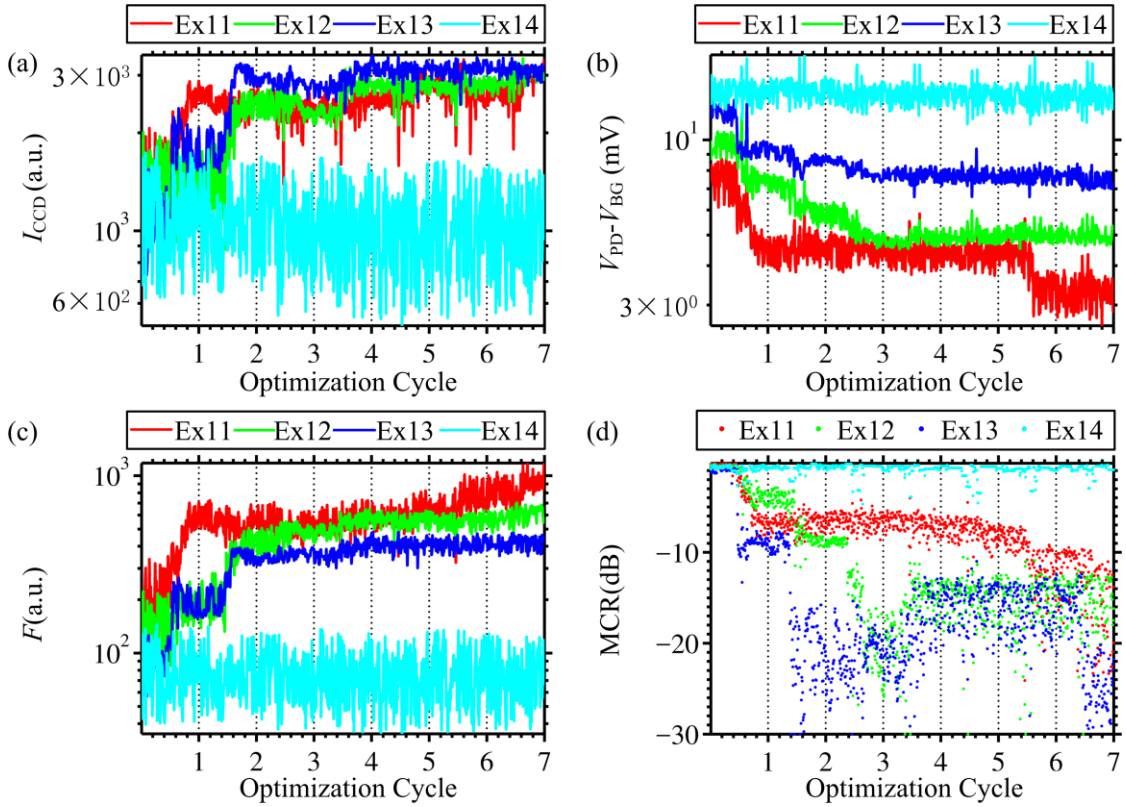

Fig. 5.2.7 Experimental results show selective excitation of the LP_{11} mode with different V_{BG}. Variations of (a) the average CCD intensity; (b) the PD signal with V_{BG} subtracted; (c) the value of the feedback function F; and (d) MCR obtained during 7 optimization cycles for the four representative experiments (Ex11-Ex14). All data points with MCR ≤ −30dB are replaced by MCR = −30dB for easier visualization.

To demonstrate the effect of V_{BG} during experiments, we have carried out adaptive mode control for pure LP_{11} mode with different values of V_{BG}. The results are shown in Fig. 5.2.6, which shows the initial and the final optimized field distributions of four experiments (labelled Ex11 to Ex14) with four different V_{BG} values (7.4 mV for Ex11, 5.4 mV for Ex12, 3.4 mV for Ex13, and 1.4 mV for Ex14). The initial conditions for all four experiments are the same except different V_{BG}. From Fig. 5.2.6, we can see the optimized

mode intensity profiles for Ex11-Ex13 are still the superposition of two degenerate LP_{11} modes, since the pixel intensities at the center are very close to zero. While for Ex14 (V_{BG}=1.4mV), the optimized mode intensity profile does not exhibit significant difference from the initial field distribution, and it is definitely dominated by the LP_{01} mode.

Variations of I_{CCD}, $V_{PD} - V_{BG}$, and the feedback function F obtained during the entire optimization process of Ex11-Ex14 are shown in Figs. 5.2.7(a)-5.2.7(c). Figures 5.2.7(a)-5.2.7(c) verify the results shown in Fig. 5.2.6. As we can see, for Ex11-Ex13, I_{CCD} generally increases after the optimization, and the I_{CCD} values after optimization are pretty close; $V_{PD} - V_{BG}$ generally decreases after the optimization, and the differences between their optimized $V_{PD} - V_{BG}$ values agree well with the differences of their V_{BG} values; and their feedback signal F increases after optimization. While for Ex14, its values of I_{CCD}, $V_{PD} - V_{BG}$ and F fluctuate during the optimization, but do not present great improvement after the optimization. Figure 5.2.7(d) plots the MCR obtained during the four experiments corresponding to Ex11-Ex14 in Fig. 5.2.6. From Fig. 5.2.7(d) we can see the MCR of Ex11-Ex13 fall under -10dB in the last optimization cycle. It is interesting to see we can still adaptively optimize the mode close to pure LP_{11} even will lower V_{BG} values. While Ex14 indicates that, if V_{BG} is significantly lower (e.g. 1.4 mV) than the background reflection, we cannot guarantee the optimized mode to be pure LP_{11} mode anymore.

5.3 Discussion and Conclusions

Our current experimental studies suggest that the ultimate accuracy of FBG-based mode selection is perhaps limited by the background reflection. It should be possible to significantly suppress the impact of background reflection by combing this method with TDM, in which pulsed signals are used for mode control. In this approach, we can identify the source of reflection based on the arrival time of the reflected pulse. Therefore, it should be possible to completely eliminate any background reflection due to the objective lenses or cleaved fiber facets. Under this scenario, the ultimate limiting factors are likely fiber Rayleigh scattering and / or detector noises. If we inscribe multiple ultra-weak FBGs within a TMF network, and combine this method with the TDM technique,

we should be able to optimize the mode at individual FGB location, thus it is possible to accomplish quasi-distributed mode control *within* the TMF network.

In conclusion, by using the ratio between FBG transmission and reflection as feedback, we can adaptively control the form of optical signals at the FBG location. Experimentally, we have demonstrated that by maximizing the feedback signal at the FBG peak reflection wavelength associated with the LP_{01} / LP_{11} mode, we can selectively excite almost purely LP_{11} / LP_{01} modes. This work can also serve as a proof-of-concept demonstration for dynamical control of optical waves within a TMF-based fiber optic network. By combining the method developed here and the TDM technique, it should be possible to adaptively control the composition of interrogation signals within a TMF network in a quasi-distributed manner. Though the experiments shown in this paper is based on TMF, generalization to MMF-based optical networks should be possible.

Chapter 6

Adaptive Mode Control in Time Domain

In previous chapters, we have demonstrated the AO-based approach can accurately control the form of optical waves in a TMF. Our method relies on the optimization algorithm in [24], where we utilize feedback signals provided by the optical field distribution, the coupling ratio of a directional coupler, and the strength of optical reflection by a FBG. In this chapter, we combine the FBG-based mode control method developed in Chapter 5 and the TDM technique developed in [43]. By using this new method, we can accomplish selective mode excitation at different FBG locations *within* the TMF, respectively.

Two different sets of experiments are described in this Chapter. In the first case, the feedback signal for AO-based mode control is similar to Chapter 5, *i.e.* the ratio of the optical power reflected by specific FBG in the TMF and the transmitted power, but the signals are measured in time-domain. Experiment results of AO-based mode control confirm selective mode excitation at two different FBG locations. In the second case, AO-based mode control is accomplished by using only the reflection signals as feedback. Specifically, the experiment is implemented by using two lasers set to two FBG peak reflection wavelengths associated with the LP_{01} or LP_{11} modes respectively. The feedback signal is the ratio of the optical power of two lasers reflected by specific FBG within the TMF.

6.1 Mode Control Based on Transmission and Reflection Signals

6.1.1 Experiment Setup and AO Algorithm

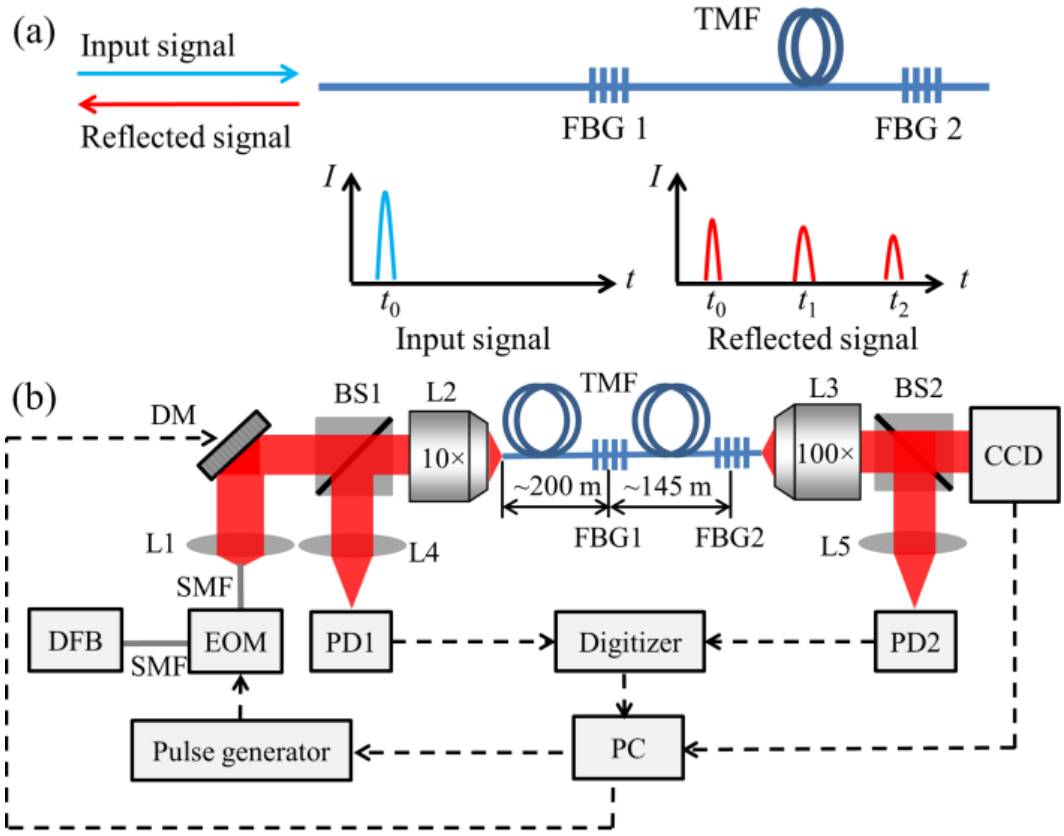

Fig. 6.1.1 (a) Combining TDM with AO for mode control at different locations within a TMF; (b) Experiment setup of TDM and AO-based mode control using transmission and reflection signals as feedback: DFB, distributed feedback laser; SMF, single mode fiber; EOM, electro-optic modulator; L1, collimator; DM, deformable mirror; BS1 and BS2, beam splitter; L2, 10× objective lens, NA=0.25; TMF, OFS two mode fiber; FBG1 and FBG2, fiber Bragg grating; L3, 100× objective lens, NA=0.70; CCD, infrared CCD camera; L4 and L5, lens; PD1 and PD2, photodetector; PC, computer.

Figure 6.1.1(a) illustrates the principle of our method. As shown in Fig. 6.1.1(a), our method requires multiple inline FBGs in a TMF and uses pulsed optical signals for mode control. Since the speed of light in a TMF can be easily determined in advance, we can associate any reflected signal with the FBG that produces the signal, based on the arrival time of the reflected signal. As a result, if we want to selectively excite a specific LP mode near any given FBG, all we need to do is to use the reflection signal produced by the desired FBG for AO feedback. As a proof-of-concept experiment, we consider only two gratings in the current work, as shown in Fig. 6.1.1(a). In the future, by inscribing multiple ultra-weak FBGs within a TMF network, we can apply the method developed here for mode control within the two-mode FBG sensor network.

An experimental implementation of this design is shown in Fig. 6.1.1(b). A distributed feedback (DFB) laser (QPhotonics, QDFBLD-1550-20) is thermally tuned to operate at 1529.70 nm. An electro-optic modulator (EOM), together with a pulse generator, is used to generate interrogation signals for mode control. After modulation, the optical signals are coupled into free space using a collimator (L1), phase-modulated by a deformable mirror (DM, Boston Micromachines), and coupled back into a ~345 meter long TMF by an objective lens (L2, 10×). The TMF (OFS) possesses a step-index profile and supports the LP_{01} and the LP_{11} modes at the operation wavelength. For adaptive mode control, we custom ordered two FBGs that were directly written in the TMF by Ascentta Inc. These two FGBs are spliced into the TMF, with FBG1 placed ~ 200 meter far away from the fiber input port, and FBG2 spliced near the output port of the TMF. At the output of the TMF, we use an objective lens (L3, 100×) and a near infrared CCD camera (Allied Vision Technologies, Goldeye-032) to capture the output intensity profile. Since FBG2 is placed near the output port of the TMF, we can use the CCD images to confirm the results of mode control experiments. It should be emphasized that the intensity profiles are not used in our adaptive algorithm, and are for validation only. A beam splitter (BS1) is placed before L2 to collect FBG reflection signals. The strength of the reflection signal is measured using a photodetector (PD1). Similarly, another beam splitter (BS2) and photodetector (PD2) are placed behind L3 to detect transmission signals. Signals from the two PDs are acquired by a digitizer (National Instruments, NI-5114, 250 MS/s sampling

rate), and analyzed by the computer (PC) to provide the feedback for the DM for adaptive mode control.

The reflection spectra of the two FBGs are measured using a component test system (CTS, Micron Optics, HR-SLI) and a circulator, as shown in Fig. 5.1.2(a) previously. Both the CTS and the circular are connected using the standard single mode fiber (SMF-28). The FBG, written in the TMF, is directly spliced to the SMF. We intentionally introduce a small misalignment for the SMF-TMF splice, which ensures that the LP_{01} mode in the SMF can excite a mixture of the LP_{01} and the LP_{11} mode in the TMF. Representative measurement results for the two FBGs are shown in Fig. 6.1.2. As discussed in Chapter 5.1, we can attribute the dominant peak at ~1529.70 nm to the LP_{01} mode, and the much weaker one at ~1528.35 nm to the LP_{11} mode. Though the reflection magnitudes of the two FBGs are slightly different, their reflection peaks are well matched and are located at almost identical wavelengths.

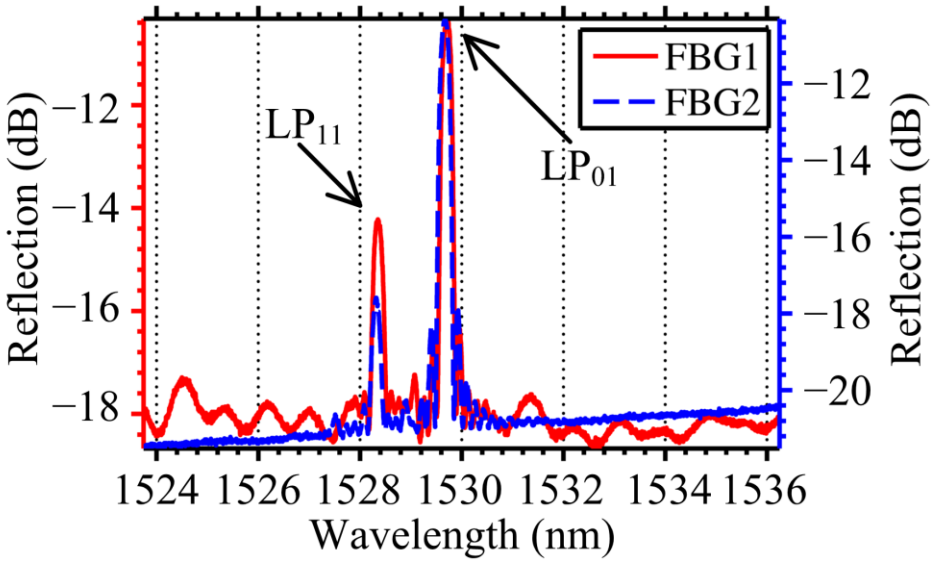

Fig. 6.1.2 Representative FBG reflection spectra (red solid line for FBG1 and blue dash line for FBG2).

Adaptive mode control is based on the optimization algorithm described in Section 2.7. In order to control the mode within the TMF, we first define an objective function *F* for AO feedback:

$$F^{(i)} = \frac{V_T}{V_R^{(i)}} \propto \frac{P_T}{P_R^{(i)}} \tag{6.1.1}$$

where P_T denotes transmitted signal power, and $P_R^{(i)}$ represents the power of the signal reflected by the *i*th FBG. The superscript *i*, which can be either 1 or 2, denotes the FBG that produces the reflected pulse and is identified through the pulse arrival time. In our experiments, the transmitted and reflected power are replaced by the corresponding PD voltage, i.e., V_T and $V_R^{(i)}$. Clearly, our feedback signal $F^{(i)}$ is proportional to the ratio of optical transmission and reflection of the *i*th FBG.

The principle of adaptive mode control is based on the observation that at an appropriate wavelength, FBG reflection in a TMF can be highly mode dependent, as can be clearly seen in Fig. 6.1.2. In our experiments, we set the operation wavelength at 1529.70 nm, which coincides with the reflection peak of the LP_{01} mode. If the incident wave is purely LP_{01}, it experiences maximum reflection and minimum transmission, which means a relatively small feedback signal $F^{(i)}$. On the other hand, a pure LP_{11} incident signal should produce minimal FBG reflection, thus resulting in a very large feedback value $F^{(i)}$. Therefore, by maximizing the feedback function $F^{(i)}$ in Eq. (6.1.1), we should be able to selectively excite a pure LP_{11} mode at the *i*th FBG location. Experimentally, the adaptive feedback process is achieved by adjusting the wavefront of the optical wave reflected by the DM. Briefly, for any given DM modulation block (out of 140), we vary its phase shift value from 0 to ~2π. Afterwards, we set its phase shift value to be the one that maximizes $F^{(i)}$, and move on to the next DM block. A single iteration, sequentially carried out for all 140 blocks, is referred to as one optimization cycle. For a more detailed description, refer to Section 2.7.

6.1.2 Experiment Results

To verify the feasibility of time-domain-based mode control, we first carry out experiments using only one FBG. Experimentally, this is accomplished by removing FBG1 from the setup in Fig. 6.1.1(b), with only FBG2 spliced at the end of the ~145 meter long TMF. In the experiments, the modulation pulse width is 300 ns (including 100 ns rising and falling edges), and the repetition frequency is 250 kHz. During phase modulation of individual DM blocks, the digitizer samples the PD signals within a 400 μs window. We determine the values of V_T and $V_R^{(i)}$ by averaging PD signals within the 400 μs window. With V_T and $V_R^{(i)}$ known, we can apply the AO algorithm and set the optical

field at the output to be the LP_{11} mode. The results of four representative experiments (labelled as Ex1-Ex4) are shown in Fig. 6.1.3.

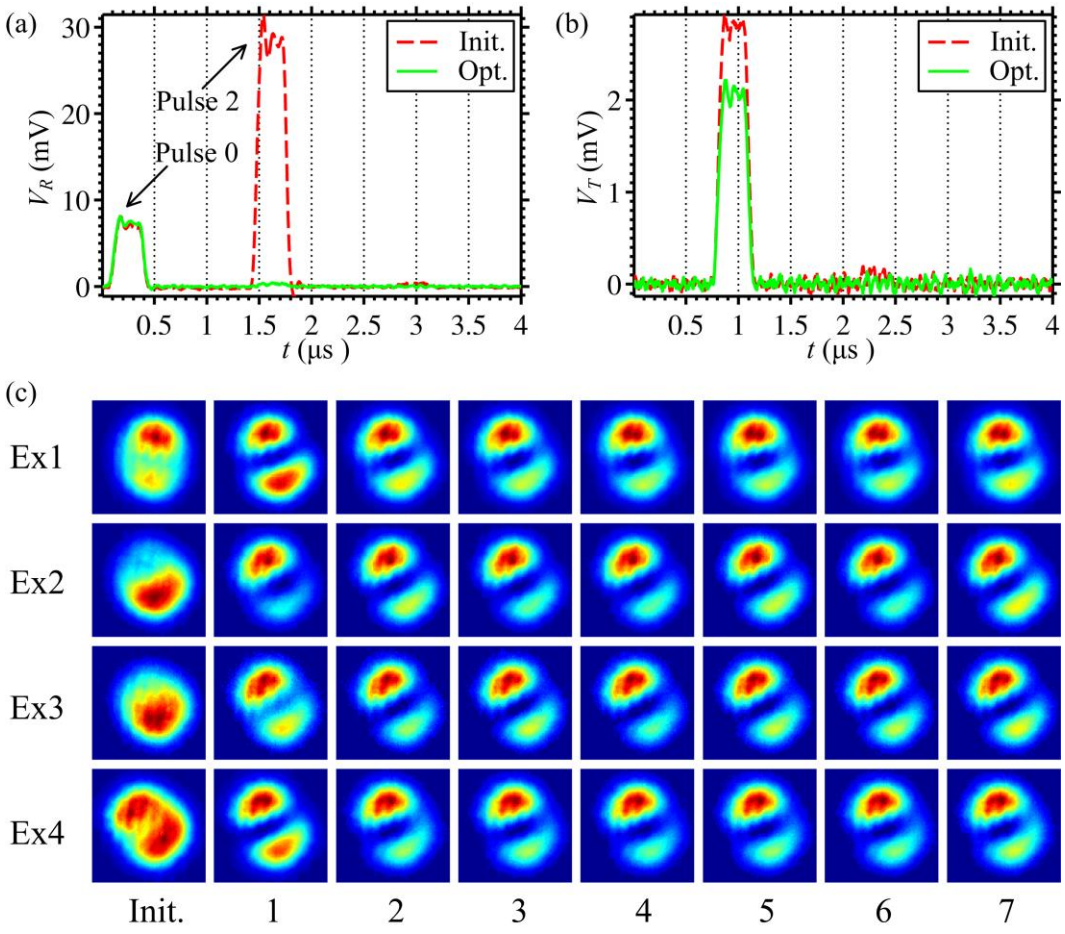

Fig. 6.1.3 Experiment results of adaptive mode control using one FBG. (a) The time dependence of the initial (labeled as "Init.") and the optimized (labeled as "Opt.") reflection signals; Two pulses, produced by the front cleaved fiber facet (Pulse 0), and FBG 2 (Pulse 2), can be clearly seen; (b) the time dependence of the transmitted signal. The results in (a) and (b) are for Ex1 only; (c) the initial optical intensity profile and the intermediate optical field distributions at the end of cycle 1 to cycle 7 (individually labelled by the cycle numbers) for Ex1-Ex4.

Figures 6.1.3(a) and 6.1.3(b) show the initial and optimized reflection and transmission pulses (labeled as "Init." and "Opt." respectively) of Ex1. Note that the reflected signals detected by PD1 contain two pulses, with the first one (Pulse 0) produced by the front facet of the TMF, and second one (Pulse 2) by FBG2. The temporal separation between

the two pulses (~1.4 μs) corresponds to a fiber length of ~145 m. We use Pulse 2 as feedback for adaptive mode control. Clearly, after optimization, the amplitude of Pulse 2 (i.e., $V_R^{(2)}$) becomes close to the minimal resolvable level (0.156 mV) of the digitizer, whereas reflection due to the cleaved TMF front facet remains similar. This measurement result is consistent with the presence of pure LP_{11} mode at FBG2. Figure 6.1.3(c) shows the initial and the intermediate field distributions at the end of each optimization cycle (1-7) of Ex1-Ex4. The initial distributions in Fig. 6.1.3(c) are intentionally chosen to be significantly different from the desired LP_{11} mode profiles. Yet after optimization, the final intensity profiles are the superposition of two degenerate LP_{11} modes, since the pixel intensities at the center are very close to zero. From Ex1 in Fig 6.1.3(c) we can see the result agrees well with Figs. 6.1.3(a) and 6.1.3(b). Additionally, Figure 6.1.3(c) suggests that it generally takes 1 or 2 optimization cycles for the output field to become almost purely LP_{11}.

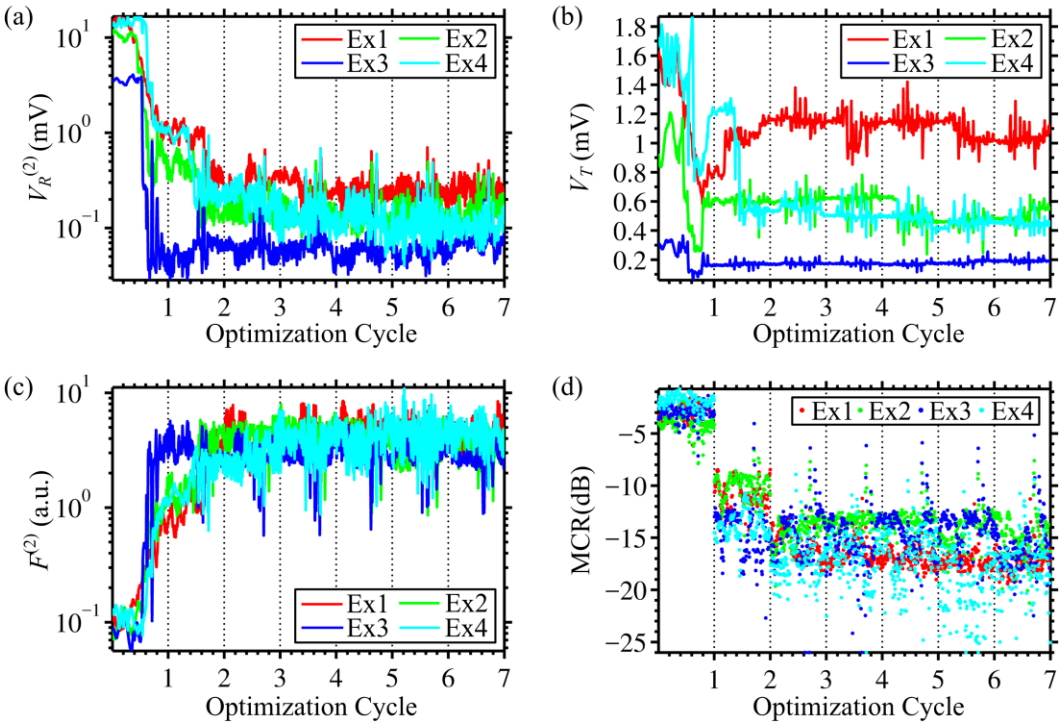

Fig. 6.1.4 (a) The reflected pulse magnitude $V_R^{(2)}$; (b) transmitted pulse magnitude V_T; (c) the feedback function $F^{(2)}$; and (d) MCR obtained during the seven optimization cycles of Ex1-Ex4.

Figures 6.1.4(a)-6.1.4(c) show the variations of $V_R^{(2)}$, V_T, and the feedback function $F^{(2)}$ during the entire optimization process (seven cycles in total) of Ex1-Ex4. Within each optimization cycle, all three values exhibit significant variations. This is due to the fact that the DM inevitably produces numerous "wrong" wavefronts before selecting the most appropriate one for the desired outcome. However, it is clear that $V_R^{(2)}$ (associated with FBG2 reflection) tends to decrease consistently throughout the entire optimization process. From Fig. 6.1.4(c) we can see that, generally after 1-2 cycles of optimization, the value of the feedback function become reasonably close to its final outcome. It agrees well with our observation in Fig. 6.1.3(c).

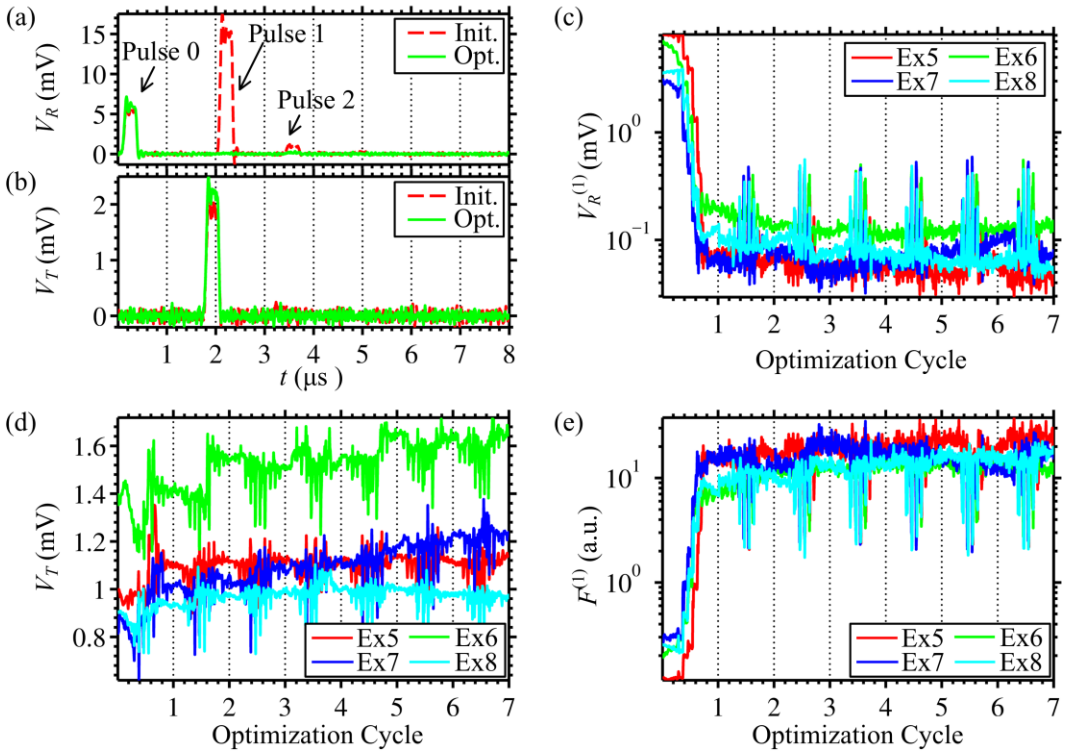

Fig. 6.1.5 Experiment results of selectively excitation of the LP_{11} mode at FBG1. The initial (labeled as "Init.") and the optimized (labeled as "Opt.") (a) reflection pulses; and (b) transmission pulses for Ex5. The variations of (c) $V_R^{(1)}$; (d) V_T; and (e) the feedback function $F^{(1)}$ during the seven optimization cycles of Ex5-Ex8.

To quantitatively analyze the composition of the LP modes during optimization, we utilize the MCR defined in Chapter 4.2, and the only difference is that the minimal intensity $I_{\min}$ is defined within a small 7×7 pixel block at the center of the fiber core (out

of the 80×80 pixel image). Figure 6.1.4(d) shows the variations of MCR during optimization of Ex1-Ex4. As we can see, after three optimization cycles, the MCR for all four representative experiments falls below −15dB. Considering the effect of CCD noises, Figure 6.1.4(d) reasonably confirms that the optical field at the FBG location should be almost entirely LP_{11}.

The above experiments confirm the feasibility of adaptive mode control based on time-domain measurements. In the following experiments, we show that the TDM and AO-based method can be used for mode control at different FBG locations within the TMF. To demonstrate this, we splice FBG1, as well as the ~200-meter-long TMF preceding it, with the ~145-meter-long TMF containing FBG2, according to Fig. 6.1.1(b). During experiments, the modulation pulse is the same except that pulse repetition rate is set to 125 kHz. All other experimental parameters and procedure remain the same. First, we demonstrate LP_{11} mode excitation at FBG1. The AO-based mode control is achieved using Pulse 1 produced by FBG1. The results of four represent experiments (labelled as Ex5-Ex8) are shown in Fig. 6.1.5. Figures 6.1.5(a) and 6.1.5(b) show the initial and optimized reflection and transmission pulses for Ex5. The reflected signal in Fig. 6.1.5(a) clearly contains three pulses, one by the front fiber facet (Pulse 0), and the other two produced by FBG1 and FBG2 (Pulse 1 and 2), respectively. In our experiments, we first set the optical field at FBG1 to be the LP_{11} mode. It is clear after optimization, the reflection from FBG1 decrease to a value close to the minimal resolvable level of the digitizer, and the transmission increases slightly. Figures 6.1.5(c)-6.1.5(e) show the values of $V_R^{(1)}$, V_T and the feedback function $F^{(1)}$ obtained during the entire seven optimization cycles. According to Fig. 6.1.5, after 2-3 cycles, the value of $V_R^{(1)}$ decreases to a value reasonably close to the final outcome [Fig. 6.1.5(c)], and the value of $F^{(1)}$ improves by more than 50 times [Fig. 6.1.5(e)]. These results suggest that it only takes 2-3 cycles to achieve selective excitation of the LP_{11} mode at FBG1.

The method reported here can also be used to selectively excite the LP_{11} mode at FBG2. Due to the strong reflection from FBG1, the signal reflected by FBG2 is relatively weak, since it has to pass through FBG1 twice. To solve this problem, we place FBG1 in a custom-built oven and heat FBG1 to 37℃. With increasing the temperature, we shift the reflection peak of FBG1 by ~0.13 nm, and reduce its reflection magnitude at 1529.70 nm

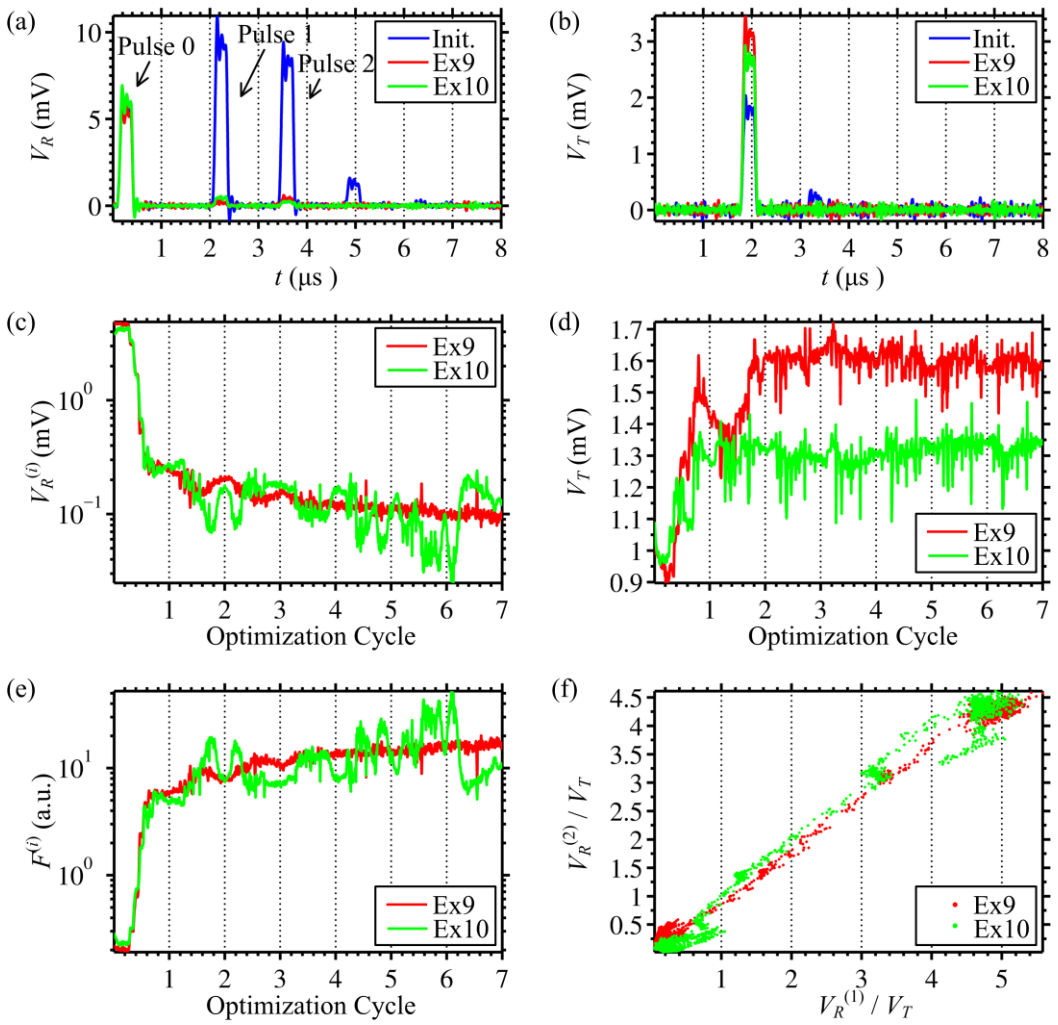

Fig. 6.1.6 Representative experiment Ex9 (or Ex10) that shows selectively excitation of the LP_{11} mode at FBG1 (or FBG2). The initial (labeled as "Init.") and the optimized (a) reflection pulses; and (b) transmission pulses of Ex9 and Ex10. The variations of (c) $V_R^{(i)}$; (d) V_T; and (e) the feedback function $F^{(i)}$ during the seven optimization cycles (i = 1 for Ex9, and 2 for Ex10). (e) The ratio of $V_R^{(2)}/V_T$ versus $V_R^{(1)}/V_T$ during the optimization for Ex9 and Ex10.

by ~3.5 dB. The results of two representative experiments (Ex9 and Ex10) are shown in Fig. 6.1.6. The initial and optimized pulses of Ex9 and Ex10 are shown in Figs. 6.1.6(a) and 6.1.6(b). In Ex9 (or Ex10), we adaptively optimize the mode at FBG1 (or FBG2) to pure LP_{11} mode, by using Pulse 1 (or Pulse 2) as feedback, respectively. Comparing the initial and optimized pulses, we can see the reflection due to the target FBG after

optimization is close to the minimal resolvable level of the digitizer, which indicates that the mode at desired FBG location is close to pure LP_{11}. Figures 6.1.6(c)-6.1.6(e) show the values of $V_R^{(i)}$, V_T and the feedback function $F^{(i)}$ obtained during the entire seven optimization cycles (i = 1 for Ex9, and 2 for Ex10). As we can see from Fig. 6.1.6(c), after 2-3 cycles, the value of $V_R^{(i)}$ decrease to a value close to the minimal value after optimization, and the feedback function $F^{(i)}$ in Fig. 6.1.6(e) is reasonably close to the final outcome. These results agree well with Figs. 6.1.4 and 6.1.5. (The "extra" pulse at ~5 μs in Fig. 6.1.6(a) is likely due to multiple reflections by the two FBGs.)

It is interesting to note from Fig. 6.1.6(a) that, after optimization, the reflection from both FBGs decrease to almost zero. To understand this phenomenon, Fig. 6.1.6(f) plots the ratio of $V_R^{(2)}/V_T$ versus $V_R^{(1)}/V_T$ during the optimization for Ex9 and Ex10. Since we intentionally introduce significant variations to the LP mode compositions during optimization, the value of $V_R^{(i)}/V_T$ fluctuates in a wide range in Fig. 6.1.6(f). However, despite the significant variations in the absolute values of $V_R^{(i)}/V_T$, the power reflection coefficients associated with the two gratings exhibit strong linear relationship. It implies that the mode compositions at these two FBG locations should be very similar, which indicates that the effect of intermodal coupling in the ~145 meter long TMF is not significant. Such information is important for many applications including MDM, and FMF-based sensing as well as imaging.

For optical communication and sensing, it is important that we can efficiently couple optical power into the fiber network. This requirement was not addressed in our previous work. Here we slightly modify the adaptive algorithm reported above to achieve adaptive mode control and reasonable coupling efficiency. The modification is minor: When setting the phase shift value of individual DM blocks during wavefront optimization, we only update the phase value if the updated value both maximizes $F^{(i)}$ and increases the transmission V_T; Otherwise, the phase value will not be updated. This algorithm has been applied in Ex5-Ex10, and we can see the transmission V_T increases after the optimization in Figs. 6.1.5(d) and 6.1.6(d). Compared with the original AO algorithm, this simple modification can improve our coupling efficiency by a factor of two or more. In our experiments we can typically achieve a coupling efficiency in the range of 10% to 30%.

6.2 Mode Control Based on Reflection Signals

6.2.1 Experiment Setup and AO Algorithm

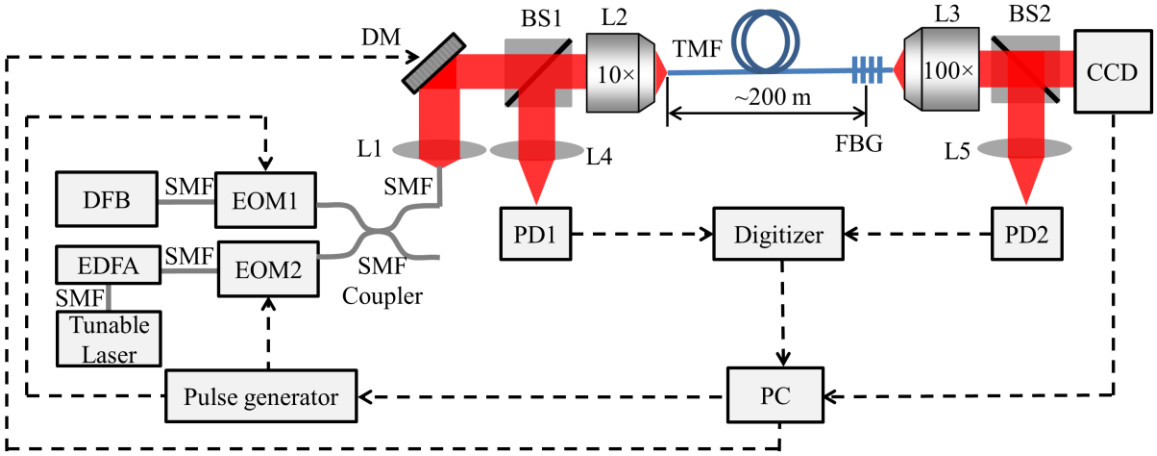

Fig. 6.2.1 Experimental setup of TDM and AO-based mode control using only reflection signals as feedback: DFB, distributed feedback laser; SMF, single mode fiber; EDFA, Erbium-doped fiber amplifier; EOM1 and EOM2, electro-optic modulator; L1, collimator; DM, deformable mirror; BS1 and BS2, beam splitter; L2, 10× objective lens, NA=0.25; TMF, OFS two mode fiber; FBG, fiber Bragg grating; L3, 100× objective lens, NA=0.70; CCD, infrared CCD camera; L4 and L5, lens; PD1 and PD2, photodetector; PC, computer.

Results in the previous section demonstrate that we can combine TDM, MDM, and AO to achieve adaptive mode control at multiple locations within a fiber optical network. While the feedback requires both the reflection signal and transmission signal at the distal end of the fiber. A natural question that arises next is whether we can adaptively control the mode within the TMF by using only reflection signals. To answer this question, we consider the experiment setup shown in Fig. 6.2.1, which is very similar to the previous setup in Fig. 6.1.1(b) except for the addition of a tunable laser, and we use only one FBG in the setup for a proof-of-concept demonstration. Specifically, a tunable laser (New Focus, 6328; amplified by an EDFA) and the DFB laser are modulated separately by two EOMs (controlled by a 2-channel pulse generator) and then combined into a SMF through a 3dB SMF coupler. FBG2 and the ~145 meter long TMF in Fig. 6.1.1 are

removed from the setup. All other components are the same. During experiments, the DFB laser wavelength is set to 1529.70 nm (denoted as λ_{01}^{FBG}), which is the FBG peak reflection wavelength associated with the LP_{01} mode in Fig. 6.1.2. The tunable laser wavelength, set to 1528.35 nm (denoted as λ_{11}^{FBG}), is the FBG peak reflection wavelength associated with the LP_{11} mode. A particularly attractive feature of the design is that we only use reflected signals for adaptive mode control: only signals detected by PD1 are used as feedback for AO-based mode control. Optical signals detected by PD2 and the CCD are used for validation only. In our experiments, there is a time delay between the DFB laser pulses and the tunable laser pulses. Consequently, the reflection signals produced by the FBG can be distinguished by their arrival time.

Similar to all previous experiments, adaptive mode control is based on the optimization algorithm described in Section 2.7. For setting the optical wave to be purely LP_{11}, we use the following objective function F_{11} for AO feedback,

$$F_{11} = \frac{V_R(\lambda_{11}^{FBG})}{V_R(\lambda_{01}^{FBG})} \propto \frac{P_{11}(\lambda_{11}^{FBG})}{P_{01}(\lambda_{01}^{FBG})} \tag{6.2.1}$$

for optimizing the mode to be purely LP_{01}, we use F_{01} defined as

$$F_{01} = \frac{1}{F_{11}} = \frac{V_R(\lambda_{01}^{FBG})}{V_R(\lambda_{11}^{FBG})} \propto \frac{P_{01}(\lambda_{01}^{FBG})}{P_{11}(\lambda_{11}^{FBG})} \tag{6.2.2}$$

where $P_{01}(\lambda_{01}^{FBG})$ represents the power of the LP_{01} mode at λ_{01}^{FBG}=1529.70 nm at the FBG location; $P_{11}(\lambda_{11}^{FBG})$ denotes the power of the LP_{11} mode at λ_{11}^{FBG}=1528.35 nm at the FBG location. During our experiments, $P_{01}(\lambda_{01}^{FBG})$ and $P_{11}(\lambda_{11}^{FBG})$ are represented by corresponding PD voltages, *i.e.* $V_R(\lambda_{01}^{FBG})$ and $V_R(\lambda_{11}^{FBG})$. As mentioned, the reflected pulses are identified through their pulse arrival time.

Given the small wavelength difference (~1.35 nm) between the DFB laser and the tunable laser, we expect that the input coupling and wavefront control system should behave similarly at both wavelengths. To make our discussion more precise, we denote the input power of the DFB laser and the tunable laser as $P^{in}(\lambda_{01}^{FBG})$ and $P^{in}(\lambda_{11}^{FBG})$ (right before both laser beam pass through L1 in Fig. 6.2.1). At the FBG location within the TMF, the DFB laser power carried by the LP_{01} and LP_{11} modes can be expressed as $A_{01}(\lambda_{01}^{FBG})P^{in}(\lambda_{01}^{FBG})$ and $A_{11}(\lambda_{01}^{FBG})P^{in}(\lambda_{01}^{FBG})$, respectively. Similarly, we denote the tunable laser power carried by

the LP_{01} and the LP_{11} modes at the FBG location as $A_{01}(\lambda_{11}^{FBG})P^{in}(\lambda_{11}^{FBG})$ and $A_{11}(\lambda_{11}^{FBG})P^{in}(\lambda_{11}^{FBG})$, respectively. If the input coupling system (including the DM) and the intermodal coupling within the TMF impact both wavelengths similarly, we should expect $A_{01}(\lambda_{01}^{FBG}) \sim A_{01}(\lambda_{11}^{FBG})$ and $A_{11}(\lambda_{01}^{FBG}) \sim A_{11}(\lambda_{11}^{FBG})$. Given these notations, Eqs (6.2.1) and (6.2.2) can be expressed as:

$$F_{11} \propto \frac{P^{in}(\lambda_{11}^{FBG})A_{11}(\lambda_{11}^{FBG})}{P^{in}(\lambda_{01}^{FBG})A_{01}(\lambda_{01}^{FBG})} \propto \frac{A_{11}(\lambda_{11}^{FBG})}{A_{01}(\lambda_{01}^{FBG})} \sim \frac{A_{11}(\lambda_{01}^{FBG})}{A_{01}(\lambda_{01}^{FBG})} \tag{6.2.3}$$

$$F_{01} \propto \frac{P^{in}(\lambda_{01}^{FBG})A_{01}(\lambda_{01}^{FBG})}{P^{in}(\lambda_{11}^{FBG})A_{11}(\lambda_{11}^{FBG})} \propto \frac{A_{01}(\lambda_{01}^{FBG})}{A_{11}(\lambda_{11}^{FBG})} \sim \frac{A_{01}(\lambda_{11}^{FBG})}{A_{11}(\lambda_{11}^{FBG})} \tag{6.2.4}$$

Thus, maximizing the feedback function F_{11} approximately maximizes the ratio of the power carried by the LP_{11} and the LP_{01} modes at λ_{01}^{FBG} at the FBG location. If the incident wave is purely LP_{11} mode at λ_{01}^{FBG}, it experiences minimal reflection and maximum transmission, which means a very large feedback signal F_{11}. Therefore, by maximizing the feedback function F_{11}, we should be able to selectively excite LP_{11} mode at λ_{01}^{FBG} at the FBG location. Similarly, maximizing feedback function F_{01} should optimize the mode to be pure LP_{01} at λ_{11}^{FBG} at the FBG location. Experimentally, the feedback function F_{11} (or F_{01}) is used in conjunction with the voltage of the reflection pulse $V_R(\lambda_{11}^{FBG})$ (or $V_R(\lambda_{01}^{FBG})$), when we optimize the optical field at the FBG to be purely LP_{11} (or LP_{01}). It is similar to the optimization algorithm used in Ex5-Ex10 of Section 6.1. As discussed previously, this simple modification allows us to adaptively control the optical field while achieving reasonable coupling efficiency.

6.2.2 Experiment Results

Using the algorithm described above, we adaptively control the mode at the FBG location to be pure LP modes. During experiments, the pulse width of both the tunable laser and the DFB laser is ~300 ns (including 100 ns rising and falling edges). The repetition frequency is set to 125 kHz. Additionally, there is a ~3.9 μs delay between the DFB laser pulse (modulated by EOM1) and the tunable laser pulse (modulated by EOM2). Same as previous experiments in Section 6.1, the digitizer samples the PD signals within a 400 μs window during phase modulation of individual DM blocks. We determine the reflection

pulse voltage V_R and transmission pulse voltage V_T by averaging PD signals within the 400 μs window.

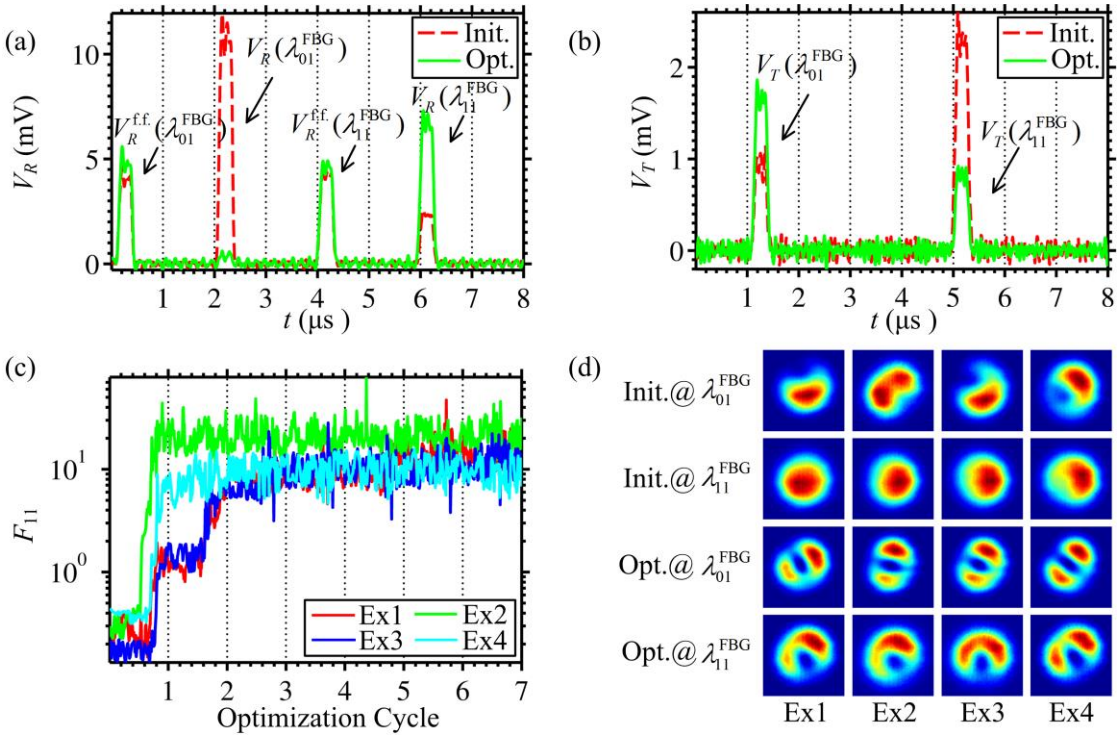

Fig. 6.2.2 Experiment results of selective excitation of the LP_{11} mode. (a) and (b) show the initial (labeled as "Init.") and the optimized (labeled as "Opt.") reflection pulses and transmission pulses for Ex1; (c) The variations of the feedback function F_{11} obtained during the seven optimization cycles of Ex1-Ex4; (d) The initial and optimized optical intensity profiles at λ_{01}^{FBG} and λ_{11}^{FBG}.

First, we show selective excitation of the LP_{11} mode at the FBG location by using F_{11} defined in Eq. (6.2.1) as feedback. Results of four representative experiments (labelled as Ex1-Ex4) are shown in Fig. 6.2.2. Figures 6.2.2(a) shows the initial and optimized reflection pulses (labeled as "Init." and "Opt." respectively) of Ex1, and 6.2.2(b) shows corresponding transmission pulses. Note that the reflected signals detected by PD1 contain four pulses. The first two are reflection pulses of the DFB laser produced by the fiber front facet (denoted as f.f.) and the FBG, denoted as $V_R^{f.f.}(\lambda_{01}^{FBG})$ and $V_R(\lambda_{01}^{FBG})$ respectively. Similarly, the second two are reflection pulses of the tunable laser, represented by $V_R^{f.f.}(\lambda_{11}^{FBG})$ and $V_R(\lambda_{11}^{FBG})$. The ~3.9 μs delay between the transmission pulses of DFB laser and the tunable laser is clearly shown in Fig. 6.2.2(b). The two transmission

pulse are labelled as $V_T(\lambda_{01}^{FBG})$ and $V_T(\lambda_{11}^{FBG})$, respectively. It is clear that after optimization, $V_R(\lambda_{01}^{FBG})$ becomes close to the minimal resolvable level of the digitizer, whereas $V_R(\lambda_{11}^{FBG})$ increases apparently. This measurement result is consistent with the presence of almost pure LP_{11} mode at λ_{01}^{FBG} at the FBG location. It agrees well with Fig. 6.2.2(b), in which we notice $V_T(\lambda_{01}^{FBG})$ increases, while $V_T(\lambda_{11}^{FBG})$ decreases clearly after optimization.

Figure 6.2.2(c) shows the feedback function F_{11} obtained during the seven optimization cycles of Ex1-Ex4. From Fig. 6.2.2(c) we can see, after 2-3 cycles of optimization, the feedback function value becomes reasonably close to the final outcome. It suggests that it generally takes 2 or 3 optimization cycles for the field at the FBG location become almost purely LP_{11} at λ_{01}^{FBG}. Figure 6.2.2(d) shows the initial and the final optimized field distributions of Ex1-Ex4 at both λ_{01}^{FBG} and λ_{11}^{FBG}. The initial distributions are intentionally chosen to be significantly different from the desired LP_{11} mode profiles. Yet after optimization, the final intensity profiles suggest that the optical fields at λ_{01}^{FBG} are the superposition of two degenerated LP_{11} modes, since the pixel intensities at the center are very close to zero. The optimized optical fields at λ_{11}^{FBG} are dominated by the LP_{11} mode as well because that even the MCR in the worst result is lower than 0.12, which is significantly lower than that of the initial field. Results in Fig. 6.2.2(d) clearly verify our AO algorithm for selective excitation of LP_{11} mode at the FBG location.

Figures 6.2.3(a)-6.2.3(d) show the variations of $V_R(\lambda_{01}^{FBG})$, $V_R(\lambda_{11}^{FBG})$, $V_T(\lambda_{01}^{FBG})$, and $V_T(\lambda_{11}^{FBG})$ during the entire optimization process (seven cycles in total) of Ex1-Ex4. Within each optimization cycle, all three values exhibit significant variations. However, the generally trend is clear: $V_R(\lambda_{01}^{FBG})$ tends to decrease consistently throughout the entire optimization process; $V_R(\lambda_{11}^{FBG})$ generally increases after the optimization; after optimization, $V_T(\lambda_{01}^{FBG})$ increases slightly; $V_T(\lambda_{11}^{FBG})$ decreases consistently throughout the entire optimization process. These results should be expected, since pure LP_{11} mode at λ_{01}^{FBG} should produce very low reflection [Fig. 6.2.3(a)] and high transmission signals [Fig. 6.2.3(c)]. Additionally, if the system behaves similarly at λ_{11}^{FBG}, the optical field at λ_{11}^{FBG} should be close to pure LP_{11} mode, thus it experiences high reflection [Fig. 6.2.3(b)] and low transmission [Fig. 6.2.3(d)]. From Figs. 6.2.3(a)-6.2.3(d) we can also see that, generally after 2-3 optimization cycles, the values of all signals become reasonably close to those after optimization. Results in Figs. 6.2.3(a)-6.2.3(d) agree well with our observations in

Figs. 6.2.2(a)-6.2.2(d) that, selective excitation of almost pure LP_{11} mode at λ_{01}^{FBG} can be accomplished at the FBG location after optimization.

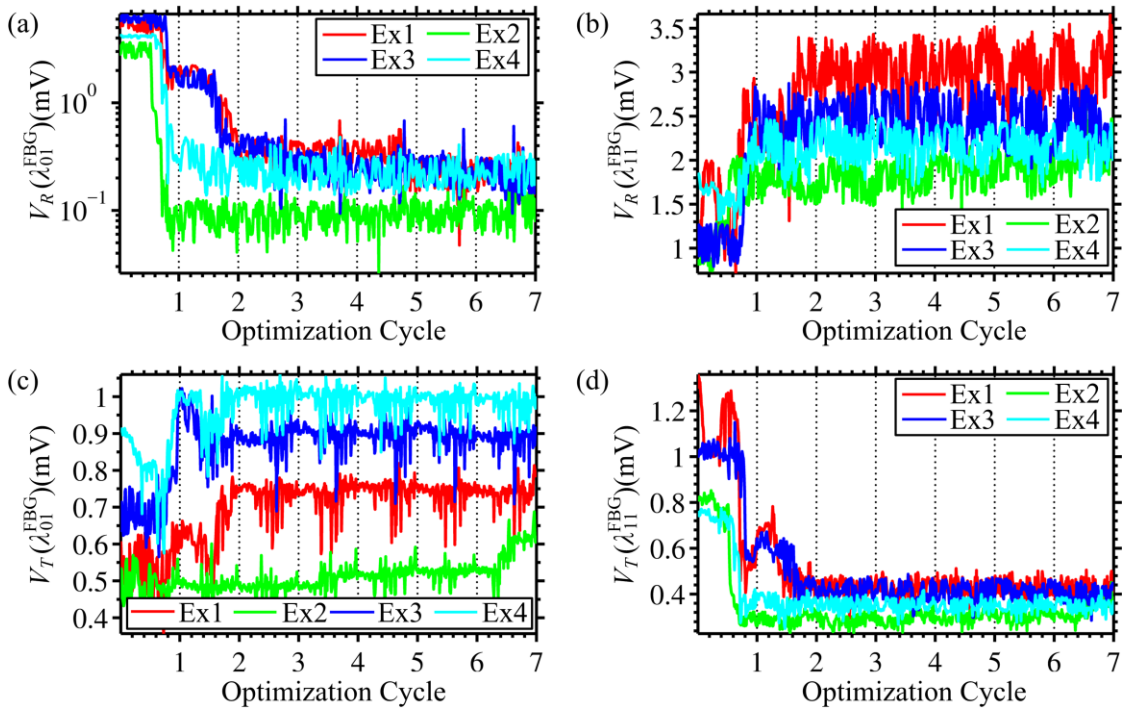

Fig. 6.2.3 The variations of (a) $V_R(\lambda_{01}^{FBG})$; (b) $V_R(\lambda_{11}^{FBG})$; (c) $V_T(\lambda_{01}^{FBG})$; and (d) $V_T(\lambda_{11}^{FBG})$ during the seven optimization cycles of Ex1-Ex4.

By using F_{01} defined in Eq. (6.2.2) as feedback, we can adaptively control the mode at the FBG to be almost pure LP_{01} mode. Results of four representative experiments (labelled as Ex5-Ex8) are shown in Fig. 6.2.4. Figures 6.2.4(a) and 6.2.4(b) show the reflection and the transmission pulses of Ex5 before and after optimization, with individual pulses labelled accordingly. It is clear that after optimization, $V_R(\lambda_{11}^{FBG})$ decreases dramatically to a small residual value, whereas $V_R(\lambda_{01}^{FBG})$ increases slightly. These results agree with the apparent decreasing of $V_T(\lambda_{01}^{FBG})$ in Fig. 6.2.4(b). During experiments, we find out the residual value of $V_R(\lambda_{11}^{FBG})$ is typically between 0.5 mV to 0.8 mV. This residue might be due to several factors, such as the amplified spontaneous emission noise of the EDFA (~ 0.2-0.3 mV) and the side lobe of the FBG reflection peaks. Taking these factors into account, the optical field at the FBG location after optimization should be reasonably close to pure LP_{01} mode at λ_{11}^{FBG}. It is noted that after optimization,

$V_T(\lambda_{11}^{FBG})$ decrease slightly, which indicates that the system coupling ratio at λ_{11}^{FBG} may be slightly reduced after optimization.

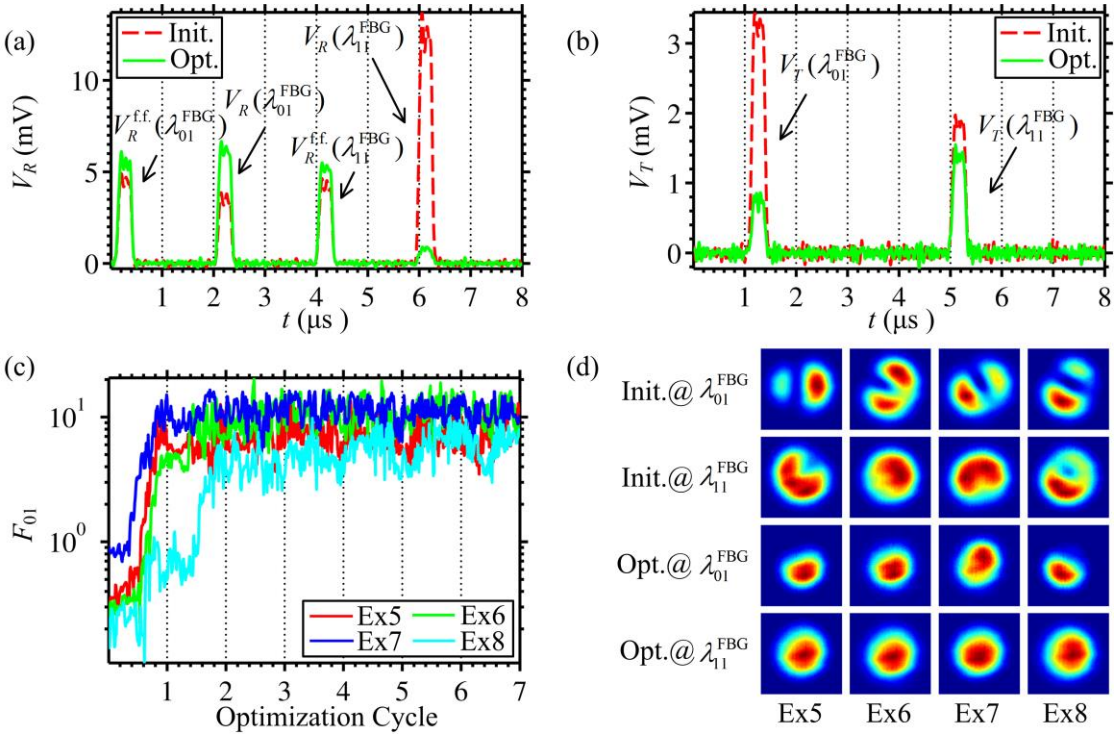

Fig. 6.2.4 Experiment results of selective excitation of the LP_{01} mode. (a) and (b) show the initial (labeled as "Init.") and the optimized (labeled as "Opt.") reflection pulses and transmission pulses for Ex5; (c) The variations of the feedback function F_{01} during the seven optimization cycles of Ex5-Ex8; (d) The initial and optimized optical intensity profiles at λ_{01}^{FBG} and λ_{11}^{FBG}.

Figure 6.2.4(c) shows the feedback function F_{01} obtained during the seven optimization cycles of Ex5-Ex8. Again, from Fig. 6.2.4(c) we can see that, after 2-3 cycles of optimization, the feedback function value becomes reasonably close to the final outcome. It suggests that it generally takes 2 or 3 cycles for optimizing the field at the FBG location to be almost pure LP_{01} at λ_{11}^{FBG}. Figure 6.2.4(d) shows the initial and the final optimized field distributions of Ex5-Ex8 at both λ_{01}^{FBG} and λ_{11}^{FBG}. The initial distributions are intentionally chosen to be significantly different from the desired LP_{01} mode profiles. Yet after optimization, the final intensity profiles suggest that the optical fields at λ_{11}^{FBG} are reasonably close to pure LP_{01} modes. In addition, the LP_{01} mode power of the optimized

optical fields at λ_{01}^{FBG} should be significant as well. Results in Fig. 6.2.4(d) verify the AO algorithm for selective excitation of LP_{01} mode at λ_{11}^{FBG} at the FBG location.

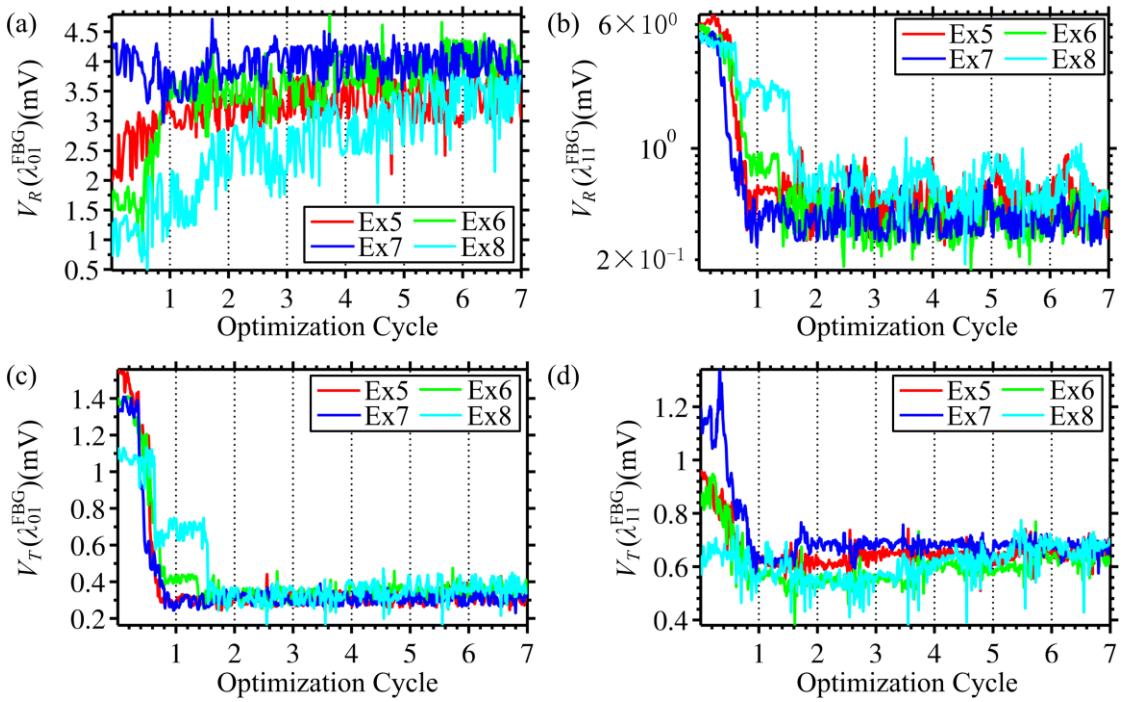

Fig. 6.2.5 The variations of (a) $V_R(\lambda_{01}^{FBG})$; (b) $V_R(\lambda_{11}^{FBG})$; (c) $V_T(\lambda_{01}^{FBG})$; and (d) $V_T(\lambda_{11}^{FBG})$ during the seven optimization cycles of Ex5-Ex8.

Figures 6.2.5(a)-6.2.5(d) show the variations of $V_R(\lambda_{01}^{FBG})$, $V_R(\lambda_{11}^{FBG})$, $V_T(\lambda_{01}^{FBG})$, and $V_T(\lambda_{11}^{FBG})$ during the seven optimization cycles of Ex5-Ex8. Again, within each optimization cycle, all three values exhibit significant variations. However, we can see that: $V_R(\lambda_{01}^{FBG})$ generally increases after the optimization; $V_R(\lambda_{11}^{FBG})$ tends to decrease consistently throughout the entire optimization process; $V_T(\lambda_{01}^{FBG})$ decreases consistently to a lower value (~0.3 mV) during the seven optimization cycles. All these results are to be expected: pure LP_{01} mode at λ_{11}^{FBG} experiences low reflection [Fig.6.2.5(b)]; if the optical field is close to pure LP_{01} mode at λ_{01}^{FBG}, it should experience high reflection [Fig.6.2.5(a)] and low transmission [Fig.6.2.5(c)]. Note that after optimization, $V_T(\lambda_{11}^{FBG})$ decreases slightly [Fig.6.2.5(d)]. As mentioned previous, it might result from the system coupling efficiency decreasing at λ_{11}^{FBG}. Again, generally after 2-3 optimization cycles, the values of all signals become reasonably close to that after optimization, which agrees well with

Figs. 6.2.4(c). It suggests that, it take 2-3 optimization cycles to selectively excite almost pure LP_{01} mode at λ_{11}^{FBG} at the FBG location within the TMF.

The above experiments successfully demonstrate the feasibility of TDM and AO-based mode control using only the reflection signals as feedback. In the future, by inscribing multiple ultra-weak FBGs into the TMF, we should be able to extend the current method to mode control at multiple locations within the TMF sensor network.

6.3 Discussion and Conclusions

The accuracy of the optimization process described above can potentially be impacted by factors such as fiber Rayleigh scattering, detector noises, and digitizer resolution. In our current setup, the main limiting factor is likely the resolution of the digitizer (8 bits only), which prevents us from accurately detecting weak FBG reflections. The optimization speed of the current experimental system is mainly limited by the software overhead, and it takes ~20s for one optimization cycle. By using fast FPGA chips for signal processing, it is possible to reach the maximal frame rate of the DM, i.e. ~34 kHz. Under these conditions, it should only take ~50 ms to complete one optimization cycle.

In conclusion, by combine the TDM technique reported in [43] with AO, we can adaptively control the form of optical signals at different FBG locations within the TMF. In Section 6.1, we have demonstrated TDM and AO-based mode control by using both the reflection and transmission signals of the FBG as feedback. Specifically, the feedback for AO-based mode control is determined by the ratio of the magnitudes between the transmission pulse and reflection pulse from specific FBG. Experimentally, we have demonstrated that by maximizing the feedback signal at the FBG peak reflection wavelength associated with the LP_{01} mode, we can set optical fields at two different FBG locations to be almost purely LP_{11} respectively. This method should be able to be easily adapted to optimize the mode at the FBG locations to pure LP_{01} mode, by setting the laser wavelength to the FBG reflection peak associated with the LP_{11} mode.

In Section 6.2, the TDM and AO-based mode control is accomplished by using only the reflection signals as feedback. Specifically, it requires two lasers in the experiment. The two lasers are set to the two FBG peak reflection wavelengths associated with the LP_{01}

and LP_{11} modes. By maximizing the ratio of the reflection signals of two lasers (reflected by specific FBG), we can optimize the optical field at the FBG location to almost pure LP_{01} or LP_{11} mode.

In the future, by inscribing multiple weak FBGs in the TMF and applying the method developed here, it should be possible to adaptively control the composition of interrogation signals within a TMF network at any FBG location. Generalization of the TDM and AO-based mode control method to MMF-based optical networks should be possible.

Chapter 7

Summary of Future Work

In this chapter, we summarize the experiment results presented in this dissertation and discuss potential improvement and applications of the AO-based mode control method in the future.

In summary, we have accomplished the following research in this thesis:

- By using the correlation between the CCD camera image and the theoretical target profile as the feedback for SLM control, we experimentally demonstrate the feasibility of using AO to achieve highly selective mode excitations in a TMF. The target profile can be purely LP_{01}, purely LP_{11}, or a mixture of the two modes. Furthermore, selective mode control in TMF can be accomplished using as few as 5×5 independent phase elements.
- We demonstrate that it is possible to use the coupling ratio of a directional coupler as feedback signal for adaptive mode control. Specifically, by minimizing the coupling ratio of the crossover port, we can ensure that the optical field within the throughput port is dominated by the LP_{01} component. Conversely, by maximizing the coupling ratio, we can ensure that the optical fields in both the crossover and the throughput ports are dominated by the LP_{11} component.
- By using the ratio between FBG transmission and reflection as feedback, we can adaptively control the form of optical signals at the FBG location. Experimentally, we have demonstrated that by maximizing the feedback signal at the FBG peak reflection wavelength associated with the LP_{01} (or LP_{11}) mode, we can selectively excite almost purely LP_{11} (or LP_{01}) modes, respectively.
- By combining the TDM technique with AO, we can adaptively control the form of optical fields at different FBG locations within the TMF.

Specifically, the feedback for AO-based mode control is determined by the ratio of the magnitudes between the transmission pulse and reflection pulse from specific FBG. Experimentally, we have demonstrated that by maximizing the feedback signal at the FBG peak reflection wavelength associated with the LP_{01} mode, we can set optical fields at two different FBG locations to be almost purely LP_{11} respectively. The method should be able to be easily adapted to optimize the mode at the FBG locations to pure LP_{01} mode, by setting the laser to the peak reflection wavelength associated with the LP_{11} mode.

In addition, we can adaptively control the mode at the FBG location within the TMF based on only the reflection signals. The experiments require two lasers set to the two FBG peak reflection wavelengths associated with the LP_{01} and LP_{11} modes. By maximizing the ratio of the reflection signals of the two lasers (reflected by specific FBG), we can optimize the field at the FBG location to almost pure LP_{01} or LP_{11} mode.

Based on the results obtained in this dissertation, the research presented here can be directly applied for adaptive mode control in MMF. Specifically, it is possible to extend the current mode control method from TMF to MMF. We can simply use the TDM and AO based mode control method developed in Chapter 6. By using the ratio between the reflection and transmission signals as feedback, it should be able to optimize the optical field within the MMF to desired LP modes.

Additionally, the results presented here can be used to develop two mode FBG sensor networks. It is possible to develop a two mode FBG sensor network based on the AO-based mode control method for simultaneous temperature and strain [70], and temperature and refractive index sensing [71, 72] *et. al*.

Finally, our work can potentially be extended for FBG-based mode control using OPC. OPC is widely used in MMF-based imaging [8]. In MMF-based imaging, a point source at the fiber distal end is required for OPC. For FBG in MMF, the reflection signal must be pure LP_{01} or LP_{11} mode. We can utilize the FBG reflection signal for OPC-based mode control in MMF. It is also possible to improve the mode control speed by using the OPC approach.

References

1. P. J. Winzer, “Optical networking beyond WDM,” IEEE Photon. J. 4, 647-651 (2012).
2. R. -J. Essiambre, R. Ryf, N. K. Fontaine, and S. Randel, “Breakthroughs in Photonics 2012: Space-Division Multiplexing in Multimode and Multicore Fibers for High-Capacity Optical Communication,” IEEE Photon. J. 5, 0701307 (2013).
3. D. J. Richardson, J. M. Fini, and L. E. Nelson, “Space-division multiplexing in optical fibres,” Nature Photon. 7, 354-362 (2013).
4. R. Ryf, S. Randel, A. H. Gnauck, C. Bolle, R.-J. Essiambre, P. J. Winzer, D. W. Peckham, A. McCurdy, and R. Lingle, “Space-division multiplexing over 10 km of three-mode fiber using coherent 6×6 MIMO processing,” Proc. Optical Fiber Communications Conference (OFC/NFOEC 2011), paper PDPB10.
5. M. Salsi, C. Koebele, D. Sperti, P. Tran, P. Brindel, H. Mardoyan, S. Bigo, A. Boutin, F. Verluise, P. Sillard, M. Astruc, L. Provost, F. Cerou, and G. Charlet, “Transmission at 2x100Gb/s, over two modes of 40-km-long prototype few-mode fiber, using LCOS-based mode multiplexer and demultiplexer,” Proc. Optical Fiber Communications Conference (OFC/NFOEC 2011), paper PDPB9.
6. A. Li, A. Al Amin, X. Chen, and W. Shieh, “Reception of mode and polarization multiplexed 107-Gb/s COOFDM signal over a two-mode fiber,” Proc. Optical Fiber Communications Conference (OFC/NFOEC 2011), paper PDPB8.
7. T. Čižmár and K. Dholakia, “Exploiting multimode waveguides for pure fiber-based imaging,” Nat. Commun. 3, 1027 (2012).
8. I. N. Papadopoulos, S. Farahi, C. Moser, and D. Psaltis, “High-resolution, lensless endoscope based on digital scanning through a multimode optical fiber,” Biomed. Opt. Express 4, 260-270 (2013).
9. T. Čižmár and K. Dholakia, “Shaping the light transmission through a multimode optical fibre: complex transformation analysis and applications in biophotonics,” Opt. Express 19, 18871-18884 (2011).

10. K. Y. Song and Y. H. Kim, “Characterization of stimulated Brillouin scattering in a few-mode fiber,” Opt. Lett. 38, 4841-4844 (2013).
11. A. Li, Q. Hu, and W. Shieh, “Characterization of stimulated Brillouin scattering in a circular-core two-mode fiber using optical time-domain analysis,” Opt. Express 21, 31894-31906 (2013).
12. A. Li, Y. Wang, Q. Hu, and W. Shieh, “Few-Mode fiber based optical sensors,” Opt. Express 23, 1139-1150 (2015).
13. R. Ryf, N. K. Fontaine, and R. -J. Essiambre, “Spot-based mode coupler for mode-multiplexed transmission in few mode fiber,” in Proc. IEEE Summer Topical, TuC3.2 (2012).
14. H. Bulow, H. Al Hashimi, and B. Schmauss, “Spatial-mode multiplexers and MIMO processing,” Proc. Opto-Electronics and Communication Conference (OECC 2012), paper 5E4-1.
15. S. G. Leon-Saval, A. Argyros, and J. Bland-Hawthorn, “Photonic lanterns: A study of light propagation in multimode to single-mode converters,” Opt. Express 18, 8430-8439 (2010).
16. N. K. Fontaine, R. Ryf, S. G. Leon-Saval, and J. Bland-Hawthorn, “Evaluation of photonic lanterns for lossless mode-multiplexing,” Proc. European Conference on Optical Communication (ECOC 2012), paper Th.2.D.6.
17. R. Ryf, N. K. Fontaine, M. A. Mestre, S. Randel, X. Palou, C. Bolle, A. H. Gnauck, S. Chandrasekhar, X. Liu, B. Guan, R.-J. Essiambre, P. J. Winzer, S. Leon-Saval, J. Bland-Hawthorn, R. Delbue, P. Pupalaikis, A. Sureka, Y. Sun, L. Grüner-Nielsen, R. V. Jensen, and R. Lingle, “12 × 12 MIMO transmission over 130-km few-mode fiber,” in Proc. Frontiers in Optics Conference (FiO 2012), paper FW6C.4.
18. N. Bai, E. Ip, Y.-K. Huang, E. Mateo, F. Yaman, M.-J. Li, S. Bickham, S. Ten, J. Linares, C. Montero, V. Moreno, X. Prieto, V. Tse, K. M. Chung, A. P. T. Lau, H.-Y. Tam, C. Lu, Y. Luo, G.-D. Peng, G. Li, and T. Wang, “Mode-division multiplexed transmission with inline few-mode fiber amplifier,” Opt. Express 20, 2668-2680 (2012).

19. J. Carpenter and T. D. Wilkinson, “All-optical mode multiplexing using holography and multimode fiber couplers,” J. Lightwave Technol. 30, 1978-1984 (2012).
20. J. Hoyningen-Huene, R. Ryf, and P. Winzer, “LCoS-based mode shaper for few-mode fiber,” Opt. Express 21, 18097-18110 (2013).
21. M. Mundus, J. U. Thomas, C. Voigtlander, R. G. Becker, C. Jauregui, A. Tunnermann, and S. Nolte, “CGH-based real-time analysis of fiber Bragg gratings in few mode LMA fibers,” Proc. SPIE 8237, 823712 (2012).
22. M. M. Ali, Y. Jung, K.-S. Lim, Md. R. Islam, S. Alam, D. J. Richardson, and H. Ahmad, “Characterization of Mode Coupling in Few-Mode FBG With Selective Mode Excitation,” IEEE Photon. Technol. Lett. 27, 1713-1716 (2015).
23. I. M. Vellekoop and A. P. Mosk, “Focusing coherent light through opaque strongly scattering media,” Opt. Lett. 32, 2309-2311 (2007).
24. I. M. Vellekoop and A. P. Mosk, “Phase control algorithms for focusing light through turbid media,” Opt. Commun. 281, 3071-3080 (2008).
25. S. M. Popoff, G. Lerosey, R. Carminati, M. Fink, A. C. Boccara, and S. Gigan, “Measuring the transmission matrix in optics: an approach to the study and control of light propagation in disordered media,” Phys. Rev. Lett. 104, 100601 (2010).
26. M. Cui, “Parallel wavefront optimization method for focusing light through random scattering media,” Opt. Lett. 36, 870-872 (2011).
27. D. B. Conkey, A. M. Caravaca-Aguirre, and R. Piestun, “High-speed scattering medium characterization with application to focusing light through turbid media,” Opt. Express 20, 1733-1740 (2012).
28. C. Stockbridge, Y. Lu, J. Moore, S. Hoffman, R. Paxman, K. Toussaint, and T. Bifano, “Focusing through dynamic scattering media,” Opt. Express 20, 15086-15092 (2012).
29. I. M. Vellekoop and C. M. Aegerter, “Scattered light fluorescence microscopy: imaging through turbid layers,” Opt. Lett. 35, 1245-1247 (2010).
30. G. Ghielmetti and C. M. Aegerter, “Scattered light fluorescence microscopy in three dimensions,” Opt. Express 20, 3744-3752 (2012).

31. F. Dubois, P. Emplit, and O. Hugon, “Selective mode excitation in graded-index multimode fiber by a computer-generated optical mask,” Opt. Lett. 19, 433-435 (1994).
32. X. Shen, J. M. Kahn, and M. A. Horowitz, “Compensation for multimode fiber dispersion by adaptive optics,” Opt. Lett. 30, 2985-2987 (2005).
33. A. Okamoto, K. Aoki, Y. Wakayama, D. Soma, and T. Oda, “Multi-excitation of spatial modes using single spatial light modulator for mode division multiplexing,” in Optical Fiber Communication Conference/National Fiber Optic Engineers Conference (OFC/NFOEC, 2012), paper JW2A.38.
34. G. Keiser, *Optical Fiber Communications, 4th edition*, (McGraw-Hill Education, 2010).
35. W. V. Sorin, B. Y. Kim, and H. J. Shaw, “Highly selective evanescent modal filter for two-mode optical fibers,” Opt. Lett. 11, 581-583 (1986).
36. K. Y. Song, I. K. Hwang, S. H. Yun, and B. Y. Kim, “High performance fused-type mode selective coupler for two-mode fiber devices,” in Opt. Fiber Commun. Conf. (Baltimore, 2000), paper TuB5.
37. R. Ismaeel, T. Lee, B. Oduro, Y. Jung, and G. Brambilla, “All-fiber fused directional coupler for highly efficient spatial mode conversion,” Opt. Express 22, 11610-11619 (2014).
38. G. Meltz, W. W. Morey, and W. H. Glenn, “Formation of Bragg gratings in optical fibers by a transverse holographic method,” Opt. Lett. 14, 823-825 (1989).
39. A. Yariv and P. Yeh, *optical electronics in modern communications,* 6th *edition*, (Oxford University Press, 2006).
40. I. Baumann, J. Seifert, W. Nowak, and M. Sauer, “Compact all-fiber add-drop-multiplexer using fiber Bragg gratings,” IEEE Photon. Technol. Lett. 8, 1331-1333 (1996).
41. M.G. Xu, A. T. Alavie, R. Maaskant, and M. M. Ohn, “Tunable fibre bandpass filter based on a linearly chirped fibre Bragg grating for wavelength demultiplexing,” Electron. Lett. 32, 1918-1919 (1996).

42. K. O. Hill, F. Bilodeau, B. Malo, T. Kitagawa, S. Thériault, D. C. Johnson, J. Albert, and K. Takiguchi, "Chirped in-fiber Bragg gratings for compensation of optical-fiber dispersion," Opt. Lett. 19, 1314-1316 (1994).
43. Y. Wang, J. Gong, B. Dong, D. Y. Wang, T. J. Shillig, and A. Wang, "A large serial time-division multiplexed fiber Bragg grating sensor network," J. Light. Technol. 30, 2751-2756 (2012).
44. W. Liang, Y. Huang, Y. Xu, R. K. Lee1 and A. Yariv, "Highly sensitive fiber Bragg grating refractive index sensors," Appl. Phys. Lett. 86, 151122 (2005).
45. D. Qian, M.-F. Huang, E. Ip, Y.-K. Huang, Y. Shao, J. Hu, and T. Wang, "101.7-Tb/s (370×294-Gb/s) PDM-128QAM-OFDM transmission over 3×55-km SSMF using pilot-based phase noise mitigation," Proc. Optical Fiber Communications Conference (OFC 2011), paper PDPB5.
46. A. Sano, T. Kobayashi, S. Yamanaka, A. Matsuura, H. Kawanishi, Y. Miyamoto, K. Ishihara, and H. Masuda, "102.3-Tb/s (224 x 548-Gb/s) C- and extended L-band all-Raman transmission over 240 km using PDM-64QAM single carrier FDM with digital pilot tone," Proc. Optical Fiber Communications Conference (OFC 2012), paper PDP5C.3.
47. R. Kashyap and K. J. Blow, "Observation of catastrophic self-propelled self-focusing in optical fibers," Electron. Lett. 24, 47-49 (1988).
48. R.-J. Essiambre, G. Kramer, P. J. Winzer, G. J. Foschini, and B. Goebel, "Capacity limits of optical fiber networks," J. Lightwave Technol. 28, 662-701 (2010).
49. P. P. Mitra and J. B. Stark, "Nonlinear limits to the information capacity of optical fibre communications," Nature. 411, 1027-1030(2001).
50. S. Berdague, and P. Facq, "Mode division multiplexing in optical fibers," Appl. Opt. 21, 1950-1955 (1982).
51. H. R. Stuart, "Dispersive multiplexing in multimode optical fiber," Science 289, 281-283 (2000).
52. A.R. Shah, R.C.J. Hsu, A. Tarighat, A.H. Sayed, and B. Jalali, "Coherent Optical MIMO (COMIMO)," IEEE J. Lightwave Techno. 23, 2410-2419 (2005).

53. B. C. Thomsen, “MIMO enabled 40 Gb/s transmission using mode division multiplexing in multimode fiber,” Proc. Optical Fiber Communications Conference (OFC/NFOEC 2010), paper OThM6.
54. B. Franz, D. Suikat, R. F. Dischler, F. Buchali, and H. Buelow, “High Speed OFDM Data Transmission Over 5 km GI-Multimode Fiber Using Spatial Multiplexing With 2×4 MIMO Processing,” Proc. European Conference on Optical Communications 2010 (ECOC 2010), paper Tu3C4.
55. R. Ryf, S. Randel, A. H. Gnauck, C. Bolle, A. Sierra, S. Mumtaz, M. Esmaeelpour, E. C. Burrows, R. Essiambre, P. J. Winzer, D. W. Peckham, A. H. McCurdy, and R. Lingle, “Mode-division multiplexing over 96 km of few-mode fiber using coherent 6×6 MIMO processing,” J. Light. Technol. 30, 521-531 (2012).
56. S. Randel, R. Ryf, A. Sierra, P. J. Winzer, A. H. Gnauck, C. A. Bolle, R.-J. Essiambre, D. W. Peckham, A. McCurdy, and R. Lingle, “6×56-Gb/s mode-division multiplexed transmission over 33-km few-mode fiber enabled by 6×6 MIMO equalization,” Opt. Express 19, 16697-16707 (2011)
57. V. A. J. M. Sleiffer, Y. Jung, V. Veljanovski, R. G. H. van Uden, M. Kuschnerov, H. Chen, B. Inan, L. Gruner Nielsen, Y. Sun, D. J. Richardson, S. U. Alam, F. Poletti, J. K. Sahu, A. Dhar, A. M. J. Koonen, B. Corbett, R. Winfield, A. D. Ellis, and H. de Waardt, “73.7 Tb/s (96 × 3 × 256 - Gb/s) mode-division-multiplexed DP-16QAM transmission with inline MM-EDFA,” Opt. Express 20, B428-B438 (2012).
58. A. M. Vengsarkar, W. C. Michie, L. Jankovic, B. Culshaw, and R. O. Claus, “Fiber-optic dual-technique sensor for simultaneous measurement of strain and temperature,” J. Lightwave Technol. 12, 170-177 (1994).
59. N. Lagakos, T. Litovitz, P. Macedo, R. Mohr, and R. Meister, “Multimode optical fiber displacement sensor,” Appl. Opt. 20, 167-168 (1981).
60. B. Y. Kim, J. N. Blake, S. Y. Huang, and H. J. Shaw, “Use of highly elliptical core fibers for two-mode fiber devices,” Opt. Lett. 12, 729-731 (1987).

61. Z. Chen, D. Lau, J. T. Teo, S. H. Ng, X. Yang, and P. L. Kei, "Simultaneous measurement of breathing rate and heart rate using a microbend multimode fiber optic sensor," J. Biomed. Opt. 19, 057001 (2014).
62. Y. Liu and L. Wei, "Low-cost high-sensitivity strain and temperature sensing," Appl. Opt. 46, 2516-2519 (2007)
63. D. Chen and X. Jiang, "All-fiber temperature sensor based on few mode fiber and single-mode fiber," Microwave & Opt. Technol. Lett. 55, 1700-1703 (2013).
64. T. Huang, X. Shao, Z. Wu, Y. Sun, J. Zhang, H. Q. Lam, J. Hu, and P. P. Shum, "A sensitivity enhanced temperature sensor based on highly Germania-doped few-mode fiber," Opt. Commun. 324, 53-57 (2014).
65. Q. Wang and G. Farrell, "All-fiber multimode-interference-based refractometer sensor: proposal and design," Opt. Lett. 31, 317-319 (2006).
66. J. Chen, P. Lu, D. Liu, J. Zhang, S. Wang, and D. Chen, "Optical fiber curvature sensor based on few mode fiber," Optik 125, 4776-4778 (2014).
67. K. H. Wanser, K. F. Voss, and A. D. Kersey, "Novel fiber devices and sensors based on multimode fiber Bragg gratings," Proc. SPIE 2360, 265-268 (1994).
68. T. Mizunami, T. V. Djambova, T. Niiho, and S. Gupta, "Bragg gratings in multimode and few-mode optical fibers," J. Lightwave Technol. 18, 230-235 (2000).
69. W. Zhao and R. O. Claus, "Optical fiber grating sensors in multimode fibers," Smart Mater. Struct. 9, 212-214 (2000).
70. J. Lim, Q. Yang, B. E. Jones, and P. R. Jackson, "Strain and temperature sensors using multimode optical fiber Bragg gratings and correlation signal processing," IEEE Trans. Instrum. Meas. 51, 622-627 (2002).
71. C.-L. Zhao, X. Yang, M. Demokan, and W. Jin, "Simultaneous temperature and refractive index measurements using a 3° slanted multimode fiber Bragg grating," J. Lightwave Technol. 24, 879-883 (2006).
72. H. Z. Yang, M. M. Ali, Md. R. Islam, K.-S. Lim, D. S. Gunawardena, and H. Ahmad, "Cladless few mode fiber grating sensor for simultaneous refractive index and temperature measurement," Sens. Actuators, A: Phys. 228, 62-68 (2015).

73. A. Sun and Z. Wu, “Multimode interference in single mode-multimode FBG for simultaneous measurement of strain and bending,” IEEE. Sensors J. 15, 3390-3394 (2015).
74. Y. Weng, E. Ip, Z. Pan, and T. Wang, “Few-mode distributed optical fiber sensors,” Opt. Photon. News 26, 59-59 (2015).
75. Y. Weng, E. Ip, Z. Pan, and T. Wang, “Single-end simultaneous temperature and strain sensing techniques based on Brillouin optical time domain reflectometry in few-mode fibers,” Opt. Express 23, 9024-9039 (2015).
76. A. Li, Y. Wang, J. Fang, M.-J. Li, B. Y. Kim, and W. Shieh, “Few-mode fiber multi-parameter sensor with distributed temperature and strain discrimination,” Opt. Lett. 40, 1488-1491 (2015).
77. A. Li, Y. Wang, Q. Hu, D. Che, X. Chen, and W. Shieh, “Measurement of distributed mode coupling in a few-mode fiber using a reconfigurable Brillouin OTDR,” Opt. Lett. 39, 6418-6421 (2014).
78. E. Spitz and A. Werts, “Transmission of images along an optical fibre,” C. R. Acad. Sci. Ser. B 264, 1015-1018 (1967).
79. Y. Choi, C. Yoon, M. Kim, T. D. Yang, C. Fang-Yen, R. R. Dasari, K. J. Lee, and W. Choi, “Scanner-Free and Wide-Field Endoscopic Imaging by Using a Single Multimode Optical Fiber,” Phys. Rev. Lett. 109, 203901 (2012).
80. M. Plöschner, B. Straka, K. Dholakia, and T. Čižmár, “GPU accelerated toolbox for real-time beam-shaping in multimode fibres,” Opt. Express 22, 2933-2947 (2014).
81. R. Barankov and J. Mertz, “High-throughput imaging of self-luminous objects through a single optical fibre,” Nat. Commun. 5, 5581 (2014).
82. S. M. Kolenderska, O. Katz, M. Fink, and S. Gigan, “Scanning-free imaging through a single fiber by random spatio-spectral encoding,” Opt. Lett. 40, 534-537 (2014).
83. D. Loterie, S. Farahi, I. Papadopoulos, A. Goy, D. Psaltis, and C. Moser, “Digital confocal microscopy through a multimode fiber,” Opt. Express 23, 23845-23858 (2015).

84. D. Loterie, S. A. Goorden, D. Psaltis, and C. Moser, “Confocal microscopy through a multimode fiber using optical correlation,” Opt. Lett. 40, 5754-5757 (2015).
85. G. P. J. Laporte, N. Stasio, C. Moser, and D. Psaltis, “Enhanced resolution in a multimode fiber imaging system,” Opt. Express 23, 27484-27493 (2015).
86. E. E. Morales-Delgado, D. Psaltis, and C. Moser, “Two-photon imaging through a multimode fiber,” Opt. Express 23, 32158-32170 (2015).
87. M. Plöschner, V. Kollárová, Z. Dostál, J. Nylk, T. Barton-Owen, D. E. K. Ferrier, R. Chmelík, K. Dholakia, and T. Čižmár, “Multimode fibre: Light-sheet microscopy at the tip of a needle,” Sci. Rep.5, 18050 (2015).
88. D. Kim, J. Moon, M. Kim, T. D. Yang, J. Kim, E. Chung, and W. Choi, “Toward a miniature endomicroscope: pixelation-free and diffraction-limited imaging through a fiber bundle,” Opt. Lett. 39, 1921-1924 (2014).
89. M. Kreysing, D. Ott, M. J. Schmidberger, O. Otto, M. Schurmann, E. Martin-Badosa, G. Whyte, and J. Guck, “Dynamic operation of optical fibres beyond the single-mode regime facilitates the orientation of biological cells,” Nat. Commun. 5, 5481 (2014).
90. Y. Choi, C. Yoon, M. Kim, J. Yang, and W. Choi, “Disorder-mediated enhancement of fiber numerical aperture,” Opt. Lett. 38, 2253-2255 (2013).
91. I. N. Papadopoulos, S. Farahi, C. Moser, and D. Psaltis, “Increasing the imaging capabilities of multimode fibers by exploiting the properties of highly scattering media,” Opt. Lett. 38, 2776-2778 (2013).
92. S. Rosen, D. Gilboa, O. Katz, and Y. Silberberg, “Focusing and scanning through flexible multimode fibers without access to the distal end,” arXiv:1506.08586 (2015).
93. S. Farahi, D. Ziegler, I. N. Papadopoulos, D. Psaltis, and C. Moser, “Dynamic bending compensation while focusing through a multimode fiber,” Opt. Express 21, 22504-22514 (2013).
94. R. Y. Gu, R. N. Mahalati, and J. M. Kahn, “Design of flexible multi-mode fiber endoscope,” Opt. Express 23, 26905-26918 (2015).

95. R. Y. Gu, R. N. Mahalati, and J. M. Kahn, “Noise-reduction algorithms for optimization-based imaging through multi-mode fiber,” Opt. Express 22, 15118-15132 (2014).
96. S. G. Leon-Saval, T. A. Birks, J. Bland-Hawthorn, and M. Englund, “Multimode fiber devices with single-mode performance,” Opt. Lett. 30, 2545-2547 (2005).
97. S. G. Leon-Saval, N. K. Fontaine, J. R. Salazar-Gil, B. Ercan, R. Ryf, and J. Bland-Hawthorn, “Mode-selective photonic lanterns for space-division multiplexing,” Opt. Express 22, 1036-1044 (2014).
98. D. Noordegraaf, P. M. W. Skovgaard, M. D. Nielsen, and J. Bland-Hawthorn, “Efficient multi-mode to singlemode coupling in a photonic lantern,” Opt. Express 17, 1988-1994 (2009).
99. A. Li, X. Chen, A. Al Amin, J. Ye, and W. Shieh, “Space-division multiplexed high-speed superchannel transmission over few-mode fiber,” J. Lightwave Technol. 30, 3953-3964 (2012).
100. T. Uematsu, Y. Ishizaka, Y. Kawaguchi, K. Saitoh, and M. Koshiba, “Design of a compact two-mode multi/demultiplexer consisting of multimode interference waveguides and a wavelength-insensitive phase shifter for mode-division multiplexing transmission,” J. Lightwave. Technol. 30, 2421-2426 (2012).
101. Y. Ding, J. Xu, F. D. Ros, B. Huang, H. Ou, and C. Peucheret, “On-chip two-mode division multiplexing using tapered directional coupler-based mode multiplexer and demultiplexer,” Opt. Express. 21, 10376-10382 (2013).
102. J. B. Driscoll, R. R. Grote, B. Souhan, J. I. Dadap, M. Lu and R. M. Osgood, Jr, “Asymmetric Y-junctions in silicon waveguides for on-chip mode-division multiplexing,” Opt. Lett. 38, 1854-1856 (2013).
103. T. Su, R. P. Scott, S. S. Djordjevic, N. K. Fontaine, D. J. Geisler, X. Cai, and S. J. B. Yoo, “Demonstration of free space coherent optical communication using integrated silicon photonic orbital angular momentum devices,” Opt. Express 20, 9396-9402 (2012).

104. C. P. Tsekrekos and D. Syvridis, “All-fiber broadband LP02 mode converter for future wavelength and mode division multiplexing systems,” Photonics Technol. Lett. 24, 1638-1641 (2012).
105. H. W. Babcock, “The possibility of compensating astronomical seeing,” Publ. Astron. Soc. Pac. 65, 229-236 (1953).
106. J. W. Hardy, *Adaptive Optics for Astronomical Telescopes* (Oxford University Press, New York, 1998).
107. M. J. Steel, B. Marks, and A. Rahmani, “Properties of sub-diffraction limited focusing by optical phase conjugation,” Opt. Express 18, 1487-1500 (2010).
108. E. G. van Putten, D. Akbulut, J. Bertolotti, W. L. Vos, A. Lagendijk, and A. P. Mosk, “Scattering lens resolves sub-100 nm structures with visible light,” Phys. Rev. Lett. 106, 193905 (2011).
109. S. Feng, C. Kane, P. A. Lee, and A. D. Stone, “Correlations and fluctuations of coherent wave transmission through disordered media,” Phys. Rev. Lett. 61, 834-837 (1988).
110. I. Freund, M. Rosenbluh, and S. Feng, “Memory effects in propagation of optical waves through disordered media,” Phys. Rev. Lett. 61, 2328-2331 (1988).
111. C. L. Hsieh, Y. Pu, R. Grange, and D. Psaltis, “Digital phase conjugation of second harmonic radiation emitted by nanoparticles in turbid media,” Opt. Express 18, 12283-12290 (2010).
112. J. Tang, R. N. Germain, and M. Cui, “Superpenetration optical microscopy by iterative multiphoton adaptive compensation technique,” Proc. Natl Acad. Sci. USA 109, 8434-8439 (2012).
113. K. Si, R. Fiolka, and M. Cui, “Fluorescence imaging beyond the ballistic regime by ultrasound-pulse-guided digital phase conjugation,” Nature Photon. 6, 657-661 (2012).
114. R. N. Mahalati, D. Askarov, J. P. Wilde, and J. M. Kahn, “Adaptive control of input field to achieve desired output intensity profile in multimode fiber with random mode coupling,” Opt. Express 20, 14321-14337 (2012).

115. D. B. Conkey, A. N. Brown, A. M. Caravaca-Aguirre, and R. Piestun, “Genetic algorithm optimization for focusing through turbid media in noisy environments,” Opt. Express 20, 4840-4849 (2012).
116. A. M. Caravaca-Aguirre, E. Niv, D. B. Conkey, and R. Piestun, “Real-time resilient focusing through a bending multimode fiber,” Opt. Express 21, 12881-12887 (2013).